TECHNISCHE UNIVERSITÄT WIEN

DIPLOMARBEIT

Comparison of ice nucleating particles from fruit juices and their properties

ausgeführt am

Institut für Materialchemie (E 165)

der

Technischen Universität Wien

unter der Anleitung von

Ao.Univ.Prof. Dipl.-Chem. Dr.rer.nat. Hinrich Grothe

durch

Bianca Fiala, BSc

Wien, am 28.Februar.2018

Bianca Fiala

Gewidmet an Mama

Abstract

Heterogeneous ice nucleation is a crucial process for ice cloud formation in the atmosphere. Recent findings indicate the importance of ice nucleating particles of biological origin in this process. Previous investigations in our group (Pummer *et al.*, 2012) revealed that pollen from several plants native to the boreal forests contain ice nucleating macromolecules, which are easily detached from the grains. Investigating a broader scope of boreal plants, Bichler (2015) showed that several juices of berries contain ice nucleation active macromolecules. Based on this research we examined ice nucleation activity and general properties of five juices from perennial plants: acerola, black currant, chokeberry, elderberry and sea buckthorn. With the only exception of acerola, which occurs primarily in the tropics and subtropics, the other four plants can be distributed up to the boreal zone. All of the examined fruit juices exhibit ice nucleation activity, $T_{50,het}$ values (median heterogeneous freezing temperature) of the pure juices are ranging between -17.9 °C and -29.6 °C. We elucidated particle size dependency of the ice nucleation activity to differentiate between coarse and submicron ice nucleating particles. For all analysed fruit juices ice nucleating particles were detected in both fractions: the coarse (> 0.45 µm) and the submicron size range (< 0.45 µm). For all five juices no direct correlation between dry mass and ice nucleation activity was found. Therefore no conclusions can be drawn from the dry mass of a juice concerning the ice nucleating particle quantity. The results of the investigations with different solvents (methanol, methylene chloride, and cyclohexane) suggest that polar components play an important role in the ice nucleation activity of acerola, black currant, chokeberry, elderberry and sea buckthorn. By FTIR spectroscopy numerous strong bands were assigned to saccharides, lipids and phenolic compounds. Further, broad bands in the different amid regions were present. The two juices that show the highest ice nucleation activity (sea buckthorn and black currant) were investigated with chaotropic agents (guanidinium chloride and urea) and a protein-digesting enzyme (Subtilisin). This way, properties like the importance of hydrogen bonds and other structure forming polar interactions were controlled. Our results suggest that proteinaceous compounds play a key role in the ice nucleation activity of pure black currant and sea buckthorn juice.

Zusammenfassung

Heterogene Eisnukleation ist ein wichtiger Prozess in der atmosphärischen Wolkenbildung. Die Wichtigkeit von biologischen Substanzen in diesem Prozess wird durch mehrere Studien aus der jüngeren Vergangenheit nahegelegt. Durch frühere Untersuchungen unserer Arbeitsgruppe (Pummer *et al.*, 2012) konnte gezeigt werden, dass Pollenkörner einiger Pflanzen, die ihr Verbreitungsgebiet bis in die boreale Zone haben, Makromoleküle enthalten, welche die Eisnukleation bei höheren Temperaturen auslösen. Diese Makromoleküle konnten von den intakten Pollenkörnern leicht heruntergewaschen werden. Bichler (2015) führte Untersuchungen im breiteren Ausmaß mit borealen Pflanzen durch und zeigte, dass einige Beerenfruchtsäfte eisnukleationsaktive Makromoleküle beeinhalten. Auf diesen Forschungsergebnissen aufbauend, wurden die Eisnukleationsaktivität und ebenso allgemeine Eigenschaften von fünf Fruchtsäften, welche von mehrjährigen Pflanzen stammen, untersucht: Acerola, Aronia, Sanddorn, schwarzer Holunder und schwarze Johannisbeere. Mit der einzigen Ausnahme von Acerola, welche vorwiegend in den Tropen und Subtropen vorkommt, sind die untersuchten Pflanzen bis in die boreale Zone verbreitet. Alle analysierten Fruchtsäfte sind eisnukleationsaktiv, wobei die $T_{50,het}$ Werte (mittlere heterogene Gefriertemperatur) der puren Fruchtsäfte zwischen -17.9 °C und -29.6 °C liegen. Um zwischen groben und submikrometer großen Eiskeimen differenzieren zu können, wurde die Partikelgrößenabhängigkeit der Eisnukleationsaktivität untersucht. Alle fünf analysierten Fruchtsäfte enthalten Eiskeime in beiden Größenfraktionen, sowohl im groben (> 0.45 µm) als auch im submikrometer Bereich (< 0.45 µm). Weiters konnte zwischen dem Gesamtgehalt der Trockenmasse und der Eisnukleationsaktivität kein Zusammenhang gefunden werden. Daraus geht hervor, dass von der Trockenmasse eines Saftes kein Rückschluss auf die Anzahl der darin enthaltenen eisnukleationsaktiven Partikel gezogen werden kann. Die Ergebnisse der Experimente mit verschiedenen Lösungsmitteln (Methanol, Methylenchlorid und Cyclohexan) deuten darauf hin, dass polare Substanzen wichtig für die Eisnukleationsaktivität von Acerola, Aronia, Sanddorn, schwarzer Johannisbeere und schwarzem Holunder sind. Mittels FTIR Spektroskopie konnten zahlreiche breitere Banden Kohlenhydraten, Fetten und phenolischen Verbindungen zugeordnet werden. Überdies sind auch breitere Banden in den verschiedenen Amidregionen vorhanden.

Mit den beiden Fruchtsäften, welche die höchste Eisnukleationsaktivität aufweisen (Sanddorn und schwarze Johannisbeere) wurden zusätzliche Untersuchungen mit chaotropen Verbindungen (Guanidiniumchlorid und Harnstoff) und einem proteinverdauenden Enzym (Subtilisin) durchgeführt. Diese Versuche wurden ausgeführt, um die Rolle von Wasserstoffbrückenbindungen und anderen strukturbildenenden polaren Wechselwirkungen festzustellen. Die erhaltenen Ergebnisse deuten darauf hin, dass Proteine eine wichtige Rolle in der Eisnukleationsaktivität von purem Sanddorn und schwarzem Johannisbeer Fruchtsaft spielen.

Danksagung

An dieser Stelle möchte ich folgenden Personen danken, die mich während der experimentellen Versuchsdurchführung, bei dem Verfassen dieser Arbeit und auch indirekt während dieser intensiven Zeit unterstützt haben:

Professor Hinrich Grothe zum einen für die Möglichkeit, an diesem interessanten, interdisizplinären und umweltrelevanten Forschungsgebiet mitwirken zu können, sowie für die Feedbacks und die Betreuung im Verlauf der Arbeit.

Laura Felgitsch für ihre kontinuierliche Betreuung während meiner gesamten Arbeit, ihre gute Laune und ebenso für ihre Unterstützung, wenn ich etwas brauchte.

Meinen Bürokollegen, im Speziellen Philipp Baloh für viele Ideen und Anregungen, Vergnügtheiten und offene Ohren.

Der gesamten Belegschaft der physikalischen Chemie für die interessanten fachlichen und persönlichen Gespräche, die erheiternden Konversationen, sowie für die insgesamt angenehme Atmosphäre.

Dem FWF (Projekt No. P 26040) und FFG (Project No. 850689) für die finanzielle Förderung dieser Arbeit.

Im Laufe des Studiums sind unter anderem durch Laborübungen, Lernen für Übungen und Prüfungen auch ein paar langjährige Freundschaften mit Studierenden erwachsen, die ich nicht missen möchte!

Meiner Schwester, meinem Papa und besonders meiner Mama möchte ich für ihre Unterstützung ganz herzlich danken! Großer Dank gilt auch meiner Verwandtschaft, sowie jenen Menschen, die in den vergangenen Jahren zu meiner Familie dazu gewachsen sind!

Contents

Abbreviations

A	Acerola
a. u.	Arbitrary unit
AFGP(s)	Antifreeze glycoprotein(s)
AFP(s)	Antifreeze protein(s)
ATD	Arizona Test Dust
ATR	Attenuated total reflectance
B	Black currant
C	Chokeberry
CCN(s)	Cloud Condensation nucleus (nuclei)
CNT	Classical nucleation theory
E	Elderberry
e.g.	exempli gratia (for example)
FTIR	Fourier Transformed Infrared Spectroscopy
GdmCl	Guanidinium chloride
GHG(s)	Greenhouse gas(es)
i.e.	id est (that is)
INA	Ice nucleation activity
INMs	Ice nucleating macromolecules
INP(s)	Ice nucleating particle(s)
IPCC	Intergovernmental Panel on Climate Change
IR	Infrared
K	Kelvin
kDa	kilodalton
M	molar
n. a.	not available
NIR	Near infrared
p. a.	pro analysi (analytically pure)
PMT	Photomultiplier
ppm	part per million by volume
PSC(s)	Polar Stratospheric Cloud(s)

RH	relative humidity
rpm	rounds per minute
RT	room temperature
S	Sea buckthorn
S_i	Saturation ratio
SM	Snomax® (shredded fragments of Pseudomonas syringae)
SNR	Signal-to-Noise Ratio
Tris	Tris(hydroxymethyl)aminomethane
upw	ultrapure water
UV-VIS	Ultraviolet-Visible
VODCA	Vienna Optical Droplet Crystallization Analyser
WMO	World Meterological Organization
wt%	mass fraction

1 Introduction

If not indicated otherwise, the information of this chapter is mainly extracted from the following books: Seinfeld and Pandis (2016), Petty (2008), Fabian (1989) and references therein.

1.1 The Atmosphere

The atmosphere of the Earth is a gaseous zone, which surrounds the planet and its specific composition is an essential condition for the existence of life. The atmospheric gases, which are held back by the Earth´s gravitation field, consist mostly of nitrogen (78 %), oxygen (21 %) and argon (0.9 %). Another important component is water vapour, which exhibits a highly variable ratio (up to 3 %). Its present level is controlled by evaporation, cloud formation and precipitation. Trace amounts of carbon dioxide (403 ppm[1]), hydrogen, methane, nitrous oxide, carbon oxide and other noble gases (in order of frequency: neon, helium, krypton) are also present in the atmosphere. These rare gases comprise less than 0.1 % in quantity. Although the concentration of these gases is very small, they are essential for the life on Earth as we know it, as they influence the properties of the atmosphere in elementary ways such as their absorption capacity of infrared (IR) radiation. This aspect is worked out in more detail in the section climate (subchapter 1.2).

As a consequence of photosynthesis a high amount of oxygen is present in the atmosphere and it has therefore a strongly oxidizing character. The oxygen concentration is regulated via a balance between oxygen production due to photosynthesis ($6\ CO_2 + 6\ H_2O + \text{light} \xrightarrow{Chlorophyll} C_6H_{12}O_6 + 6\ O_2$) and consumption through respiration and decay of organic compounds.

The pressure and therefore the density decreases exponentially from sea level with increasing altitude, which can be addressed with the barometric formula (Equation 1).

$$p(h_z) = p(h_0)\, e^{\left[\frac{-\Delta h}{\left(\frac{RT}{Mg}\right)}\right]}$$

Equation 1

[1] https://www.esrl.noaa.gov/gmd/ccgg/trends (5.10.2017)

$p(h_z)$	Pressure at a height z [Pa]
$p(h_0)$	Pressure at sea level: 101325 [Pa]
Δh	Height difference between h_z and h_0 [m]
R	Gas constant: 8.31446 [J∗mol^{-1}∗K^{-1}]
T	Temperature is assumed to be constant at 288.15 [K]
M	Mean molecular weight of air: 0.02897 [kg∗mol^{-1}]
g	Acceleration due to gravity: 9.80665 [m∗s^{-2}]

Owing to this fact the mass majority of the atmosphere is located in the troposphere (approx. 70 - 90 %) and in the stratosphere (approx. 10 - 30 %). The mesosphere holds only about 0.1 % and the thermosphere holds just 0.001 % of the total atmospheric mass. The atmospheric pressure at a certain point is proportional to the mass of the atmospheric gases above that specific point. The air is markedly thinner at top of a high mountain than at sea level, leading to pressure differences at the different altitudes. It is regarded as logically meaningful to distinguish the atmosphere in five different layers based on the vertical temperature profile with height. The gradient is termed as lapse rate. The variations of the temperature and pressure of the different layers (except of the outermost layer, the exosphere) are illustrated in Figure 1.

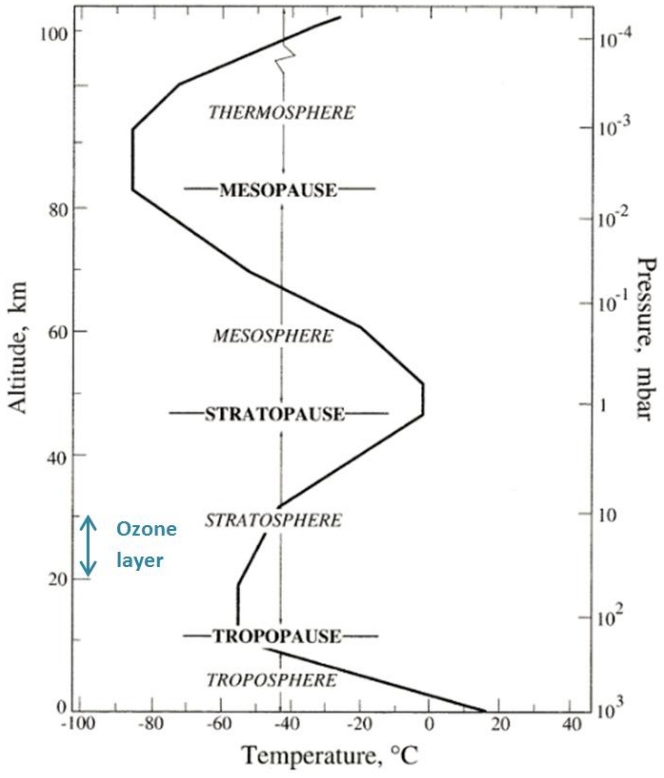

Figure 1: Temperature and pressure profile of the layers of the Earth´s atmosphere, except of the farthest exosphere (adapted from: Seinfeld and Pandis, 2016).

Beginning from the lowest to the highest (from the perspective of the Earth´s surface), the five main layers, which are distinguished by the temperature profile with height, are described hereinafter.

The troposphere is the lowest layer of the Earth´s atmosphere and it extends upwards from the surface to the tropopause, which is 8 km at the poles and 18 km at the equator. The thickness of this layer varies not only with the latitude, but also with the season. The troposphere is a zone of rapid vertical mixing, which is promoted by the vertical temperature gradient. The general principle is that warm air rises up and cold air sinks down. Since the temperature declines almost linearly with height in the troposphere and it rises with altitude in the close-by stratosphere, the tropopause is an isothermal inversion layer. In fact, little mixing occurs between troposphere and stratosphere. Through the low temperature at the tropopause the water vapour condensates almost completely in the troposphere, thus it contains the main quantity of atmospheric water. As a consequence nearly all weather phenomena take place in the troposphere and therefore it is also known as weather-creating layer.

The stratosphere extends from the tropopause upwards to the stratopause, which is located approx. 45 to 55 km above the Earth´s surface. Slow vertical mixing occurs in the stratosphere due to the positive temperature gradient. The stratosphere is thermally stratified: the first zone is an isothermal region, reaching from 11 to 20 km over midlatitudes and in the second zone the temperature increases again. About 90 % of the atmospheric ozone is present in the stratosphere. In 20 to 30 km height the ozone concentration reaches its highest level, therefore this region is called ozone layer.
Ozone has an important function for living, since it protects living organisms from harmful, high energetic solar ultraviolet radiation due to absorption by oxygen (O_2) and leading in the next step to formation of ozone (O_3), which is also absorbing. The Chapman cycle (Figure 2) describes the photochemical formation of ozone caused by the radiation with shortwave ultraviolet light ($\lambda < 242$ nm) and the photolytic cleavage ($\lambda < 1200$ nm) of it. At this ultraviolet radiation absorption process the electromagnetic radiation is converted into heat and therefore the temperature steadily increases from 20 to 50 km height.

$$O_2 \xrightarrow{\lambda < 242\ nm} O + O$$
$$O + O_2 + M \longrightarrow O_3 + M \qquad (M = O_2 \text{ or } N_2 \text{ usually})$$
$$O + O_3 \longrightarrow 2O_2$$
$$O_3 \xrightarrow{\lambda < 1200\ nm} O + O_2$$

Figure 2: Chapman cycle (Fabian, 1989, p. 27; Seinfeld and Pandis, 1998, pp. 164).

Most of the commercial aircraft traffic takes place at altitudes of 9 to 13 km in middle latitudes (Petty, 2008, p. 21) this zone is preferred as it is higher than the turbulent weather-creating layer of the atmosphere.

The mesosphere is the next layer; it is the region above the stratopause. Atop of the mesosphere is the mesopause (at around 80 to 90 km height), which is the boundary to the thermosphere. The mesosphere is characterized by rapid vertical mixing as the temperature falls with increasing altitude. The mesopause is, with a temperature of -93 °C (180.15 K), the coldest naturally occurring point of the atmosphere.

The forth layer of the Earth´s atmosphere is the thermosphere; it extends upwards from the mesopause. This layer has a thickness of several hundreds of kilometres and its end is not well-defined. Above the mesopause the total X-ray and hard ultraviolet radiation to about 175 nm is absorbed, this leads to ionisation of the atmospheric components (e.g. N_2 and O_2), which results in heating up the elevated atmosphere. Therefore the thermosphere is characterized by high temperatures (600 to 2000 K), which depend highly on the solar activity. This high temperature is not high in terms of thermodynamics but in terms of electronic excitation. One would not perceive this temperature due to the low density and therefore the low quantity of molecules that is prevailing at these altitudes.
The ionosphere includes the upper mesosphere and the lower thermosphere; it is a region where ions are increasingly produced during daytime due to photoionisation.

The uppermost layer is the exosphere, which extends above 500 km altitude; it is a transitional region between the atmosphere of the Earth and outer space. In this layer the density of present atmospheric gases (mainly helium and hydrogen) is very low and these

components are still affected from the gravity of the Earth. If these gas molecules have enough energy, they can escape into space.

1.2 The Climate and Earth´s Radiation Balance

The climate is the entity of all meteorological processes and describes the typical condition of the atmosphere over longer periods of time in a multifaceted interaction with landmasses, hydrosphere, cryosphere and living creatures. Earth´s climate is created as a result that in the equator near area the Earth absorbs most of the solar energy and transports it through winds and ocean movements to the colder polar regions (Seinfeld and Pandis, 1998, p. 4). Since water has unique properties (e.g. high specific heat capacity, high enthalpy of vaporization), mainly because of the strong hydrogen bonds, it is therefore able to smooth out large temperature differences in the Earth-atmosphere system (hydrological cycle) leading to a moderate climate.

The Intergovernmental Panel on Climate Change (IPCC) defines climate as follows (IPCC, 2014): "Climate in a narrow sense is usually defined as the average weather, or more rigorously, as the statistical description in terms of the mean and variability of relevant quantities over a period of time ranging from months to thousands or millions of years. The classical period for averaging these variables is 30 years, as defined by the World Meteorological Organization. The relevant quantities are most often surface variables such as temperature, precipitation, and wind. Climate in a wider sense is the state, including a statistical description, of the climate system."[2]

The climate is complex, because various chemical and physical processes are intertwined and act together leading to an overall effect, which cannot be estimated easily.
The Earth´s climate can be influenced due to the following three factors (Treut *et al.,* 2007):

- Incident solar radiation is dependent on the distance of the Sun and the Earth, as well as the solar activity. No intervention by human beings is possible.

[2] IPCC, 2014: Annex II: Glossary [Mach, K.J., S. Planton and C. von Stechow (eds.)]. In: *Climate Change 2014: Synthesis Report. Contribution of Working Groups I, II and III to the Fifth Assessment Report of the Intergovernmental Panel on Climate Change* [Core Writing Team, R.K. Pachauri and L.A. Meyer (eds.)]. IPCC, Geneva, Switzerland, pp. 119

- The albedo effect is defined as the reflectivity of the Earth due to cloud tops (also artificial clouds like contrails), Earth´s surface (thereby the state of the surface is important; especially deserts, oceans, snow/ice- and vegetation-covered ground have a large albedo effect) and atmosphere. Here natural sources (e.g. volcano eruptions) as well as anthropogenic activities (e.g. combustion of fossil fuels, biomass burning, and deforestation) cause an effect.
- Black body radiation (longwave) that is emitted from the Earth into outer space. Here greenhouse gases (GHGs) are taken into account; they are of natural and anthropogenic origin.

A key element that impinges on climate in a significant way is the energy of the solar radiation, which is received by the Earth and its atmosphere. Figure 3 illustrates the balance of the incoming and outgoing radiation.

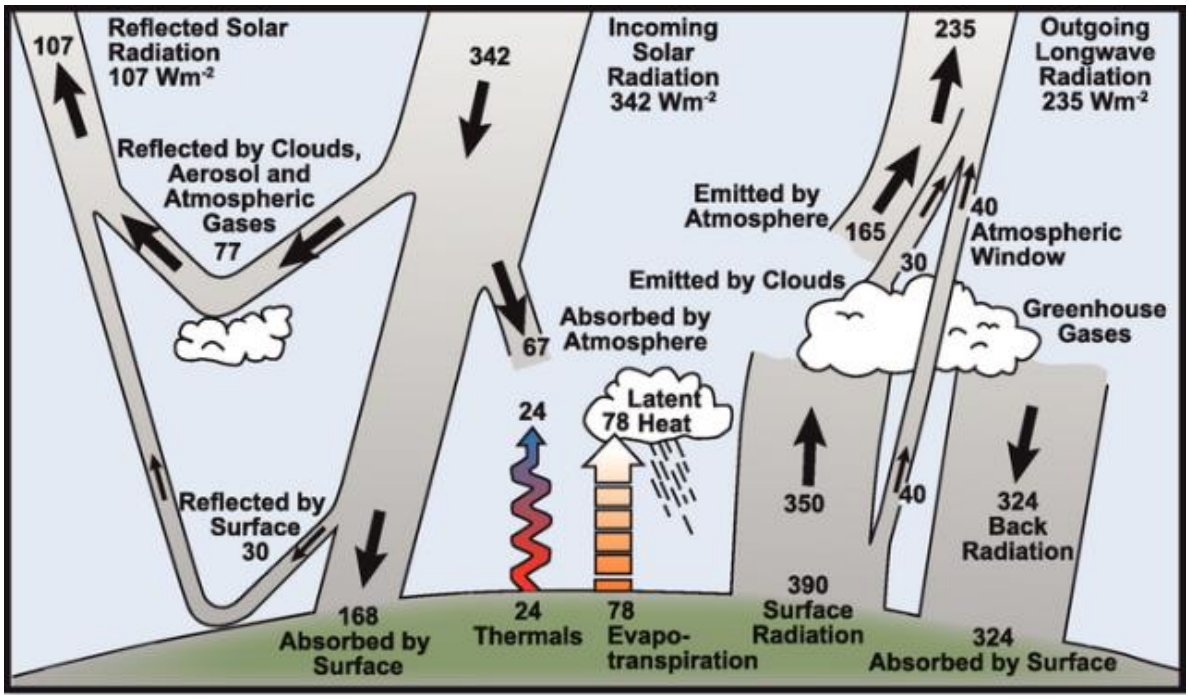

Figure 3: Estimated radiation budget of the Earth, whereby the values are averaged globally and annually and they are given in units watts per square metre [$W*m^{-2}$] taken from the IPCC report 2007 (Le Treut *et al.*, 2007; original source: Kiehl and Trenberth, 1997)).

As displayed in Figure 3, the average amount of Sun´s energy that reaches the Earth´s atmosphere is 342 $W*m^{-2}$. About 30 % of the incoming shortwave solar radiation is reflected back into outer space by clouds, aerosols and bright-coloured surfaces (albedo effect). Approximately one half of the incoming solar energy is absorbed by landmasses and oceans

and nearly 20 % by the atmosphere. The absorbed energy of the Earth´s surface is converted through thermal radiation and conduction with subsequent convection. It is released back into the atmosphere by warming the ground-level air with the Earth´s surface (thermals), as longwave radiation and due to evapotranspiration.

GHGs are essential for the life on Earth as we know it. GHGs such as carbon dioxide (CO_2), methane (CH_4) and nitrous oxide (N_2O) are IR active trace gases, which make a powerful contribution to the greenhouse effect. CO_2 is the GHG that occurs most frequently in the atmosphere. GHGs have the ability to function as thermal insulators in the troposphere. They absorb and reemit longwave radiation to all sides, also back down to the surface, resulting in a warming effect on the planet's surface. Due to their presence in the troposphere the heat is trapped, thus they can strongly affect the climate system. In fact without these GHGs, life on Earth would not be the same, since they ensure that the global mean surface temperature of the Earth is about +14 °C. In their absence, the temperature would be approx. -19 °C, thus GHGs are accountable for a temperature difference of 33 °C (Le Treut *et al.*, 2007).

Aside GHGs, water vapour and clouds are also able to interact with IR radiation via absorption and in turn emission (Seinfeld and Pandis, 1998, p. 33). After nitrogen and oxygen, water vapour can occur as the third most abundant gaseous constituent of the Earth´s atmosphere. In Figure 4 the absorption patterns of the two strongest IR active gases are displayed.

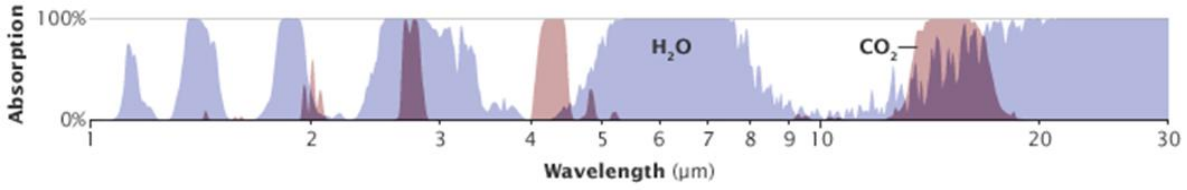

Figure 4: Absorption spectra of carbon dioxide (in red) and water vapour (in blue) in the near- and mid-IR range (source: Wikipedia)[3].

Clouds, along with water vapour, are the most important atmospheric components for reflection, absorption and emission of radiation (Seinfeld and Pandis, 1998, p. 1094). Hence

[3] By NASA, Robert Rohde - http://earthobservatory.nasa.gov/Features/EnergyBalance/page7.php NASA Earth Observatory, Public Domain, https://commons.wikimedia.org/w/index.php?curid=32288093 (28.11.2017)

clouds are deeply involved in the processes of the Earth´s energy balance. Some clouds trap the energy close to the surface resulting in warming our planet (see strong absorption bands of water in Figure 4), other clouds cool the Earth by reflecting off the incoming sunlight immediately (Seinfeld and Pandis, 1998, p. 4). However, in total clouds have an important net cooling effect on Earth´s surface.

The interactions of clouds with other factors such as aerosols are diverse and interconnected. As we see below (described in subchapter 1.3.1) several effects can thereby have an impact.

Nowadays the impact of human activities on global climate change is not to deny. IPCC is publishing a report periodically, including most recent studies and insights to analyse and quantify the influence of mankind on the resulting climate change. The strength and influence of a driver that change the radiation balance is expressed as radiative forcing. These external drivers (e.g. increased CO_2 concentration) cause a perturbation of the radiation balance and the change in net flux is quantified at the top of the troposphere. Radiative forcing is specified in units of heat flux [$W*m^{-2}$] (IPCC, 2007, p. 86; IPCC, 2013, pp. 13). Positive radiative forcing amplifies the warming trend (such as e.g. black carbon on snow leads to reduced albedo effect of white-covered surfaces) and negative radiative forcing damps warming (e.g. enhanced albedo effect due to increased release of sulphur dioxide (SO_2), which can be the precursor of light-scattering sulfate aerosol). (Seinfeld and Pandis, 1998, p. 1113)

The change in energy flux of 2011 is related to 1750, which can be considered as the start of the industrial revolution, since then the atmospheric composition changed markedly due to human activities.

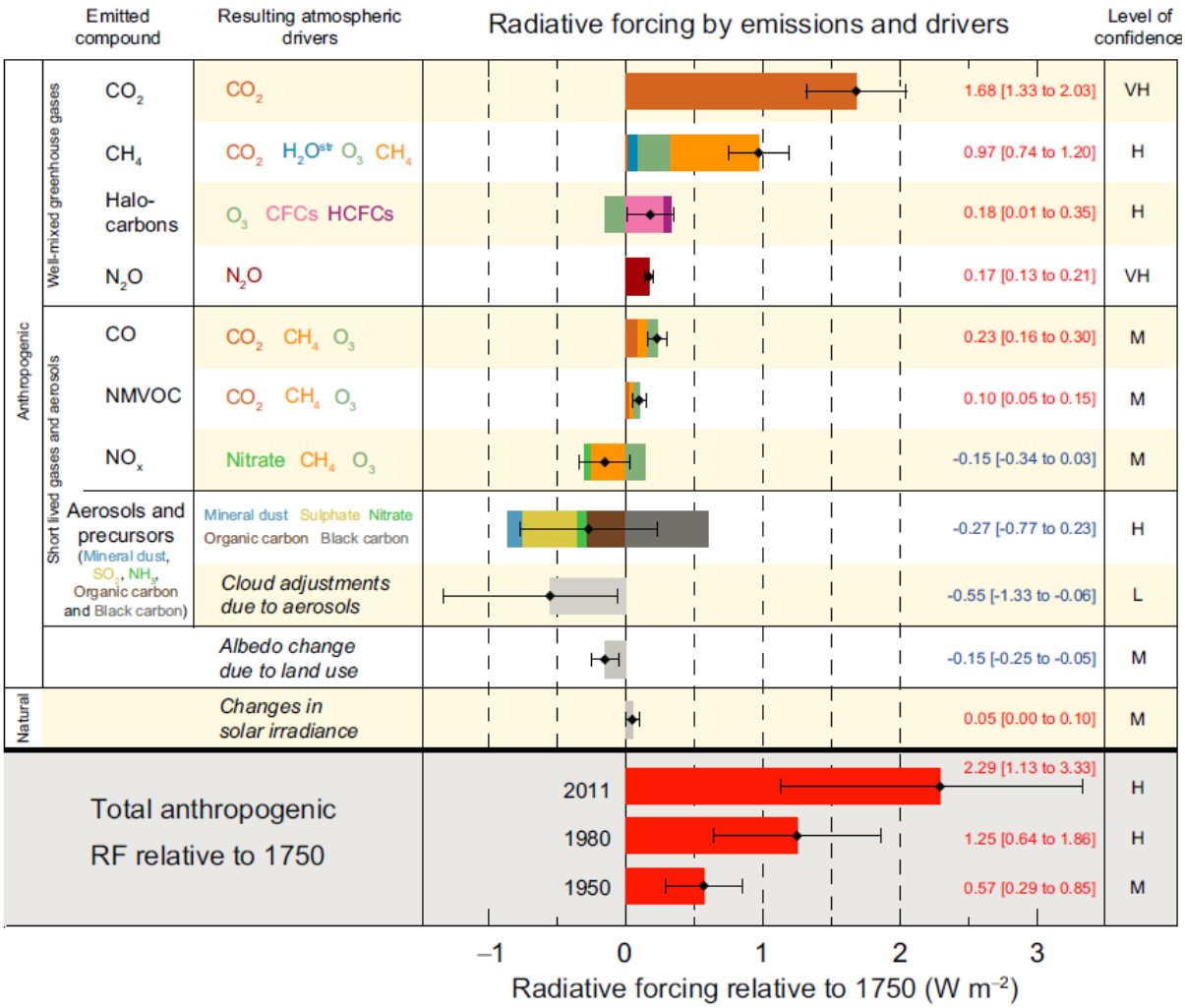

Figure 5: Global average radiative forcings caused by different external drivers (natural and anthropogenic) indicated together with the level of confidence (VH – very high, H – high, M – medium, L – low). Positive radiative forcing, leading to warming of the Earth´s surface is highlighted in red and negative forcing, which have a cooling effect, is highlighted in blue. Since 1750 the net radiative forcing is positive and the greatest contribution to that is attributable to the increased CO_2 concentration in the troposphere (adapted from IPCC, 2013, p. 14).

IPCC is using an ensemble of models that try to quantify the feedback of different drivers on Earth´s energy balance (IPCC, 2007). Climate modelling is highly complicated and many factors such as aerosol-cloud interactions contribute to large uncertainties to these calculations (Wang, 2013, p. 420). As displayed in Figure 5, the only factor that has a low level of confidence is the net cooling effect of clouds on Earth´s surface. This fact, that clouds have the single largest uncertainty at the present time indicates that plenty of scientific activity in cloud research including their radiative properties is still required.

1.3 Clouds

Clouds are visible aggregates of condensed water particles consisting of liquid droplets and/or frozen crystals that are suspended in the air. According to the World Meterological Organization (WMO) (WMO, 1975, p. 9) they may also comprise non-aqueous liquids or solid particles (e.g. dust, fume or smoke particulates).

In view of the fact that nearly all water vapour is located in the troposphere, clouds occur mainly there. However, under particular conditions clouds can be also found in the stratosphere and mesosphere.

1.3.1 Clouds in the Troposphere

Water exists in the atmosphere in several forms such as water vapour, snow, rain, dew, hail, graupel, fog, wet aerosol particles and clouds. On average clouds cover approx. 70 % of the sky above land area and 75 - 85 % above the oceans of our planet (Lohmann *et al.*, 2016, p. 1).

Clouds are an essential part of the Earth´s atmosphere, playing central roles in our climate system (Seinfeld and Pandis, 1998, p. 777). First of all clouds have a significant influence on Earth´s radiation budget. It is generally considered that higher clouds warm the Earth´s surface by acting as a greenhouse due to trapping longwave IR radiation in the lower atmosphere (greenhouse effect). This trapping effect is reduced by the fact that high altitude clouds, especially ice clouds, exhibit lower water content and therefore, a higher transparency. In comparison clouds in the lower atmosphere tend to have a large albedo effect and promote cooling of the planet´s surface by reflecting the Sun´s radiation back into space. (Seinfeld and Pandis, 1998, p. 1100) In general which of the two effects prevails for a particular cloud is depending on its microphysical properties, the cloud´s thickness, height, particle composition and on its surface albedo (Lohmann *et al.*, 2016, p. 329; Wang, 2013, pp. 414).

Moreover, clouds also have an important function in the hydrological cycle by transporting water from the atmosphere to the Earth´s surface, mainly as rain or snow. Besides soluble gases and aerosols can be scavenged from the atmosphere via wet deposition (water droplets, snow, ect.). Aqueous-phase chemical reactions and the formation of secondary species occur inside cloud droplets. The uptake of sulphur dioxide (SO_2) into cloud droplets

e.g. can lead to sulphate (SO_4) aerosols by oxidation (Lohmann *et al.*, 2016, p. 3). Furthermore, clouds can also facilitate vertical and horizontal motions of moisture, trace species and temperature in the atmosphere. (Seinfeld and Pandis, 1998, p. 777)

In 1803 Luke Howard classified on the basis of the Latin terms four elementary cloud forms as they appear to an observer on Earth´s surface: *cirrus*, *cumulus*, *stratus* and *nimbus* (Ahrens, 2007, p. 117). Cirrus means “curl” or “hair” in Latin. Cirrus clouds occur in high altitudes and are of thin and fibrous appearance. Cumulus is Latin for “heap”; these puffy and dense clouds emerge in groups well separated from each other. Stratus means “layer”; these clouds form horizontal layers. Rain-bearing clouds are indicated by nimbus, which means “violent rain” and these clouds can extend vertically over wide ranges.

According to the WMO (1975, p. 11) there exists ten types of tropospheric clouds (described in Table 1 and shown in Figure 6), also called *genera*. The types can be defined by the height at which they usually appear. The troposphere can be divided vertically into three levels: low (*strato*), middle (*alto*), high (*cirro*), whereby the level is referred to the height of the cloud base above Earth´s surface. However, the levels should be considered as slightly flexible, because they can overlap and differ with latitudes (Table 1).

Genera can be further distinguished into *species*, in terms of their shape and internal structure that compose it and into *varieties* related to particular properties such as transparency (WMO, 1975, p. 11).

Table 1: The ten cloud types and their typical heights of occurrence in polar regions, temperate regions and tropical regions (WMO, 1975, p. 15).

Level	Genera	Polar regions	Temperate regions	Tropical regions
high	Cirrus	3 - 8 km	5 - 13 km	6 - 18 km
	Cirrocumulus			
	Cirrostratus			
middle	Altocumulus	2 - 4 km	2 - 7 km	2 - 8 km
	Altostratus			
	Nimbostratus			
low	Stratus	From the Earth´s surface to 2 km		
	Stratocumulus			
	Cumulus			
	Cumulonimbus			

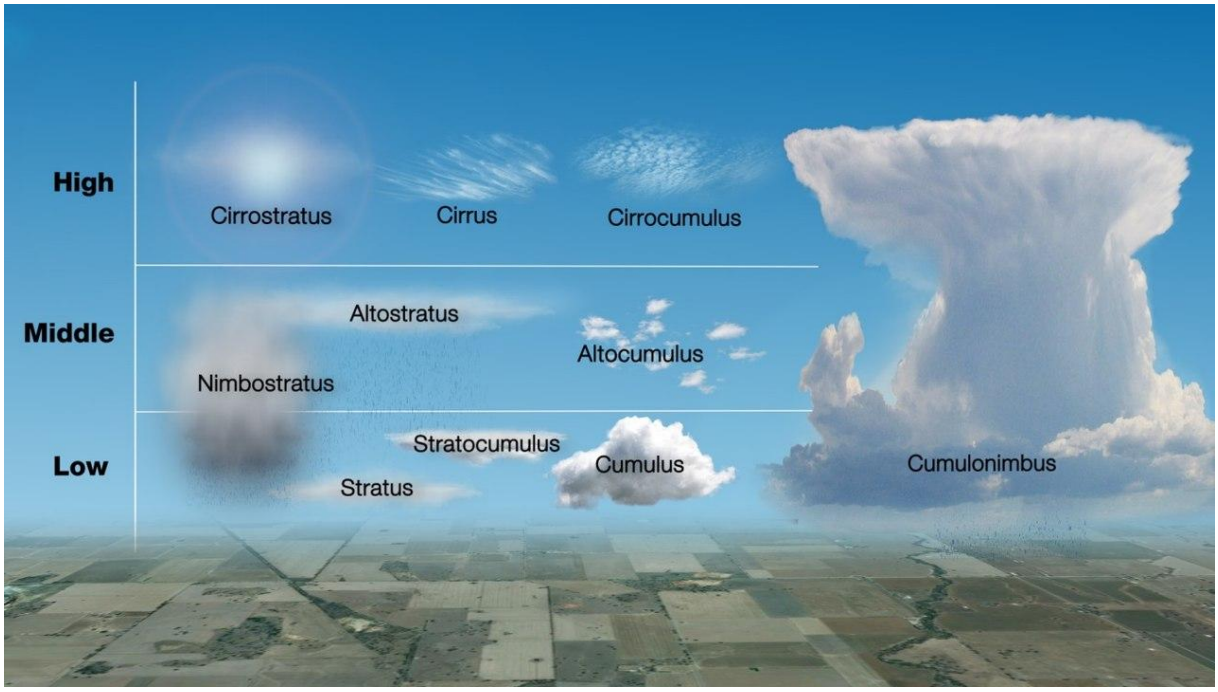

Figure 6: Illustration of the ten cloud types according to WMO and their height at which they usually appear (source: Wikipedia)[4].

Besides the categorization via their shape and their altitude, another classification can be related to their microphysical properties. On the basis of the water phase within the clouds, it can be distinguished between *warm* clouds, *ice* clouds or *mixed-phase* clouds. Warm

[4] By Christopher M. Klaus at w:en:Argonne National Laboratory - Own work by en:User:Klaus, Public Domain, https://commons.wikimedia.org/w/index.php?curid=2760873 (28.11.2017)

clouds are composed entirely of liquid droplets. They can occur at plus degrees and as well below 0 °C even up to nearly -38 °C, as long as no particles, so called ice nucleating particles (INPs) (Vali *et al.*, 2015) are present that trigger ice formation (Lohmann *et al.*, 2016, p. 15) (described in subchapter 1.4).

Water droplets that remain in the liquid state below 0 °C are referred to as supercooled water. According to Wang (2013, p. 28) approx. 40 % of the clouds still consist of supercooled water droplets at -12 °C. At temperatures of approx. -38 °C homogeneous nucleation (described in subchapter 1.4) takes place and therefore no warm clouds can be found below these temperatures. Ice clouds (e.g. cirrus) comprise purely of ice crystals and they can emerge at temperatures up to 0 °C, since this temperature marks the melting point of water. As the name already suggests, mixed-phase clouds consist of a mixture of liquid droplets and ice crystals. Stratus and cumulus are low-level clouds and dependent on several factors such as temperature; they can be warm clouds, ice clouds or mixed-phase clouds (Lohmann *et al.*, 2016, p. 3). Rain-bearing clouds (e.g. cumulonimbus) can contain water droplets as well as ice crystals of different sizes (Wang, 2013, p. 28). Fog can be denoted as ground-touching cloud, it can consists of water vapour, ice crystals or a mixture of both (Ahrens, 2007, p. 117).

Condensation is the general process of forming a cloud, a required condition for it is supersaturation of water vapour in an air parcel. The saturation ratio is defined by Equation 2:

$$S_i = \frac{p_{H_2O}}{p^S_{H_2O}(T)}$$

Equation 2

S_i	Saturation ratio [-]
p_{H_2O}	Partial pressure of water [Pa]
$p^S_{H_2O}(T)$	Saturation vapour pressure of water in equilibrium with its liquid state at temperature T [Pa]

Thereby three basic sections of saturation exists, water vapour is supersaturated if $S_i > 1$, saturated if $S_i = 1$ and subsaturated if $S_i < 1$. (Seinfeld and Pandis, 1998, pp. 545)

Supersaturation is usually achieved by cooling down an air parcel with high humidity. At lower temperatures, the saturation water vapour concentration decreases, resulting in higher relative humidity (RH) within the air parcel. Cloud formation can occur as soon as the ambient RH of an air parcel is overstepping 100 %. There are two main mechanisms to cool down an air parcel in the atmosphere, initiating cloud formation. Cooling down can occur due to mixing of two air masses or radiative losses of energy under constant pressure (isobaric cooling). Another way is adiabatic cooling, which takes place by uplifting of an air parcel with nearly no heat transfer with its environment. As pressure decreases with increasing altitude, the air parcel expands and its temperature declines. (Seinfeld and Pandis, 1998, p. 794)

By cooling down an air parcel, water vapour is able to condensate. During the condensation process, enthalpy of vaporization is released. This leads to a slower cooling rate and therefore the cloud can ascend further.

Theoretically, condensation can take place either in pure vapour (homogeneous condensation) or under the presence of foreign particles (heterogeneous condensation). However, cloud formation via homogeneous condensation is almost impossible, since supersaturation conditions of 400 % (Caballero, 2014, p. 4-2) are required. The dominant formation of cloud droplets in the atmosphere takes place due to heterogeneous condensation (Wang, 2013, pp. 156). Therefore foreign particles, also known as cloud condensation nuclei (CCNs), are necessary. The surface of CCNs is able to attract water and reduce the necessary energy to form a droplet. These particles have either soluble (e.g. sea salt, sulphate) or hydrophilic (e.g. mineral dust) properties (Lohmann *et al.*, 2016, p. 155). Size and chemical composition are significant for their ability to act as CCN (Seinfeld and Pandis, 1998, p. 793).

In contrast, the formation of ice clouds is less clear (Wang, 2013, p. 157). There are two possibilities: Ice crystals can be formed

- either directly by conversion from water vapour (deposition nucleation) - without passing through the liquid phase - onto appropriate particles, the INPs,
- or freezing by going through the supercooled liquid phase (ice nucleation) (described in subchapter 1.4).

In this field of research, the fundamental understanding is still lacking (Murray *et al.*, 2012).

1.3.2 Upper Atmospheric Clouds (Clouds in the Stratosphere and Mesosphere)

Stratosphere

As already mentioned, the stratosphere contains less water vapour and hence cloud formation is just possible under particular conditions. In extremely cold polar nights (as low as -90 °C) attributable to the vortex in the Antarctica (south pole) and Arctic (north pole), polar stratospheric clouds (PSCs) can occur, they are located in the lower (15 to 20 km altitude) and also colder part of this layer (Seinfeld and Pandis, 1998, pp. 192). An example for PSCs, which are also known as nacreous clouds, is illustrated in Figure 7. They can consist either of nitric acid trihydrate (Type Ia); nitric acid, sulphuric acid and ice water (Type Ib); or pure ice water (Type II) (Seinfeld and Pandis, 1998, p. 193).

Figure 7: Polar stratospheric clouds in the Antarctica (source: Wikipedia)[5].

Mesosphere

Noctilucent clouds, which are also known as night clouds are present occasionally in the mesosphere. They are the highest located clouds in the atmosphere and consist of ice crystals, whereby the water source is not known for certain[6] (Kulikov *et al.,* 2009). The

[5] By Alan Light from Charlotte, USA. At Commons: Alan R Light (talk · contribs) - Nacreous Clouds over the NASA Radome -4-Uploaded by Hike395, CC BY 2.0, https://commons.wikimedia.org/w/index.php?curid=14503960 (22.10.2017)

[6] http://www.atoptics.co.uk/highsky/nlc2.htm (26.2.2018)

occurrence of noctilucent clouds takes place under restricted conditions and they can only be seen at twilight, because of their faint form as illustrated in Figure 8.

Figure 8: Noctilucent clouds in Estonia (source: Wikipedia)[7].

1.4 Ice Nucleation

Nucleation is the initial step of the transition into a new thermodynamic phase or a new structure and happens by self-organization. In the case of ice formation, hexagonal ice is the thermodynamically favoured phase at temperatures below 0 °C and standard pressure. However, as temperatures fall below 0 °C, ice formation is typically not initiated instantly, as the phase transition is kinetically hindered, leading to water in the supercooled state. In order to freeze, water needs to surpass an energy barrier (Lohmann *et al.*, 2016, p. 155). Supercooled water can occur frequently in the Earth´s troposphere down to temperatures of approx. -37 °C (Murray *et al.*, 2010b).

A required condition for the ice crystal formation is the supersaturated metastable state of a parent phase. In the case of supercooled water the process is denoted as freezing. Ice can also be formed from supersaturated vapour. This process is known as deposition nucleation. The focus of this subchapter is on the phase transition of supercooled water to ice.

[7] By Ireen Trummer - Own work, CC BY-SA 4.0, https://commons.wikimedia.org/w/index.php?curid=37064834 (23.1.2018)

Ice nucleation can happen by two different mechanisms, which are known as homogeneous and heterogeneous nucleation. Homogeneous ice nucleation is the ice crystal formation of a new ice phase, which arises entirely from a pure metastable parent phase via self-assembly of the water molecules. No foreign substances are involved in this process. In contrast heterogeneous ice nucleation occurs in the presence of interfering foreign substances, which are referred to as INPs. INPs can catalyse the freezing process by lowering the nucleation barrier and therefore heterogeneous ice nucleation occurs at higher temperatures than homogeneous ice nucleation.

1.4.1 Homogeneous Ice Nucleation

In the absence of INPs, liquid water in small quantities (as e.g. droplets present in the troposphere) can be supercooled down to temperatures of approx. -37 °C (Murray *et al.*, 2010b).

There is a constant formation and cleavage of intermolecular hydrogen bonds in the liquid water phase due to thermal agitation. However, in order to form hexagonal ice, the molecules have to be arranged into a well ordered structure. This results in the kinetic inhibition of ice formation at higher sub-zero temperatures. In hexagonal ice, each water molecule is connected via hydrogen bonds to its four closest-neighbour water molecules. As the majority of solid water occuring in our biosphere is hexagonal ice, it is referred to as “ice” in this thesis. (Pruppacher and Klett, 2010, pp. 78)

The standard model to describe homogeneous nucleation is the classical nucleation theory (CNT). It is applied to provide an appropriate description of the homogeneous freezing in a simplified way. Hereby CNT relies on quasi-bulk thermodynamics to approximate the process (Wang, 2013, p. 158) and it can be applied for constant temperature and pressure. Applied on freezing it describes the formation of ice clusters in the supercooled parent phase. A cluster smaller than the critical size is specified as *embryo,* above the critical size it is denoted as *germ*. Close to saturation ($S_i = 1$) (see Equation 2), water molecules start to assemble small ice embryos containing n-molecules (n = 1, 2, 3, 4) caused by random fluctuation (Caballero, 2014, p. 4-3, p. 4-6). Larger embryos are short-lived, due to the unfavourable surface-to-volume ratios. As a result they dissipate back to the liquid phase rather quickly. Germs on the other hand are large enough to gain a more favourable surface-

to-volume ratio and therefore are able to grow. The critical size of a cluster is dependent on temperature. At -5 °C the critical cluster has to comprise of 45.000 water molecules, while at -40 °C only 70 molecules are required to initiate stable growth (Zachariassen and Kristiansen, 2000). At supersaturated conditions ($S_i > 1$) the cluster has the tendency to grow stable, since these conditions lower the chemical potential and therefore the Gibbs free energy of the entire system. The related Gibbs free energy change of the phase transition liquid-ice can be obtained with the CNT (see Equation 3), whereby a spherical cluster of radius r is formed. It is typically written as (Seinfeld and Pandis, 1998, pp. 520, pp. 556; Murray *et al.*, 2012):

$$\Delta G_{cluster} = \Delta G_{surface} - \Delta G_{volume}$$
$$= 4\pi\gamma r^2 - \frac{4\pi}{3}\frac{kT\ lnS_i}{v}r^3$$

Equation 3

$\Delta G_{cluster}$	Gibbs free energy for cluster formation [J]
$\Delta G_{surface}$	Gibbs free energy related with interface formation [J]
ΔG_{volume}	Gibbs free energy related with intermolecular water bond formation within the cluster [J] ($\Delta G_{volume} < 0$ if $S_i > 1$)
γ	Surface tension between liquid water and ice [$N*m^{-1}$]
r	Radius of the cluster [m] (assumption of sphericity)
k	Boltzmann constant: $1.38 * 10^{-23}$ [$J*K^{-1}$]
T	Temperature [K]
v	Molecular volume of ice [m^3*mol^{-1}]
S_i	Saturation ratio [-] ($S_i = P_l/P_{ice}$)
P_l	Vapour pressure of liquid water [Pa]
P_{ice}	Vapour pressure of ice [Pa]

Equation 3 consists of two major terms. The first ($\Delta G_{surface}$) is the Gibbs free energy required to form a new surface within the supercooled parent phase, it is always positive and has therefore a destabilising effect on the phase transition process. The second (ΔG_{volume}) is the Gibbs free energy resulting from the decrease in chemical potential by forming bonds within the cluster. At supersaturated conditions ($S_i > 1$), the associated change in Gibbs free energy of the volume term plays a stabilising role. For small r, the surface term (proportional to r^2)

overbalances, because of the high surface tension γ. For bigger cluster, the volume term (proportional to r^3) starts to dominate the equation, indicating stability of the cluster. The resulting Gibbs free energy of forming a cluster has a maximum, which represents the energy barrier of forming the new ice phase (Figure 9). This energy barrier plays a key role in phase transition, because it controls the kinetics and therefore the probability of ice formation from a parent phase (Lohmann *et al.*, 2016, p. 155). While the position of the maximum depends on the temperature, its height is strongly influenced by the saturation ratio S_i and surface tension γ.

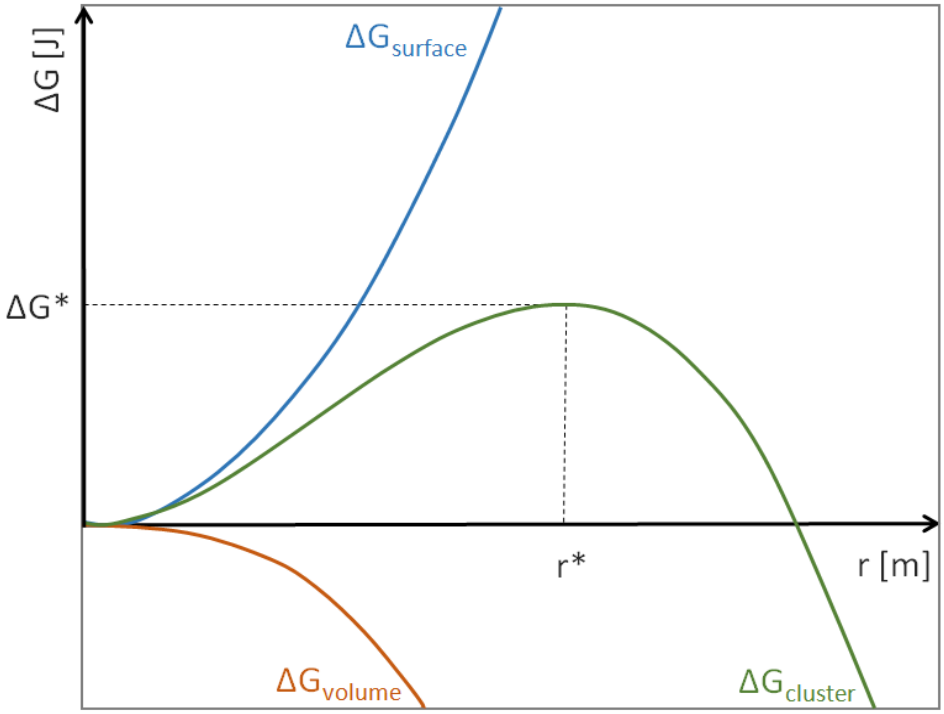

Figure 9: Change in Gibbs free energy ΔG for homogeneous nucleation of a cluster with the radius r at S_i = 1.01, thereby r* is the critical radius (adapted from Lohmann *et al.*, 2016, p. 161).

The energy barrier marks the critical radius r* (Equation 4) and the critical Gibbs free energy ΔG* (Equation 5) and has to be exceeded that a cluster can grow stable.

$$r^* = \frac{2\gamma v}{kTlnS_i}$$

Equation 4

$$\Delta G^* = \frac{16\pi\gamma^3 v^2}{3(kTlnS_i)^2}$$

Equation 5

Homogeneous ice nucleation occurs spontaneously and is therefore a stochastic process. The probability of nucleation events per unit volume and per unit time can be described by the homogeneous nucleation rate coefficient J_{hom}. Equation 6, which exhibits a typical Arrhenius style, shows the relation of J_{hom} at which ice crystals arise from metastable liquid water with the necessary Gibbs free energy of forming a critical cluster. (Murray *et al.*, 2012)

$$J_{hom} = A\ exp\left(-\frac{\Delta G^*}{kT}\right)$$

Equation 6

A Pre-exponential factor [$cm^{-3}{*}s^{-1}$]

J_{hom} Homogeneous nucleation rate coefficient [$cm^{-3}{*}s^{-1}$]

With decreasing temperature, the required energy of forming an ice germ decreases and therefore the probability of ice formation rises (Murray *et al.*, 2011). The larger the droplet thereby is, the less it can be supercooled before the freezing event happens. In larger droplet volumes, the likelihood for density fluctuations is enhanced and therefore also the probability for ice germ formation. Also time plays a role, as it is a stochastic process. With increasing time, the probability of freezing events increases. (Pruppacher and Klett, 2010, pp. 211) An important factor in the statistical process of homogeneous ice nucleation correlates with volume, time and temperature, and also with the cooling rate (Dorsch and Hacker, 1950; Levine, 1950; Bigg, 1953; Vali and Stansbury, 1966). In general slower cooling rates are leading to higher temperatures of the freezing event (Bigg, 1953; Murray *et al.*, 2010b).

Under isothermal conditions the three factors volume, time and temperature can be integrated in Equation 6, leading to the form (Murray *et al.*, 2010b):

$$\ln\left(\frac{n_{liquid}}{n_{total}}\right) = \ln(1 - f_{ice}) = -J_{hom}Vt$$

Equation 7

n_{total} Number of total droplets (liquid and frozen) [-]

n_{liquid} Number of liquid droplets at temperature T [-]

f_{ice} Fraction of frozen droplets at temperature T [-]

J_{hom} Homogeneous nucleation rate coefficient [$cm^{-3} * s^{-1}$]

V Volume of a droplet [cm^{-3}]

t Observation time [s]

whereby f_{ice} is given by Equation 8:

$$f_{ice} = \frac{n_{frozen}}{n_{total}}$$

Equation 8

n_{frozen} Number of frozen droplets [-]

1.4.2 Heterogeneous Ice Nucleation

Heterogeneous ice nucleation takes place in the presence of foreign substances acting as INPs. INPs exhibit active sites, which stabilise the newly formed ice clusters due to a reduction of the energy barrier. This process can be understood as catalysis of ice formation. Four theoretical modes of heterogeneous ice nucleation (Figure 10) are currently used and the freezing temperature is quite specific for each mode (Pruppacher and Klett, 2010, p. 309; Murray *et al.*, 2012):

- Deposition nucleation takes place when ice is formed directly onto a deliquescent[8] surface of an INP at supersaturated conditions regarding to ice.
- Immersion freezing occurs on a solid INP, which is suspended inside a supercooled droplet.
- Condensation freezing, in which first water vapour condensates onto deliquescent particles (CCNs), which also act as INPs and freezing is initiated.
- Contact freezing, which is initiated due to collision of an INP with a supercooled water droplet.

[8] Property of some solid aerosols consisting of a salt mixture: they can absorb moisture from the atmosphere at high RH (Seinfeld and Pandis, 1998, p. 514).

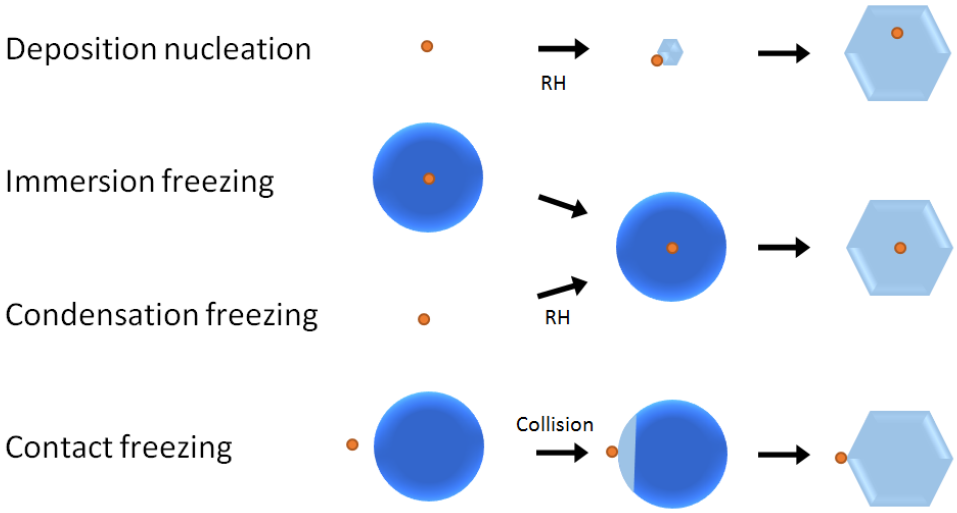

Figure 10: Schematic illustration of the four heterogeneous freezing modes.

In mid- and low-level clouds the most predominant mechanisms for ice formation are immersion freezing (Murray *et al.*, 2012) followed by contact freezing (Phillips *et al.*, 2007). All results presented in this thesis refer to immersion freezing.

Heterogeneous ice nucleation can be described quantitatively either by using *stochastic* (time-dependent) or *singular* (temperature-dependent) approaches. In the stochastic model the probability of heterogeneous nucleation events per unit surface area σ of the solid INPs immersed in the droplet per unit time, can be expressed with the heterogeneous nucleation rate coefficient J_{het} (Equation 9). In comparison to J_{hom}, J_{het} is volume independent, but dependent on the INP quantity and INP surface area in the droplet. (Murray *et al.*, 2011)

$$\ln(1 - f_{ice}) = -J_{het}\sigma t$$

Equation 9

J_{het} Heterogeneous nucleation rate coefficient [$cm^{-2}*s^{-1}$]

σ Surface area [cm^2]

Assuming an even distribution of the INPs in the liquid phase, a larger droplet contains more INPs as a smaller one and freezes therefore at higher temperatures (Hartmann *et al.*, 2016). In statistical terms there is hence a certain dependence on the volume of the droplet. For such systems with INPs evenly distributed in the liquid, the surface area can be replaced by the volume, whereby both J_{hom} and J_{het} have then the same unit [$cm^{-3}*s^{-1}$].

An alternative way of describing heterogeneous ice nucleation is the singular theory (Vali, 1971, 1994; Pruppacher and Klett, 2010; Murray *et al.*, 2012) developed by Levine (1950) and Langham and Mason (1958). In this model it is assumed that every INP, which is incorporated in the water droplets (immersion freezing mode), has its characteristic freezing temperature at which freezing takes place. INPs have individual active nucleation sites on their surface, which serve as ice phase templates and where heterogeneous ice nucleation is consequently initiated due to ice embryo formation and growth. The active nucleation sites of a particle are responsible for its ice nucleating ability and become activated at a specific temperature. If several different INPs are present in one droplet, the freezing process will be initiated by the most active INP, which is the particle that has the highest characteristic freezing temperature (Pruppacher and Klett, 2010, pp. 350). Compared to the characteristic freezing temperature, the time dependence can be regarded as negligible (Murray *et al.*, 2011). Equation 10 describes the ice formation that occurs at a certain active nucleation site of a certain INP at a specific temperature (Murray *et al.*, 2012).

$$f_{ice}\ (\mathrm{T}) = \frac{n_{frozen}\ (T)}{n_{total}} = 1 - \exp\left(-n_s\ (T)\ s\right)$$

Equation 10

$f_{ice}\ (\mathrm{T})$	Fraction of frozen droplets at temperature T [-]
$n_{frozen}\ (\mathrm{T})$	Number of frozen droplets at temperature T [-]
n_{total}	Number of total droplets (liquid and frozen) [-]
$n_s\ (\mathrm{T})$	Active site density (number of nucleation sites per surface area) [cm^{-2}]
s	Nucleant surface area per droplet [cm^2]

Although these two models are well known, and are well applicable in most cases, they do not always match adequately with the experimental results. For this reason other models have been introduced to picture the complex freezing process in a more accurate way. One example is the soccer ball model, in which the surface of INPs are covered with different active nucleation sites, whereby each site has a different energy barrier for the ice cluster formation that is controlled by stochastics (Niedermeier *et al.*, 2011).

1.5 Aerosols

Atmospheric aerosols are tiny liquid or solid particles which are dispersed in air. They are either of natural or anthropogenic origin. Their concentrations vary widely in geographical areas (e.g.: arid, marine, urban regions) and time (e.g.: dry or wet season) (Seinfeld and Pandis, 1998, pp. 1113). Aerosol particles can be described by their physical and chemical properties (Lohmann *et al.*, 2016, p. 115). The size of aerosol particles is an important property, as it defines the atmospheric lifespan (Seinfeld and Pandis, 1998, p. 408) as well as possible health effects (Zimmermann, 2015), and typical sizes are ranging between 0.01 and 10 µm (IPCC, 2007, p. 76). In general, the residence time of larger aerosol particles in the atmosphere is lower, since they have larger sinking velocieties. The chemical composition of aerosol particles is highly variable, ranging from particles consisting of one single compound (e.g. pure sulphuric acid) to those that are composed of a high quantity of chemical substances (e.g. combustion-formed carbonaceous compounds).

Due to the presence of electromagnetic radiation and the highly oxidizing property of our atmosphere, aerosol particles are subjected to aging processes. Besides photochemical reactions, oxidation, and uptake of or reaction with other chemicals (e.g. uptake of gaseous ammonia by a liquid sulphuric acid particle) physicomechanical conversions (e.g. collision and coagulation with other particles) of the aerosol particles can occur, whereby the original particle properties are modified (Lohmann *et al.*, 2016, p. 143).

Atmospheric particles can be divided into primary and secondary aerosols. Primary particles are released into the atmosphere by direct emission. Sources of primary aerosol particles are for instance arid regions for mineral dust, combustion processes (biomass, fossil fuels) for black carbon or the emission of pollen and fungal spores from the biosphere (Lohmann *et al.*, 2016, p. 129). Other primary biological aerosol particles in the atmosphere are e.g. bacteria, viruses and small parts of animal and plant matter (Murray *et al.*, 2012). In contrast, secondary particles are generated from gaseous precursor substances via gas-to-particle conversion (e.g. production of ammonium nitrate from ammonia and nitric acid or formation of secondary organic aerosols).

Aerosol particles are of pivotal importance for cloud formation (subchapter 1.3.1). Particle properties such as the physical state of aerosols have a significant impact on its capability to act as a CCN or INP (Lohmann *et al.*, 2016, p. 116). The chemical composition of aerosol particles and its size are crucial factors. INPs are only a minor fraction of aerosol particles

and they can be found therefore rarely in the atmosphere (Murray *et al.*, 2012). Their atmospheric presence is hard to predict, as INPs originate from many different sources. Some efforts were made to find out what characteristics are necessary for a particle to be a good INP. Pruppacher and Klett (2010, pp. 326) reported the following requirements for effective INPs: (i) insolubility: INPs are typically insoluble in water, (ii) size: a positive correlation between the number of INPs and larger (> 0.1 µm in diameter) aerosol particles was found (DeMott *et al.*, 2010; Pruppacher and Klett, 2010, pp. 326) (iii) chemical bond requirement: water molecules must have the ability to form chemical bonds with the surface of the INP and (iv) crystallographic requirement: an effective INP should have an ordered geometric structure to match the ice structure. However, several investigations of the research community suggest that for some of the mentioned requirements exceptions exist. For instance, Zuberi *et al.* (2001) reported that soluble ammonium sulphate salt induces ice nucleation in the immersion freezing mode. Non-crystalline materials such as soot (DeMott, 1990), glassy aerosols (Murray *et al.*, 2010a) and organic aerosol particles (Knopf *et al.*, 2010) trigger ice formation despite their amorphous structure. So far, no satisfactory approach has been found to characterize requirements for potent INPs. Currently the only option to find out if a particular substance is a good ice nucleating material is to carry out quantitative experiments. (Murray *et al.*, 2012)

There are four main classes of aerosols that catalyse ice formation in the atmosphere (Murray *et al.* 2012):

- Mineral dust (e.g. kaolinite, illite, Arizona Test Dust (ATD))
- Biological material (e.g. fungal spores, bacteria, pollen, alga, diatom)
- Carbonaceous combustion aerosols (e.g. soot)
- Volcanic ash

The ice nucleating ability of these atmospheric particles extends over a wide temperature range as illustrated in Figure 11. Biological ice nucleating agents such as bacteria (e.g. *Psyeudomonas syringae*) are the most effective INPs as they can trigger ice formation at high subzero temperatures close to 0 °C (orange frame). In the middle temperature region (light green frame), birch pollen, soot, and various dust and volcanic ash types start to catalyse

freezing. In the strongly supercooled region (light blue frame), marine organisms such as alga and diatom, as well as fungal spores initiate ice nucleation.

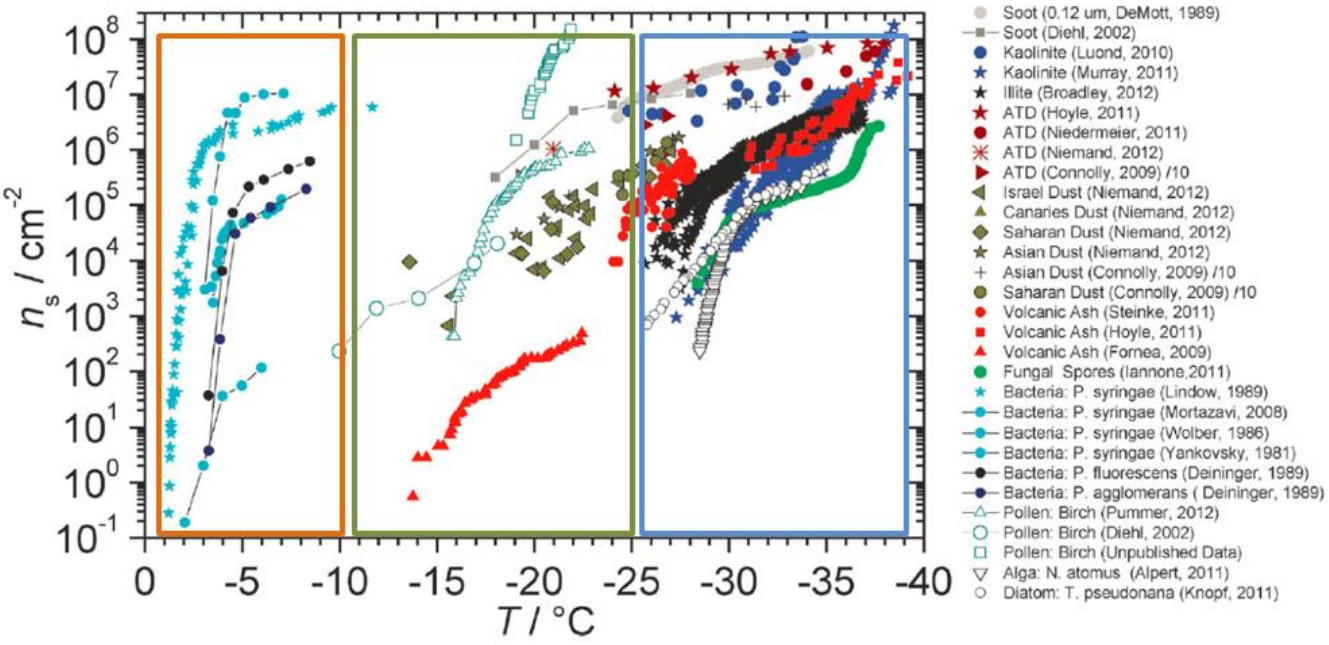

Figure 11: Ice nucleating activity (INA) expressed as active site density of different atmospheric aerosol particles immersed in water (n_s). This summary plot is based on literature data; (adapted from Murray *et al.*, 2012).

1.6 Ice Nucleation and Antinucleation in Nature

On Earth it can get unpleasantly cold in specific temperature zones (especially in the temperate and frigid zone, see Figure 12) and during the cold seasons of the year. When temperatures drop below 0 °C, it is necessary for the survival of plants to have coping mechanisms to deal with the cold.

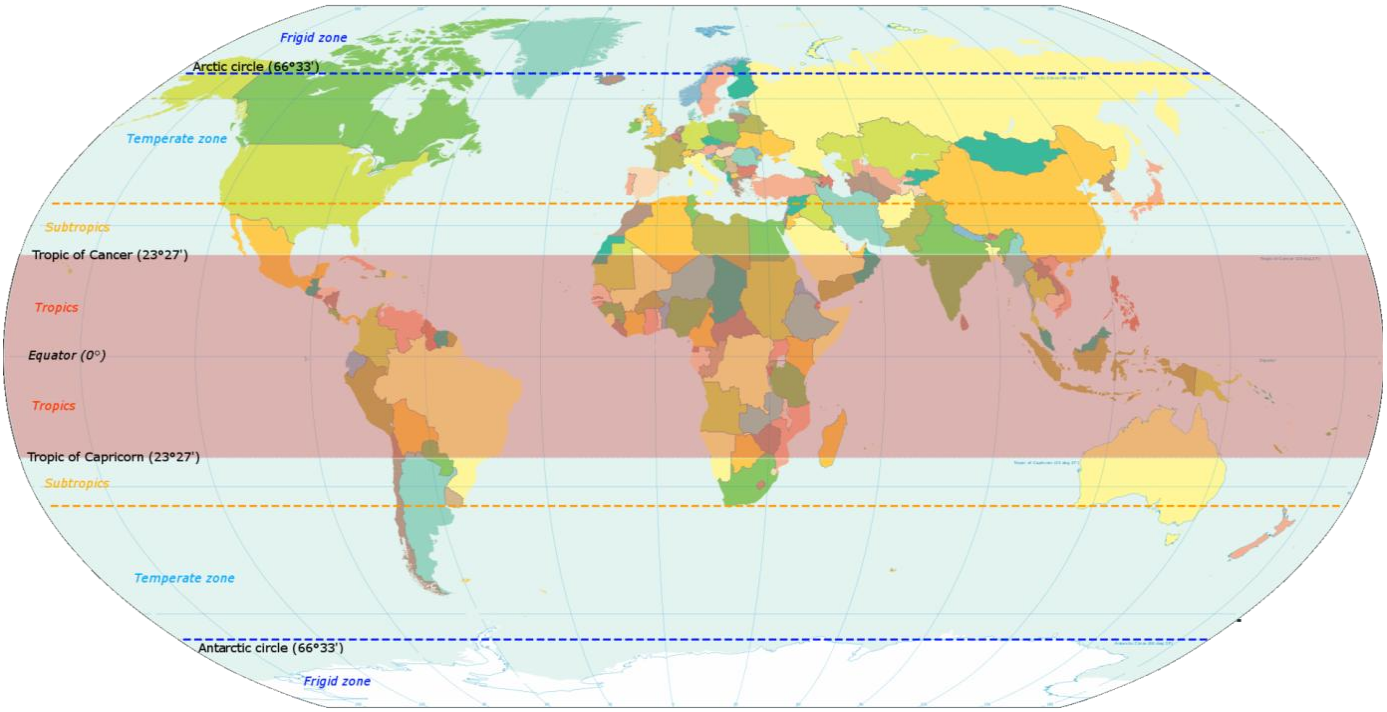

Figure 12: The different climatic zones of the Earth: frigid zone, temperate zone, subtropical zone, tropical zone (source: wikipedia[9]).

Freezing of plant tissues is usually lethal, harmful frost injuries are for instance caused by rupture of cellular structures or when dehydration surpasses a critical level (Asahina É., 1956, p. 114). In nature there are two main cold hardiness mechanisms of plant species, they are either develop *freeze tolerance* or *freeze avoidance* (Zachariassen and Kristiansen, 2000; Storey and Storey, 2005, pp. 474).

Plant species that are freeze tolerant act by the competing phenomenon of controlled ice nucleation in certain spaces. In general freezing of frost tolerant plants take place in extracellular spaces (Burke *et al.*, 1976). Ice formation can be induced in plants via *extrinsic* (foreign substances, not plant derived) or *intrinsic* (plant derived substances) ice nucleating agents. An example for an extrinsic ice nucleator is *Pseudomonas syringae*, whereby a special membrane bound protein has been identified as its ice nucleating active site (Lindow *et al.*, 1989). The production of intrinsic ice nucleating agents is a prominent frost protection mechanism for plants (Burke *et al.*, 1976; Pearce, 2001). Several studies (Kieft, 1988; Constantinidou and Menkissoglu, 1992; Brush *et al.*, 1994; Lundheim and Wahlberg, 1998) suggest that INPs can be produced by plants. These effective INPs have been found in the

[9] By KVDP - Own work, CC BY-SA 3.0, https://commons.wikimedia.org/w/index.php?curid=27385077, via Wikimedia Commons (18.12.2017)

extracellular liquid. According to Asahina (1956, p. 113) and Zaragotas *et al*. (2016) some plants can survive extracellular freezing, depending on several factors, intracellular freezing however is almost always lethal. In general there exists an osmotic equilibrium between the cells and the extracellular solution that surrounds them, meaning that the concentration of osmotically active solutes in both spaces is equal. During extracellular ice formation, water molecules are removed from the extracellular fluid, leading to higher concentrations of the solutes. To maintain this isosmotic state a water efflux from the cells takes place to the frozen compartments. This process causes shrinking of the cells. This increases the salt concentration within the cells, preventing ice crystal formation due to freezing point depression. If temperature falls so low that the water within the cells freezes, the high salt concentrations propagate vitrification rather than ice crystal formation, increasing the chance of survival (Storey and Storey, 2005, pp. 474).

The second cold hardiness strategy is the freeze avoidance mechanism, which works due to stabilization of the deep supercooled state of fluids in an organism. This metastable state can be preserved through accumulation of various antifreeze substances or by eliminating/inhibiting ice nucleating agents from/in the system. In response to the cold temperatures, wintering plants typically produce such antifreeze substances at least in some compartments of their tissues. These substances can be osmotically active molecules, for instance soluble sugars, lipids, acids (amino, organic) and polyamines (Guy *et al.*, 2008). Such compounds exhibit colligative properties and can lead to a freezing point depression. On the other hand, there are compounds such as proteins that interact via hydrogen bonding with nascent ice crystals, counteracting crystal growth and recrystallization of ice and therefore minimizing the freezing injuries. Antifreeze proteins (Urrutia *et al.*, 1992; Griffith and Yaish, 2004) are acting noncolligatively and can be divided into two groups: entire proteins, which are called antifreeze proteins (AFPs), whereas others contain carbohydrate chains that are attached to the protein, which are referred to as antifreeze glycoproteins (AFGPs) (Zachariassen and Kristiansen, 2000). The mode of action of these proteins is similar, although they have different structures. If AFPs or AFGPs bind to the surface of ice crystals, they will convert the crystal front from a slightly into a highly curved surface and therefore will inhibit ice propagation due to an extreme increase of the surface free energy (subchapter 1.4.1). Consequently these proteinaceous compounds are able to form an energy barrier for the progressive ice formation process. (Storey and Storey, 2004)

1.7 Biological INPs and State of the Art

The extent and influence of biological material, which serves as INPs in the Earth´s atmosphere is not completely clear at present time. Pratt *et al.* (2009) sampled ice crystal residues from ice clouds over Wyoming at about 8 km height and analysed the composition of those residues by aerosol mass spectrometry. They found that one third of the material was of biological origin and approx. 60 % of the found mineral dusts were internally mixed with biological and/or humic matter. However these results were questioned due to the reliability of the measurement techniques (Cziczo *et al.*, 2017). Huffman *et al.* (2013) showed a significant enhancement of the biological particle concentration in the air within a forest ecosystem during and after rain events to which they were able to link an increase in the INP concentration. This indicates a correlation between rain, bioaerosols, and biological INPs in the atmosphere.

As mentioned previously in subchapter 1.5 biological INPs can be found in many kingdoms of life. Various types of bacteria (Maki *et al.*, 1974; Lindow *et al.*, 1978; Lindow *et al.*, 1989) as well as fungi (Pouleur *et al.*, 1992) and lichens (Kieft, 1988) were found to trigger ice formation. The most effective biological INP originates from the bacterium *Pseudomonas syringae*, which initiates ice nucleation at high subzero temperatures (-1.8 to -3.8 °C) (Maki *et al.*, 1974). This bacterium grows on the surface of various plants (epiphytic organism) and is using ice nucleation and the following freeze injuries for access to plant nutrients (Zachariassen and Kristiansen, 2000). The active site of this bacterium has been identified as a protein that is linked to its outer membrane layer (Maki *et al.*, 1974; Govindarajan and Lindow, 1988; Lindow *et al.*, 1989). The ice nucleating protein is believed to be rich in planar β-sheet domains that can serve as a pattern for orientation of water molecules on its surface into an ice-like structure (Kajava and Lindow, 1993) as illustrated in Figure 13. Shredded *Pseudomonas syringae* membrane is commercially available as Snomax® and it is used in artificial snow production.

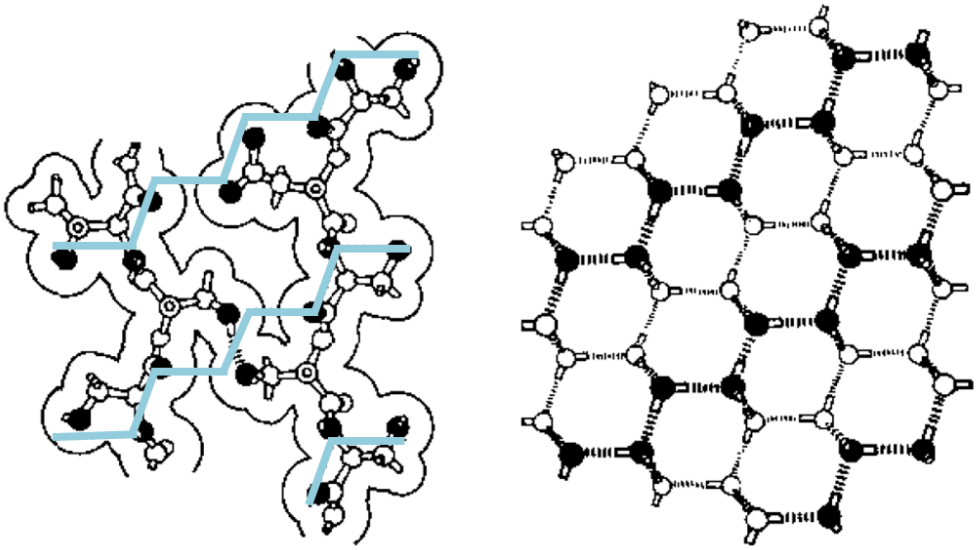

Figure 13: Schematically representation of the ice nucleating protein structure of *Pseudomonas syringae* (left) and ice crystal lattice (right). Similarities between these two ordered structures (zig-zag configuration) are present, whereby the hydrogen bond acceptors and donors of the ice nucleating protein are complementary arranged to those of ice (adapted from: Kajava and Lindow, 1993).

Different plant-derived materials were already shown to be ice nucleating active. Some examples are decayed leaf litter (Schnell and Vali, 1973), *Prunus* trees (Gross *et. al.*, 1988), fruits of *Citrus sinensis* (Constantinidou and Menkissoglu, 1992) and in various kinds of pollen grains (Diehl *et al.*, 2001). Pummer *et al.* (2012) discovered that not only whole pollen grains exhibit ice nucleating activity (INA), but also that ice nucleating macromolecules (INMs) which are easily detached from the grains are responsible for the INA.

According to Brush *et al.* (1994) the mesophyll cells of fresh winter rye leaves (*Secale cereale*) contain INPs, which are active between -5 to -12 °C. Further the response of these intrinsic ice nucleators to changes in growing conditions (decreased temperature and halved day length) was analysed. While the temperature range of the freezing events remained constant, the composition of the intrinsic ice nucleating substances is modified during acclimation to the lower temperatures. In general, they were identified as composite of phospholipids, carbohydrates and proteins, whereby free sulfhydryl groups and disulfide bonds play a key role in the INA of frost-tolerant rye leaves. For the plants that were grown at 20 °C and a long day length (16 h), phospholipids and carbohydrates are the important parts that can act as active sites, while for plants that were grown at 5 °C with varying the day length (8 h), proteins play a key role. These results indicate that winter rye leaves can synthesize distinct ice nucleators as response to decreased temperatures. (Brush *et al.,* 1994)

Kishimoto *et al.* (2014) analysed the INA of cold-hardy blueberry trees (*Vaccinium corymbosum* and *Vaccinium ashei*) that were at least 20 years old, growing in the northeast area around Tokyo. Stem tissue shows the highest ice nucleation behaviour (-1 to -4 °C), followed in the subsequent order by the tissue of flower buds, fruits, and leaves. The intrinsic INPs in the bark were found in the cell walls and/or the extracellular region. In contrast, inside the cells no or little INA was detected. By IR-thermography the freezing process of an intact blueberry plant was observed in October. Freezing was initiated at two different positions at the steam and subsequently propagated along the steam and from there spread into the leaves. It can be assumed that this protecting mechanism is a response of the plant to subzero temperatures. (Kishimoto *et al.*, 2014)

Sea buckthorn is a perennial plant, able to grow in a variety of climate conditions including highland and marine climate, and this plant exhibits INPs in both, leave and berry tissue (Lundheim and Wahlberg, 1998). Lundheim and Wahlberg (1998) did not find significant differences of the nucleation temperatures of sea buckthorn juice, depending on where the fruits were grown. However, different varieties originating from various regions of the world, but grown under the same conditions possess different mean nucleating temperatures in the range from -15.1 °C for *Hippophae rhamnoides* subsp. *fluviatilis* (Swiss wild type) to -6.1 °C for *Hippophae rhamnoides* subsp. *rhamnoides* (Swedish wild type). (Lundheim and Wahlberg, 1998) Sea buckthorn (*Hippophae rhamnoides*) is a frost tolerant plant that can endure exposure in nature down to -40 °C (Lu, 1992). Leaf-extracts from sea buckthorn (*Hippophae rhamnoides*) shrubs also possess INA (freezing temperature: -5.5 °C). Jann *et al.* (1997) reported that the ice nucleator of raw sea buckthorn berry juice is likely a high molecular weight complex, which consists of a protein (subunits with 25 to 27 kDa) and lipid component. According to Jann *et al.* (1997) disulphide bridges and positive surface charges of the active sites seem to be not important for the INA of sea buckthorn berry juice. In contrast, aromatic amino acids appear to be of importance. The INA of the berries is depending on the degree of maturity. From September to October the berries reach their optimum ripening stage, which is indentified by the orange colour. (Jann *et al.*, 1997)

My hypothesis is that decomposition processes degrade different plant materials into smaller pieces and therefore it is likely that these smaller particles are lifted up by airstream into higher altitudes where they can act as a possible source for biological INPs in the atmosphere.

2 Methodology

2.1 Methods

We analysed ice nucleation behaviour of all samples with the Vienna Optical Droplet Crystallization Analyser (VODCA). Characterization of the pure fruit juices was performed by using Attenuated Total Reflectance (ATR) Fourier Transform Infrared (FTIR) and Ultraviolet-Visible (UV-VIS) spectroscopy. Further we made experiments with chaotropic reagents, a protein digesting enzyme, and different solvents.

2.1.1 VODCA

Experimental Setup

We use VODCA for the examination of the INA of different samples. All ice nucleation experiments were done in the immersion freezing mode. In this mode the INPs are immersed in droplets prior freezing. In previous studies of our working group the custom-built experimental setup VODCA has already been used and there a detailed description is given (Pummer *et al.*, 2012; Zolles *et al.*, 2015). The measurements were performed on two different setups, working with the same measurement principle, with which we are able to observe the freezing of droplets in an emulsion. The setups are depicted in Figure 14 and are described in more detail in Table 2. We observe freezing via an incident light microscope equipped with a 20 fold-LWD-objective and an attached camera connected to a computer. As a result of the Mie scattering that describes the elastic scattering of light by spherical particles, which size is comparable to the wavelength of the light, frozen droplets show a different light scattering behaviour than liquid droplets. Therefore freezing events are directly visible. In the light microscope there are two key components responsible for the magnification. The objective works as a collecting lens and magnifies the image in the first step to an intermediate image generated in the optics lens barrel. The ocular is also a collecting lens and works like an optical magnifier and magnifies the intermediate image in the second step considerably once more to real image.

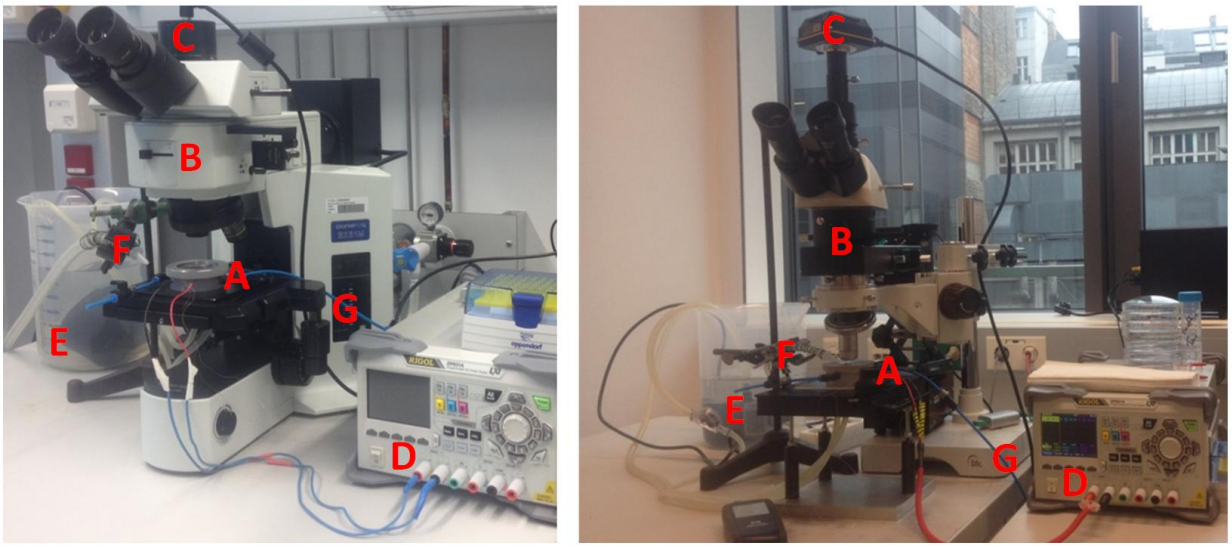

Figure 14: The two used VODCA setups for the freezing experiments: setup 1 (left) and setup 2 (right). The components of each setup are: cryo-cell (depicted closed, A), microscope (B), camera (C), power supply (D), ice-water bath and a pump (E) for cooling, dry air (F), nitrogen supply (G) and a computer, which cannot be seen on the photographs.

Table 2: Specification of the two used VODCA setups to analyse the samples.

	Setup 1	**Setup 2**
Light microscope	Olympus BX51M	custom-made production
Camera	Hengtech MDC320	microQ L3CMOS
Thermoelectric cooler	HighTech Peltier Element Quick-cool QC-31-1.4-3.7M	
Thermocouple	PCE-T312 (type K)	
DC Power Supply	Rigol DP800A	
Software	Based on LabVIEW	
Thermocouple measurement device	NI USB-TC01	
Water pump	EHEIM universal pump	

Cooling was achieved by a thermoelectric cooler, which operates on the principle of the Peltier effect. The thermoelectric cooling device consists of an array of alternating p- and n-doped semiconductor units that are soldered between two ceramic plates in a sandwich-like pattern (see Figure 15), electrically in series and thermally in parallel. One pair of p- and n-doped units is denoted as a couple. At the junction a contact potential is generated by the reason of the two different work functions of the semiconductor materials.

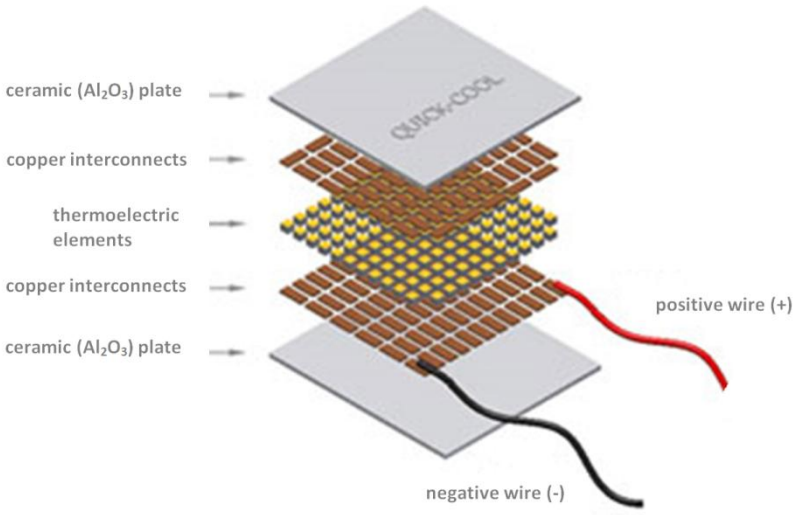

Figure 15: Setup of the used Peltier element with the different layers (source: Quick-Ohm Küpper & Co. GmbH, Unterdahl 24B, 42349 Wuppertal)[10].

Due to the Peltier effect a temperature difference is created and a heat flux from one side (cold side) to the opposite side (hot side) occurs when direct current is applied between the junctions of two different types of semiconductors. The connection between transported heat and electric current is given by Equation 11.

$$P = \frac{\Delta Q}{\Delta t} = (\pi_A - \pi_B)I$$

Equation 11

P	Power at the Peltier effect [W]
Q	Heat [J]
t	Time [s]
π_i	Peltier coefficient of the material i [V]
I	Electric current [A]

The cold plate absorbs the heat from the surrounding atmosphere and the heat is transported to the hot side where it is released afterwards. In the used measuring system the hot side of the Peltier element is fixed on a copper heat exchange device, which was cooled by an ice water blend with a temperature of approx. 5 °C. That aqueous medium was circulated with a water pump to achieve continuous cooling. Thus the heat from the bottom of the Peltier element was dissipated. Our used Peltier element was capable of achieving a

[10] http://www.quick-cool-know-how.com/peltier_elements/peltier-know-how.htm (30.1.2018)

temperature difference of 70 °C and leading to a minimum temperature of approx. -55 °C. The cooling effect is mainly dependent on the applied current and the Peltier element properties, such as the number of couples and the semiconductor materials. For the temperature measurement of the sample a K-type thermocouple[11] was fixed on one corner of the ceramic surface with temperature conductive glue and linked to a computer via a thermocouple measurement device. By a computer-controlled power supply and a program based on LabVIEW the regulation and control of the direct current, and therefore temperature was possible. With our program, we were further able to access the camera, observe the freezing, and recorded videos and photos of the process (see 2.1.1 Data Analysis part below).

The cryo-cell (Figure 16 and Figure 17) was built airtight, using a hollow Teflon® cylinder (diameter 68 mm and height 25 mm) to avoid gas exchange during the experiments. Water vapour from the atmosphere could interfere with the emulsions and influence the measurements. During the freezing experiments the glass window of the cell was streamed with dry air to prevent fogging.

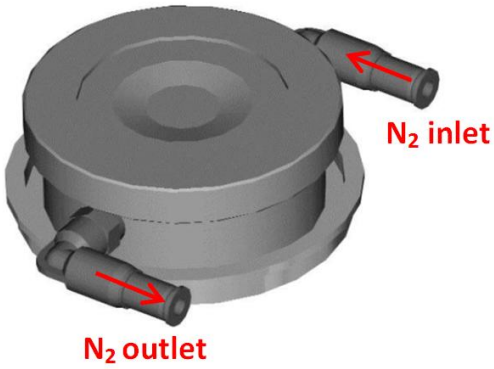

Figure 16: Construction plot of the cryo-cell with nitrogen in- and outlet.

[11] https://www.msm.cam.ac.uk/utc/thermocouple/pages/ThermocouplesOperatingPrinciples.html (10.8.2017)

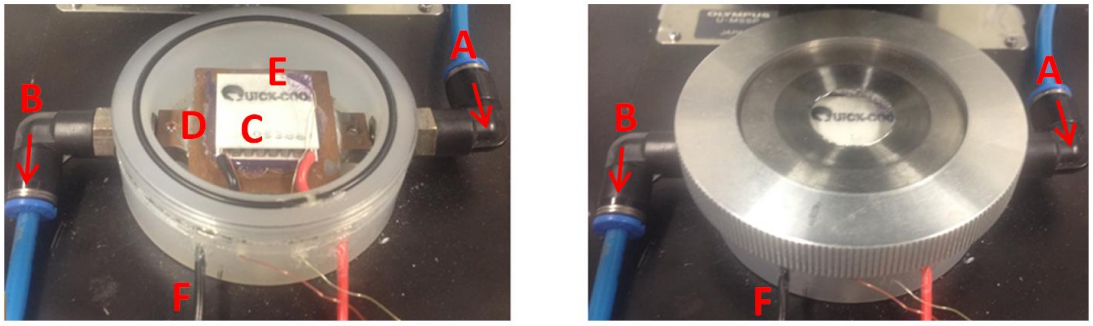

Figure 17: Close up of the cryo-cell: without (left) and with a cover cap (right). Their gas in- (A) and outlets (B) are horizontally arranged. The Peltier element (C) is attached on the copper block (D) with conductive glue (violet colour) and at the upper right corner the thermocouple (E) is fixed with the same adhesive as can be seen in the left photograph. The red and black electronic connections (F) of the thermoelectric cooler are also visible in the photographs.

Production of Emulsions

Prior to the production of the emulsions for the VODCA experiments, the aqueous samples were shaken via a shaking device (VWR, lab dancer S40) until homogeneity. Emulsions consisted of a droplet of an oil matrix (approx. 85 wt% paraffin oil and 15 wt% anhydrous lanolin as an emulsifier) in small excess and a droplet of aqueous sample. Both droplets (each droplet had a volume of approx. 2 µl) are dripped on a cleaned monocrystalline silicium plate. We mixed the two droplets, using a pipette tip (standard, yellow, 200 µl, VWR; made out of plastic material) until the emulsions turned opaque. This change of appearance is a result of the Mie scattering caused by water droplets with diameters in the micrometre size range. With this method we create a good-quality emulsion of small aqueous droplets immersed in an inert oil matrix. The combination of paraffin oil and lanolin affect the emulsion quality (stable droplet size distribution), but does not influence the ice nucleation temperature of the aqueous droplets (Hauptmann *et al.*, 2016). We spread the emulsion on the silicium plate to create a thin sample film with areas where the droplets are present as monolayer. After that, we inserted the plate into the cryo-cell mounted under the microscope (see Figure 14). After we chose a good sampling spot, containing droplets in the defined size range being present in a single layer, we started the experiment.

Experimental Procedure

The closed cell was flushed with nitrogen to remove humidity out of the chamber every time after a new sample was inserted and dry air was used to avoid fogging on the glass window at the outside of the cell. For each sample four measurements were made at different areas of the plate to create a better statistical value.

At the beginning of every measurement day, the ice nucleation of ultrapure MilliQ® water (produced with Millipore® SAS SIMSV0001) was measured, to verify if the setup was working properly. Afterwards we started the experiments with our samples. Between the measurements the monocrystalline silicium plate was cleaned well with redistilled acetone to remove oil residues and in a second cleaning step ultrapure water was used. Before preparing a new sample, the plate was dried in an air stream. For all the here presented measurements, we used the same two silicium plates (15x15x1 mm) pictured in Figure 18.

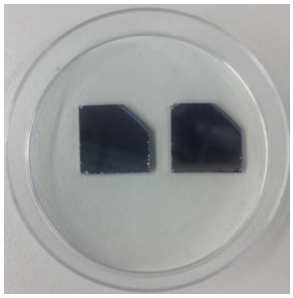

Figure 18: The two monocrystalline silicium plates that were used for all ice nucleation measurements in this thesis.

Data Analysis

With the help of the recorded measurement videos and the VLC media player Version 2.2.2 we carried out the data analysis. Due to changes in the interior scattering behaviour of the measured droplets freezing can be observed. Only droplets with the diameter between 20 µm and 60 µm (corresponding to 4 - 113 pl in volume) were taken into account of the droplet size distribution, since the freezing temperature of the droplets is dependent on its size (subchapter 1.4.1 and 1.4.2) (Hartmann *et al.*, 2016). Figure 19 shows four video snapshots of the freezing process of pure black currant juice at different temperatures.

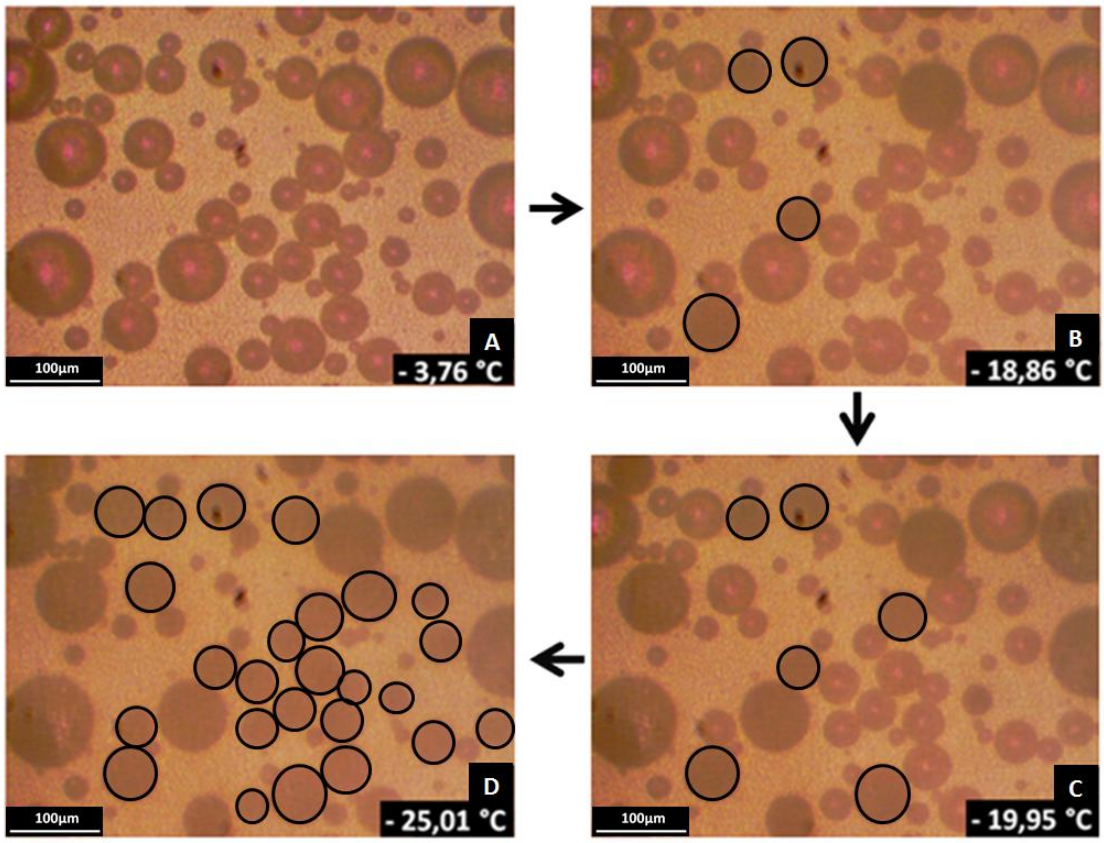

Figure 19: During the freezing of the droplets they change their light scattering properties. Frozen droplets appear darker in the video snapshots. The frozen droplets in the defined size range are highlighted by black circles. In the first snapshot (A) none, in (B) four, in (C) six and in the fourth snapshot (D) 25 of the droplets are frozen. Here, pure black currant juice was measured.

We counted the number of frozen droplets and combined the four measurements done per sample. The percentage of the frozen droplets of a sample (also called frozen droplet fraction (f_{ice})) is plotted against the corresponding temperature, resulting in so called freezing curves. Additionally the heterogeneously frozen droplet fraction ($f_{ice,het}$) was determined. For each sample we evaluated the median freezing temperature T_{50}. This is the temperature, where 50 % of the observed droplets were frozen. We also determined the median freezing temperature of the heterogeneous frozen droplets $T_{50,het}$. For this parameter we only took into account droplets freezing heterogeneously. For the evaluation of the heterogeneous values -35 °C was used as a threshold value for heterogeneous nucleation - every droplet that froze below -35 °C is too close to homogeneous nucleation and is therefore not considered (see Figure 28 in chapter 3).

2.1.2 UV-VIS Spectroscopy

The information of this subchapter is mainly extracted from the following book: Perkampus (1992) and references therein, if not indicated otherwise.

UV-VIS spectroscopy is a technique in molecular spectroscopy. Molecules and atoms can undergo electronic transitions when irradiated with UV-VIS radiation. There are several transitions: n → π*, π → π*, n → σ*, σ → σ*(Lehmann, 2009)[12]. However, in the visible range (400 - 800 nm) the most prominent electronic transition is besides the n → π*-, the π → π*-excitation in conjugated systems (Lehmann, 2009) such as unsaturated hydrocarbons (e.g. polyenes, polyaromatics, polyphenols). The higher energetic ultraviolet light (200 - 400 nm) has the ability to excite electronic transition of non-bonding heteroatom electrons.

The main components of a spectrometer are a light source, a monochromator, a sample and reference holder and a detector. By a prism or grating monochromator the light is dispersed into its constituent wavelengths. The radiation source that is continuous over the specific spectral region is a deuterium lamp for the UV region and a tungsten or tungsten-halogen lamp for the VIS region. Over the whole spectral region these dispersive spectrometers allow the continuous variation of the measurement wavelength. In a double-beam instrument, the primary light beam is split into two beams and directed along two paths which pass through alternately the reference and sample cuvette. The reference beam intensity is taken as 0 % absorbance. In Figure 20 a simplified schematic double-beam UV-VIS spectrometer is displayed.

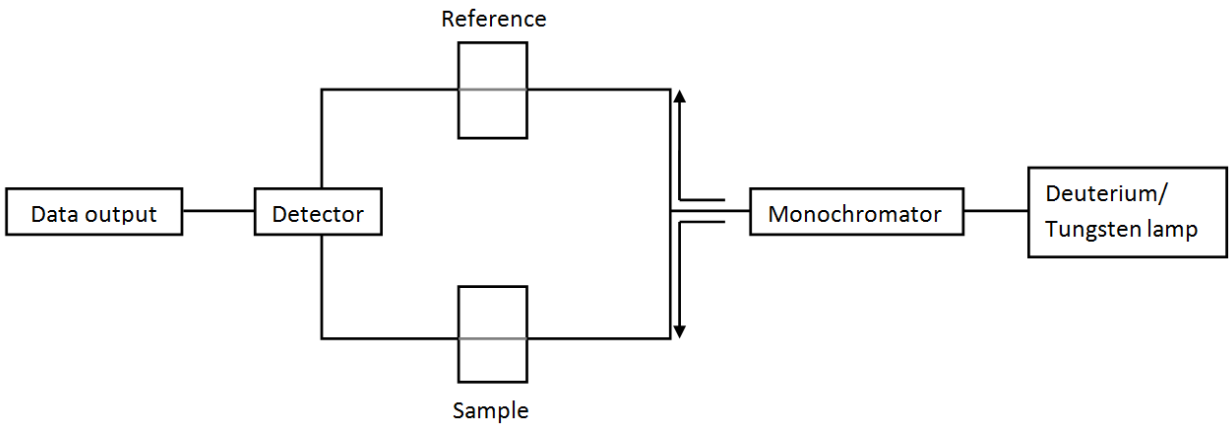

Figure 20: Schematic depiction of the main components of a double beam UV-VIS spectrometer.

[12] available at http://www.bcp.fu-berlin.de/chemie/chemie/studium/ocpraktikum/_Unterlagen_Spektroskopie/uv.pdf (28.2.2018)

In most instruments, the sample and reference beam are measured alternately by means of a beam chopper, a rotating sector aperture for intensity modulation. Thus, light of varying intensity falls onto the detector and the ratio of the two beam intensities is calculated according to the Bouguer-Lambert-Beers law (Equation 12). This law describes the attenuation of light intensity and relates it to the properties of the substance, when transmitting trough. This law is limited to diluted solutions ($c \leq 10^{-2}$ mol$*$l^{-1}), homogeneous distribution of the absorbing components, insignificant multiple scattering and negligible variation of the extinction coefficient within the measured spectral region.

$$A_\lambda = lg\left(\frac{I_0}{I}\right)_\lambda = \varepsilon_\lambda \, c \;\; d$$

Equation 12

A_λ	Absorbance at a certain wavelength λ [-]
I	Intensity of the transmitted light [W$*$m^{-2}]
I_0	Intensity of the incident light [W$*$m^{-2}]
c	Concentration of the light-absorbing substance [mol$*$l^{-1}]
ε_λ	Molar decadic extinction coefficient at a certain wavelength λ [l$*$m$^{-1}*$mol^{-1}]
d	Pathlength of the sample [m]

The measurements were carried out with the UV-VIS-NIR spectrometer (PerkinElmer Lambda 750 in transmission mode and a Photomultiplier (PMT) detector module), which is equipped with a tungsten and a deuterium lamp. The spectrometer is depicted in Figure 21. We worked with the wavelength range of 800 to 200 nm with a data interval of 1 nm. The PMT detector response was set to 0.36 seconds. At 319.2 nm the switching between the tungsten and deuterium lamp occurred. We used the software UV WinLab to follow the measurements and to export the data. For all measurements a quartz cuvette filled with ultrapure water was used as blank. Between the measurements of different sample dilutions the cuvette was cleaned well with ultrapure water and blown out with dry air. This method was used for comparison of the different juices and valuating their extraction behaviour (solvent experiments).

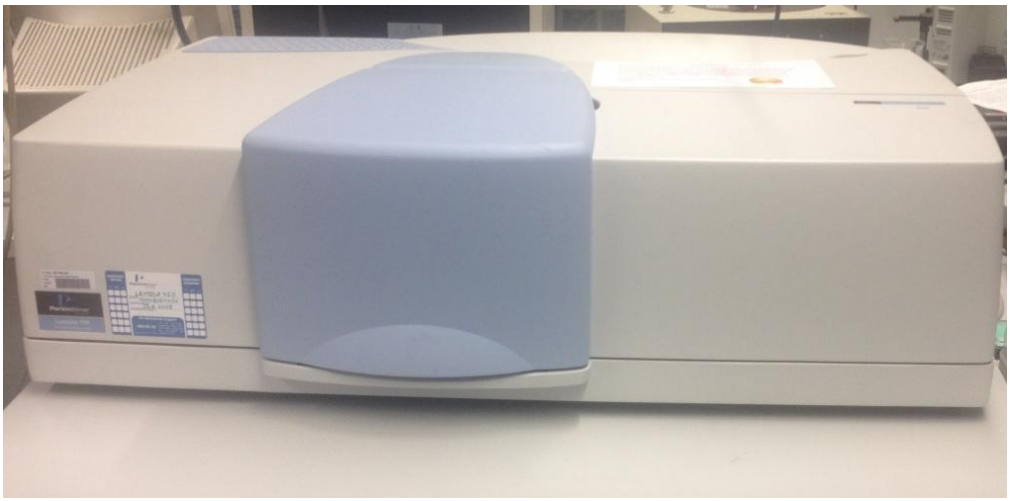

Figure 21: PerkinElmer Lamda 750 UV-VIS-NIR spectrometer and PMT detector module.

2.1.3 ATR-FTIR Spectroscopy

The information of this subchapter is mainly based on the following books: Smith (2011) and Stuart (2004) and references therein, if not indicated otherwise.

In principle, every object has three degrees of freedom in the three-dimensional space. A molecule containing N atoms has 3N degrees of freedom including translation (3), rotation (3) and a number of vibrations. A linear molecule has 3N-5 degrees of vibrational freedom and a non-linear molecule has 3N-6 since no observable energy is related to the rotation around the linear axis. For a single vibration of a bond the harmonic vibrational frequency is given by Equation 13:

$$\nu = \frac{1}{2\pi}\sqrt{\frac{k}{\mu}}$$

Equation 13

- v Frequency of absorption [s^{-1}]
- k Force constant [$kg_{*}s^{-2}$]
- □ Reduced mass [kg]

Besides the masses of the atoms and the stiffness of their bonds the vibrational frequencies are also dependant on their molecular geometry and electronic structure. The mid-IR light from 4000 to 400 wavenumbers can excite fundamental vibrations and overtones of

molecules. The IR spectroscopy may therefore be used to study and identify structures of compounds since the bands in this spectral region are rich in information. Functional groups have characteristic bands in consideration of their frequency and intensity. The selection rule for IR spectroscopy is that the molecule must change its electric dipole moment during the vibration to show IR absorptions. The intensity of the absorption band is related to the square of the change of the electric dipole moment. Therefore the number of the IR active vibrations is related to the symmetry of the molecule observed. Molecules with same symmetry and same number of atoms therefore have similar IR spectra. Of course the exact position of the bands still depends on the reducible masses and the force constants.
In dispersive IR spectrometers a monochromatic light beam would illuminate the sample and the absorbed light is measured. This process would be repeated for each wavelength in the measurement range by applying Equation 13 the spectrum is obtained, which is a plot of wavenumber versus measured light intensity.

Since the 1970s the FTIR spectroscopy is used. Compared to dispersive spectrometers there are three significant advantages of FTIR instruments, which are described hereinafter.

- One of the major benefits is called the *Fellgett* or *multiplex* advantage. It is based on the fact that information from all wavelengths is monitored simultaneously which improves the Signal-to-Noise Ratio (SNR) per scan time. The SNR is proportional to the square root of the number of scans added together to comprise a spectrum, as shown in Equation 14. For the measurements carried out here, 512 scans of the background as well as for each sample were made, so the SNR is nearly twenty-three times higher than a spectrum measured with only one scan, so the spectral quality is improved significantly. The resolution is also directly related to the SNR, whereby higher resolutions cause more noise due to the characteristics of the interferometer. Hence the samples were measured at a resolution of 4 cm^{-1}, which is sufficient for liquids and solids.

$$SNR \propto \sqrt{N}$$

Equation 14

SNR Signal-to-Noise Ratio [-]

N Number of scans added together to comprise a spectrum [-]

- The second advantage is known as *Jacquinot´s* or *throughput* advantage. Due to the fact that in FTIR spectrometer no monochromator or slits are required, a high intensity of IR light from the source impinges on the detector, hence leading to higher signal levels and improved SNRs.
- The third one is the *Connes´* or *wavelength precision* advantage. In contrast to the dispersive technique where the wavelength scale depends on the mechanical movement of diffraction gratings in FTIR instruments a helium-neon laser and a visible polychromatic light source are used to measure the mirror position and therefore the optical path difference of the interferometer. Thus the monochromatic laser and the polychromatic lamp act as internal references and so the wavenumber scale is calibrated, which results in a higher wavenumber precision on the order of ± 0.01 cm^{-1}.

FTIR is based on the principle of the interference of radiation between two beams to yield an interferogram, where the entire spectrum is captured. This interference pattern (time domain) is then converted into an IR spectrum (frequency domain) by a mathematical calculation known as the Fourier transformation[13].

The working principle is described below. A beam of polychromatic light produced by a globar is brought into contact with the sample and then it is detected how much of that beam is absorbed by the sample. In front of the sample an interferometer is placed, which is a configuration of two mirrors, one moveable and one fixed. By a beamsplitter, consisting of a semi-reflecting film, the polychromatic beam is split into two parts, ideally 50 % of the incident radiation is reflected to the fixed mirror while 50 % is transmitted to the moving mirror. The two beams are reflected back from the two mirrors to the beamsplitter where they interfere after recombination. Constructive interference occurs when the optical path difference of these two light beams is a multiple of their wavelength. The position of the mirror is changed during the measurement and the light falling on the detector is measured. A scan is the process of moving the mirror back and forth once. A helium-neon laser is used to measure the exact position of the moving mirror. The received interferogram is a plot of IR intensity versus optical path difference. These raw data signals are then amplified by a filter, which eliminates high-frequency contributions. For the subsequent computer processing the data is required in a digital form, which is achieved by an analog-to-digital

[13] available at http://www.damtp.cam.ac.uk/user/dbs26/1BMethods/FourierT.pdf (30.1.2018)

converter. Through the Fourier transformation the data is converted into an IR absorbance spectrum, which is a plot of IR intensity versus wavenumber. The main components of an FTIR spectrometer are shown schematically in Figure 22. In Table 3 the instrument and measurement parameters are listed.

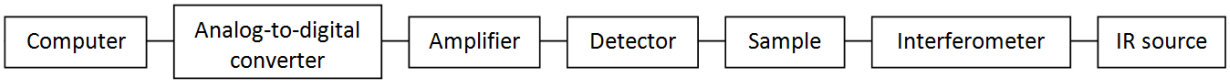

Figure 22: Schematic depiction of the basic components of an FTIR spectrometer.

Table 3: FTIR-instrument and measurement parameters.

	Parameters
FTIR spectrometer	Bruker Vector 22
Detector	DTS (Deuteriated triglycine sulphate)
ATR chamber	PIKE GladiATR^{TM} cell
Mirrors	three
Crystal as total reflection window	germanium
Filter	open
Control program	Opus 5.5
Wavelength scale	690 - 4000 cm^{-1}
Scans	512
Resolution of each measurement	4 cm^{-1}
Intensity	~ 790 counts

Figure 23 shows the used FTIR spectrometer (Bruker Vector 22) with the ATR optic cell (PIKE GladiATR cell) that contained three mirrors and as total reflection window a germanium crystal. During the measurements the cell was flushed continuously with dry air. Due to the ATR device, solid and liquid samples could be measured directly without further treatment. Before the sample measurements were performed, it was essential to run a background spectrum of the clean, dry crystal and the surrounding atmosphere, where typically bands from strong IR absorbing molecules like carbon dioxide and water vapour occur (see Figure 4). At the measurements the IR intensity was around 790 counts. As a control program we used the software OPUS 5.5.

Figure 23: Bruker Vector 22 FTIR spectrometer with a PIKE GladiATR cell.

A schematic depiction of a typical ATR cell is represented in Figure 24. In the used setup the sample of lower refractive index η_s was placed on a germanium-crystal of a high refractive index η_c. An IR-radiation-beam is total reflected in this crystal and when it reaches the boundary layer the light intensity does not instantly go to zero. At this point of total reflection an evanescent wave is formed and with distance from the boundary of the crystal away the energy decreases exponentially. Thus this evanescent wave has a fraction of a wavelength, capable of interacting with the sample. When the crystal is covered with sample, which absorbs a part of the radiation, the total reflected beam loses the absorbed energy. The attenuated beam is then focused onto the detector.

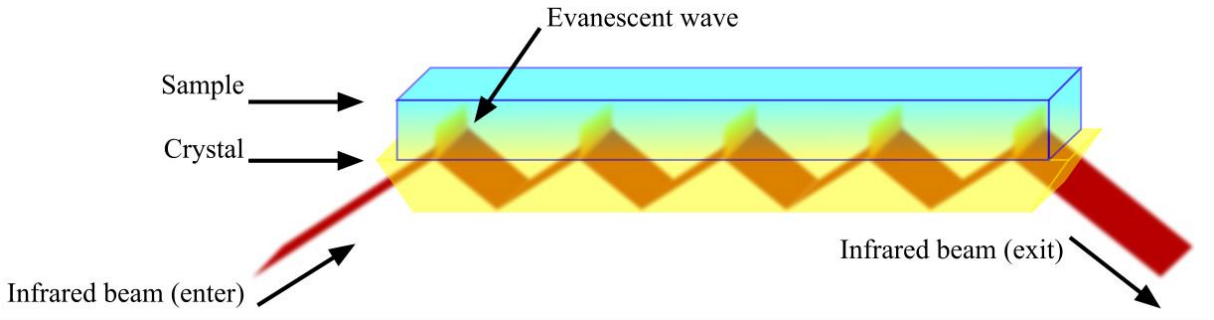

Figure 24: Schematic representation of the ATR-principle. An IR-beam undergoes multiple internal reflections in the crystal and thereby an evanescent wave is formed. This wave sticks up above the crystal surface and might interact with the sample, which is in close contact with the crystal. (source: wikipedia.org)[14].

2.1.4 Dry Mass Content Determination

Due to the fact that the concentration of the INPs of the selected fruit juice samples was unknown, the dry mass content of them was investigated in a pure and filtered form. 500 µl of each homogeneous fruit juice was pipetted with a 1000 µl-Eppendorf-pipette into a sterile Petri dish (diameter 55 mm manufactured from virgin crystal grade polystyrene), which was weighed before with an analytical lab balance scale (Sartorius AW-224) and then dried under vacuum in a desiccator over blue silica gel until their weight remains constant. For every juice sample two dry mass content determinations were carried out. The results are obtained by calculating the mean value and the standard deviation based on a sample.

[14]By Fulvio314 - Own work, CC BY-SA 3.0, https://commons.wikimedia.org/w/index.php?curid=28499710 (30.1.2018)

2.2 Sample Selection and Description

2.2.1 Sample Selection

From previous publications (Jann *et al.*, 1997; Lundheim and Wahlberg, 1998; Kishimoto *et al.*, 2014) and from research of our working group (Bichler, 2015) it is known that several berry fruit juices show INA. Bichler (2015) examined a number of fruit juices from berries and found out that most of them exhibit INA.

Based on this research and in terms of their geographical origin, five fruit juices were selected: acerola, black currant, chokeberry, elderberry and sea buckthorn. Except for acerola, which occurs primary in tropical and subtropical climate zone (see Figure 12 in subchapter 1.6; subchapter 2.2.2), the other four plants can be distributed up to the boreal region (Figure 25). We wanted to investigate among other parameters (size of the INPs, solubility of INPs in different solvents, and behaviour with chaotropic agents and a protease), if there are differences in INA of the fruit juices according to the climate zone of origin.

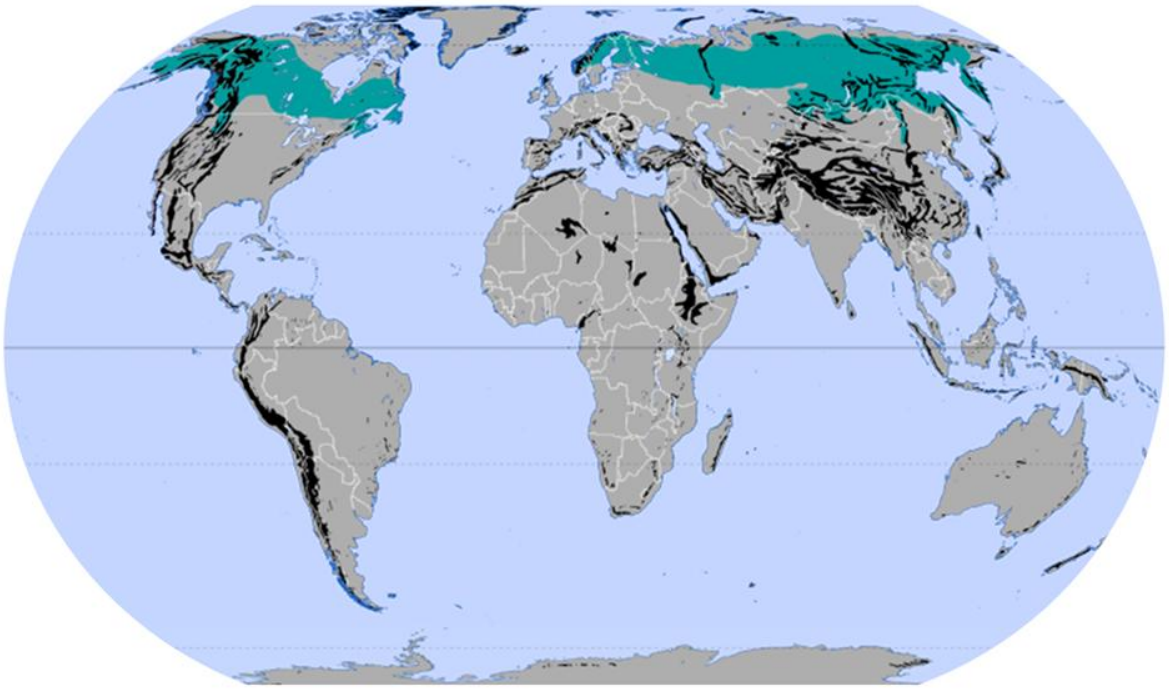

Figure 25: Boreal zone (marked in aquamarine) according to Jürgen Schultz (adapted from wikipedia[15]).

[15] Von Ökologix - Eigenes Werk, CC BY-SA 3.0, https://commons.wikimedia.org/w/index.php?curid=23607877 (12.2.2018)

Fruit juice samples were commercially available juices and all of them were of organic quality. The pure juices were bought from *Alnavit*[16] (elderberry) and *dm Bio*[17] (acerola, black currant, chokeberry and sea buckthorn). These five berry juices were marked as "Muttersaft". "Muttersaft" from *dm Bio* is directly pressed berry juice and processing was done as little as possible including mild pasteurization at temperatures as low as possible for a short amount of time to preserve most of the natural ingredients. The heat treatment is done to prevent microbial spoilage.

For the elderberry juice from *Alnavit* we were not able to receive further information concerning processing, heat treatment and origin of the berries. Since elderberries contain the plant toxin Sambunigrin, which is a cyanogenic glycoside, the ripe berries must be heated up to at least 80 °C in order to break the toxin down[18].

All four *dm Bio* juices were harvested at perfect degree of ripeness and then pressed immediately or were stored in the frozen state and then pressed on demand. The originating country of the acerola berries was Brazil. Black currant was grown in Germany and Poland, chokeberries in Ukraine and Poland, and sea buckthorn in Germany, Poland and Romania. All of the examined juices were naturally cloudy and are listed in Table 4.

Table 4: A list of all examined fruit juices. Given is the common name and the sample name, brand, genus, volume of the bought unit and the charge number.

Common name	Sample name	Brand	Genus	Volume	Charge Number
Acerola	A	dm Bio	*Malpighia*	0,33 l	61812
Black currant	B	dm Bio	*Ribes*	0,33 l	61493
Chokeberry	C	dm Bio	*Aronia*	0,33 l	62152
Elderberry	E	Alnavit	*Sambuccus*	0,33 l	57188
Sea buckthorn	S	dm Bio	*Hippophae*	0,33 l	60857

[16] Alnavit GmbH (Bickenbach, DE)

[17] dm-drogerie markt GmbH + Co. KG (Karlsruhe, DE)

[18] https://www.gesundheit.gv.at/leben/ernaehrung/saisonkalender/oktober/holunder (23.1.2018)

2.2.2 Sample Description

This subchapter comprises the description of the juices, including the origin and distribution of the plants, of which the juices are made of.

Acerola

Acerola cherry fruits are bright red drupes, which occur in pairs or groups of three. They grow on an evergreen shrub or small tree that is in general two to three metres tall, rarely it reaches 6 meters in height. The geographical area of origin of Acerola plants is West Indies, Central and South America, but it can be also found in other tropical and subtropical regions of the world (Phillips, 2005)[19]. This plant is a member of the Malpighiaceae family. The *dm Bio* acerola juice has a creamy yellow colour.

Black currant

Black currant berries are produced in racemes, containing ten to twenty small dark purple berries. They grow on medium woody shrubs, reaching heights up to 1.5 metres and they belong to the Grossulariaceae family. The main distribution area extends over the temperate climate zone of the northern hemisphere (Friedrich *et. al.*, 1986, p. 846). The black currant juice from the brand *dm Bio* has a dark purple colour.

Chokeberry (Aronia)

Chokeberries are purple or black berries that are formed in corymbs of 10 - 25 small pomes together. They have their origin in eastern North America (National Resources Conservation Service, 2008)[20] and grow on deciduous shrubs, which are generally one to two metres tall. This plant is a member of the Rosaceae family. The colour of the *dm Bio* chokeberry juice is dark purple.

[19] available at http://ufdcimages.uflib.ufl.edu/IR/00/00/28/97/00001/MG04100.pdf (1.2.2018)

[20] "´McKenzie´ black chokeberry" available at https://www.nrcs.usda.gov/Internet/FSE_PLANTMATERIALS/publications/ndpmcrb7936.pdf (1.2.2018)

Elderberry

Elderberries are clusters of small blue-black berries growing on large deciduous, herbaceous perennial shrubs or small trees. The plants usually reach heights of three to eight metres, but sometimes small trees can grow up to 15 metres. It grows primarily in Asia Minor, Caucasus and Europe in alpine valleys up to 1200 m. (Kremer, 2010, p. 86)

It is a member of the Adoxaceae family. The elderberry juice from *Alnavit* has a dark purple colour.

Sea buckthorn

Sea buckthorn berries are orange-red to yellow oval berries growing on deciduous shrubs that are reaching sizes from half a metre to six metres, occasionally up to 10 metres. This plant belongs to the Elaeagnaceae family and it can be found in Europe, Balkans, Caucasus and western Asia (Kremer, 2010, p. 20). The *dm Bio* sea buckthorn juice has an intense yellowish-orange colour.

2.3 Sample Preparation

Every preparation, dilution and cleaning step was done by using ultrapure water with a value of resistance of 18.2 MΩ∗cm at 25 °C.

2.3.1 Fruit Juices

After opening of the fruit juice bottles they were divided into aliquots of approx. 40 ml and stored at -20 °C in centrifuge tubes (sterile, 50 ml, BRAND, made out of polypropylene) until further use.

Pure Juices

Samples marked as pure juices did not undergo any additional treatment.

Filtered Juices

To receive the filtered fruit juice samples the following procedure was done: Each of the five different pure juices was transferred into culture tubes (sterile, natural, 14 ml, VWR collection, made out of polypropylene) and centrifuged for one hour at 3500 rpm (1972 g) at room temperature with a centrifuge (Sartorius Sigma 2-16P). Only sea buckthorn had

additional suspended particles above the supernatant over the deposited solid particles, which is illustrated in Figure 26.

Figure 26: Sea buckthorn juice after treatment with a centrifuge for one hour at 3500 rpm (1972 g) at room temperature. Solid particles are divided in one top and one bottom fraction. Furthermore the liquid still shows visible cloudiness.

Then the liquids of the juices were separated from the solids using a glass Pasteur pipette. The remaining liquid of the acerola and sea buckthorn juices were then centrifuged a second time for one hour at 4000 rpm (2575 g) at room temperature to remove the remaining solid particles in the liquid. Of all five juices the supernatant was separated again and afterwards filtered with a sterile syringe filter (< 0.45 µm, VWR) consisting of cellulose acetate.

Sedimented Juices

Sedimented means that the juice was centrifuged for one hour at 3500 rpm (1972 g) at room temperature and the supernatant was measured after the separation from the solid particles by using a glass Pasteur pipette. No further filtration steps were applied.

2.3.2 Solvent Experiments with Methanol, Methylene Chloride, and Cyclohexane

From each homogeneous, pure fruit juice 500 µl were dried in a Petri dish (Steriplan, diameter 50 or 58 mm, made out of glass) under vacuum in a desiccator over blue silica gel. For each fruit juice species three dishes had to be prepared - for every solvent (methanol, methylene chloride, cyclohexane) one separate dish. Afterwards 500 µl of solvent were pipetted onto the dried residue of the fruit juice. With circular motion of the solvent it was tried to dissolve the fruit juices. The solvent with the dissolved molecules of the fruit juice was transferred into a new glass Petri dish and dried under the same conditions as the fruit juices. In the next step the resulting residue was weighed, then dissolved in 500 µl ultrapure water and afterwards transferred into a safe lock tube (Eppendorf, 2 ml, naturel, made out of polypropylene).

2.3.3 Experiments with Chaotropic Agents and a Protease

We carried out the following experiments with guanidinium chloride (GdmCl), urea, and the protease Subtilisin at different temperatures to examine the role of proteinaceous substances in the INA of pure black currant and sea buckthorn juice. We selected these two juices, because the experiments in this thesis (the results are presented in subchapter 3.1.1) showed that sea buckthorn has the highest $T_{50,het}$ value and according to the samples used in Bichler (2015) black currant (*Alnavit*) has the highest concentration of INPs of her selected fruit juices.

Depending on its environment a protein folds into higher ordered structures, also known as its native confirmation. These specific three-dimensional shapes are stabilized by weak non-covalent bonds such as hydrogen bonds. In general the integrity of the native confirmation of a protein is required for its specific functional activity.
Chaotropic agents such as GdmCl and urea can disrupt the ordered hydrogen bonding network of the water structure and its environment, this may influences the stability of the native state of a protein in an aqueous solution. This process is termed as denaturation and it usually results in complete protein inactivation. Chaotropic solutes can induce unfolding via different pathways reflected by variation of the structure of the solvent around the protein, even though the mechanism of action of these agents is not completely understood.

Camilloni *et al.* (2008) performed simulations with the protein L indicating that the α-helix is destabilized first in aqueous solution with GdmCl. This solution generates a much higher average dipole moment - due to Gdm^+ and Cl^- ions - than generated by water alone. The Coulomb interaction induced by GdmCl has a longer-range electrostatic effect and can lead to denaturation of the protein, because the helical region is rich in residues that are charged at neutral pH. The unfolding process takes place due to stretching of the α-helix. The β-sheet structure is remarkably stable, this could be explained by the fact that the fraction of charged residues is lower in this secondary structure. In contrast, in the simulations in aqueous urea of the protein L, unfolding starts by destabilization of the β-sheet structure caused by urea accumulation in the first solvation shell replacing some water molecules. As a consequence the total number of hydrogen bonds between the protein and the solvent are reduced. This property of urea linked with the variations of solvent structure leads to the denaturation of the protein. Subsequent to the β-sheet disruption, the α-helix also gets unfolded. In conclusion, one substantial difference between urea and GdmCl is that urea accumulates and therefore disrupts the first solvation shell of a protein, while GdmCl does not particularly interfere with the solvation shell around the protein. More details about the different unfolding mechanisms of GdmCl and urea can be found in Camilloni *et al.* (2008). (Camilloni *et al.*, 2008)

A protease is any protein-digesting enzyme that cleaves peptide bonds by hydrolysis. Subtilisin belongs to the group of serine proteases and is a non-specific protease.

Experiments with GdmCl at Room Temperature

For the preparation of the 5 molar (M) GdmCl solution 23.882 g of GdmCl were weighed in and diluted up to with 50 ml ultrapure water and then homogenized by a shaking device until it was dissolved completely.

In Table 5 the sample components and sample names are summarized. 500 µl of the homogeneous, pure fruit juices of sea buckthorn and black currant were dried in a sterile Petri dish (VWR, diameter 55 mm manufactured from virgin crystal grade polystyrene) under vacuum in a desiccator over blue silica gel. For each fruit juice species two dishes had to be

prepared – one for the blank (fruit juice and ultrapure water) and one for the investigation with the chaotropic agent (fruit juice and 5 M GdmCl solution). The dried fruit juice residue was dissolved either with 500 µl ultrapure water or with the 5 M GdmCl solution and then transferred into safe lock tubes (Eppendorf, 2 ml, naturel, made out of polypropylene) immediately before the measurement series was started.

As comparison standard Snomax®, which consists of shredded membrane fragments of the bacterium *Pseudomonas syringae* was used. *Pseudomonas syringae* is an ice nucleation active bacterium with special membrane proteins acting as active sites (Lindow *et al.*, 1989). Two Snomax® samples were prepared - one with ultrapure water and one with 5 M GdmCl solution. We used Snomax® in a concentration of approx. 88 mg/500 µl to match black currant, the juice with the higher dry mass, leading to a comparable dilution of GdmCl for all samples. The suspension process was a challenge because of the high concentration of Snomax®. In addition, a blank sample consisted of 86.4 mg ultrapure water and 500 µl 5 M GdmCl was prepared.

Table 5: Overview of the different samples of the GdmCl measurement series and their different compositions:

Sample name	Ultrapure water (upw)	5 M GdmCl [µl]	Black currant (B) dried residue of 500 µl juice	Sea buckthorn (S) dried residue of 500 µl juice	Snomax® (SM) [mg]
B_upw	500 µl		x		
B_GdmCl		500	x		
S_upw	500 µl			x	
S_GdmCl		500		x	
GdmCl_upw	86.4 mg	500			
SM_upw	500 µl				88.2
SM_GdmCl		500			88.0

The sealed and mixed tubes were placed at room temperature (23±1 °C) for 24 hours and two samples were drawn after 19.3 and 24 hours. 2 µl of the well shaken sample were taken and diluted with 18 µl ultrapure water (dilution 1:10) to decrease the salt concentration and stop the effects of GdmCl, subsequently they were homogenized and then stored at -20 °C until the measurement of the INA.

Experiments with Urea and Subtilisin at 60 °C

For the preparation of the 8 M urea solution 24.0 g of urea were weighed in and diluted up to 50 ml with ultrapure water and then mixed well by a shaking device until a clear solution was obtained.

Tris(hydroxymethyl)aminomethane (Tris) acts as a buffer (effective pH range between 7.5 and 9.0) for the protease Subtilisin, which was obtained from the bacterium *Bacillus licheniformis*. The Tris buffer is important for the physiological effects of this enzyme. A 0.1 M Tris solution was required, therefore 1214.5 mg of Tris were weight in and diluted up to 100 ml with ultrapure water and adjusted to a pH of 8.0 using 2 normal hydrochloric acid (HCl). The concentration of Subtilisin in Tris buffer was 2 mg/ml. 5 ml of this enzyme-buffer solution were prepared containing all in all 10 mg Subtilisin.

The sample names and exact components of the samples are listed in Table 6. In the same manner as for the GdmCl experiments (described in 2.3.3 Experiments with GdmCl at Room Temperature) three dishes of pure sea buckthorn and black currant juice were prepared. Because of the poor solubility of the Snomax® samples in the GdmCl measurement series, this series was carried out with a lower concentration (approx. 1 mg/ml). The dried pure fruit juice residue or Snomax® was dissolved either with 1 ml ultrapure water or with 8 M urea solution and then placed into safe lock tubes, directly before the measurement series was initiated. Two blanks were also produced just consisting of the different solutions without sample load. Depending on the sample either 100 µl Tris buffer or 100 µl Subtilisin in Tris buffer were added and mixed well via a shaking device.

Table 6: Overview of the different samples of the urea and Subtilisin measurement series and their different compositions:

Sample name	Ultra-pure water (upw) [ml]	8 M urea (U) [ml]	Black currant (B) dried residue of 500 µl juice	Sea buck-thorn (S) dried residue of 500 µl juice	Sno-max® (SM) [mg]	0.1 M Tris Buffer [µl]	2 mg Subtilisin (St) in 1 ml Tris Buffer [µl]
B_upw_Tris	1		x			100	
B_upw_Tris_St	1		x				100
B_U_Tris		1	x			100	
S_upw_Tris	1			x		100	
S_upw_Tris_St	1			x			100
S_U_Tris		1		x		100	
upw_Tris	1					100	
U_Tris		1				100	
SM_upw_Tris	1				1.1	100	
SM_upw_Tris_St	1				1.1		100
SM_U_Tris		1			1.0	100	

The sealed tubes were placed in a lockable box. This box was then placed in a closable heating and shaking device (Gesellschaft für Labortechnik (GFL) 1086) filled with water that was tempered at 60 °C (the temperature range of the experiment was 58-61 °C) and the shaking frequency was 9 min^{-1}. In Figure 27 the used device is illustrated. The measurement was performed for 24 hours and two samples were drawn after 0 and 24 hours. The first samples were drawn after the tubes were homogenized ("zero samples"), right before the box was transferred into the closable heating and shaking device.

5 µl of the homogeneous sample were taken and diluted with 45 µl ultrapure water (dilution 1:10) to decrease the salt concentration and stop the effects of urea, afterwards they were homogenized and then stored at -20 °C until the measurement of the INA.

Additionally renaturation experiments of the sample that was drawn after 24 hours, were performed. For that purpose, 40 µl of the diluted sample were left for 24 hours at room temperature (23±1 °C).

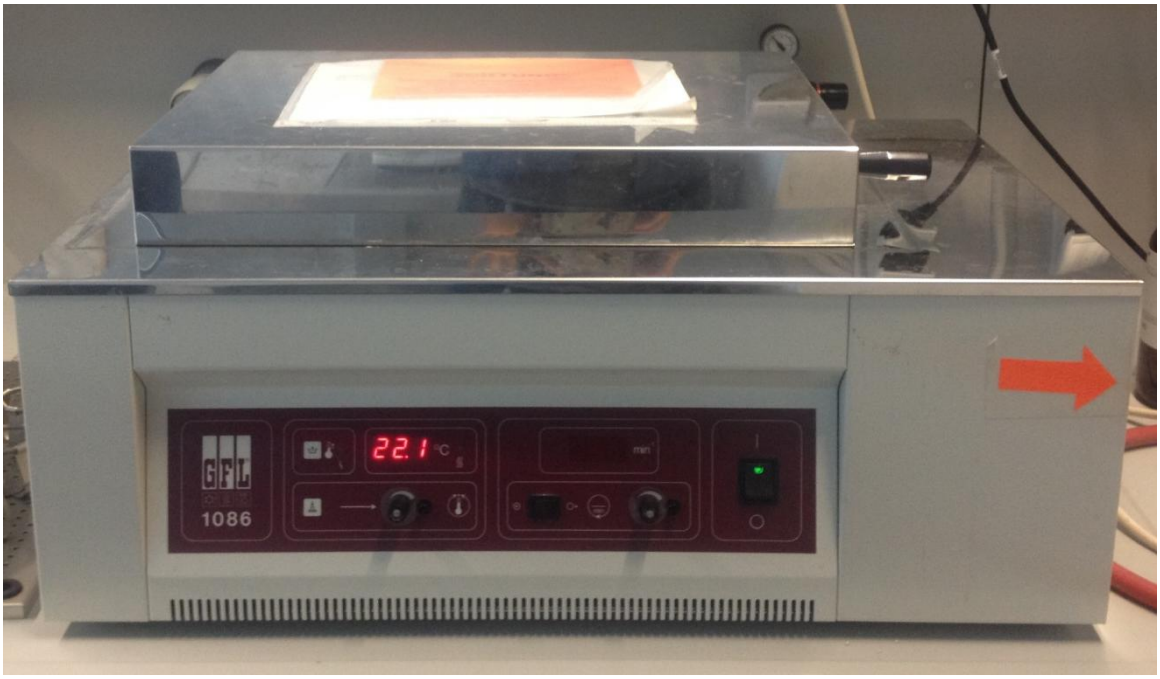

Figure 27: GFL 1086 heating and shaking device.

2.3.4 UV-VIS Measurements

Pure or Sedimented and Filtered Juices

Black currant, chokeberry and elderberry juice could be measured in the pure form without any difficulties. The pure acerola and sea buckthorn juices have a high amount of insoluble solid particles, which would lead to a falsification of the UV-VIS measurement by the scattering of the light on these particles, so for these two samples the sedimented, particle-free juices were used.

5 µl of the pure or sedimented and also for the filtered juices were diluted with 2995 µl ultrapure water up to 3 ml (dilution 1:600) and measured afterwards.

Solvent Experiments

20 µl of the dried methanol dissolved residue, which was dissolved in 500 µl ultrapure water, were diluted with 2980 µl ultrapure water up to 3 ml (dilution 1:150).

200 µl of the dried methylene chloride dissolved residue, which was dissolved in 500 µl ultrapure water, were diluted with 1300 µl ultrapure water up to 1.5 ml (dilution 2:15).

100 µl of the dried cyclohexane dissolved residue, which was dissolved in 500 µl ultrapure water, were diluted with 1400 µl ultrapure water up to 1.5 ml (dilution 1:15).

These prepared aqueous solutions were measured afterwards.

2.3.5 ATR-FTIR Measurements

At first ambient air was measured to determine the background IR absorption. Then one droplet of the homogeneous, pure juice was placed onto the germanium-crystal of the ATR-cell. By the use of a hair dryer (Rowenta Mod. CV5012) at the middle heat position the droplet was dried carefully (not exceeding 35 °C). After sample application we had to wait several hours prior measurement until the equilibrium of gaseous water in the equipment was reached. It was necessary to find a balance between drying of the juices i.e. the remaining humidity and exposure time to air, whereby the possibility increases that oxidation processes take place.

3 Results

The main objective of my thesis was to examine pure and filtered fruit juices concerning their INA and chemical composition.

Investigations were carried out to estimate the size of the contained INPs, as well as the influence of different reagents (three different solvents, chaotropic agents, and a protease) on the freezing properties of the pure juices. The aim was to gather more information about the ice nucleation active species of the investigated juices. To achieve qualitative information in terms of differences and similarities between the five different fruit juices, they were investigated via UV-VIS (description see subchapter 2.1.2) and ATR-FTIR (description see subchapter 2.1.3) spectroscopy. In addition to pure, sedimented, and filtered fruit juices (subchapter 2.3.1), aqueous sample solutions were prepared according to subchapters 2.3.2, 2.3.3 and 2.3.4.

Furthermore the dry mass content of the pure and filtered fruit juices was investigated (subchapter 2.1.4) to find out if there exists a correlation between dry mass content and INP quantity of the five fruit juices.

We generated freezing curves (frozen droplet fraction for the corresponding temperature) with the data that we obtained from the VODCA measurements. To obtain the curves, the frozen droplet fraction (f_{ice}) for each temperature was determined and plotted against the corresponding temperature.

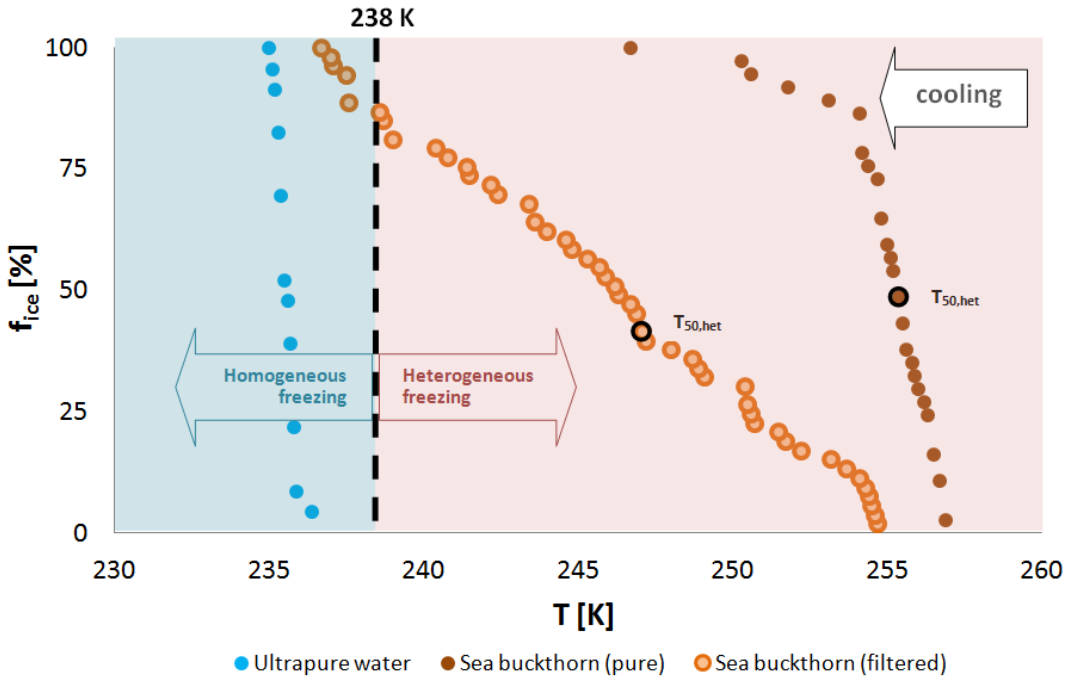

Figure 28: Freezing curves of ultrapure water, pure and filtered sea buckthorn juice. 238 K (corresponds to -35 °C) is used as a threshold value separating homogeneous (blue background) and heterogeneous freezing (red background). In our setup, homogeneous freezing occurs at temperatures below and heterogeneous freezing takes place above 238 K. For each freezing curve the frozen droplet fractions (f_{ice}, $f_{ice,het}$) and $T_{50,het}$ was determined.

Figure 28 provides an example of three different freezing curves: ultrapure water, as well as pure and filtered sea buckthorn juice. Freezing curves are obtained, when the f_{ice}-values (as y-axis) are plotted against their corresponding temperature (as x-axis). The correct way to read a freezing curve is in cooling direction (marked with an arrow in Figure 28). The first frozen droplets are the dots on the lower right corner of the diagram. The fraction of the frozen droplets increases to a maximum of 100 % (all of the counted droplets are frozen). Freezing curves are often characteristic for certain INPs, however, due to the high number of different INPs they are not always easy to compare. For the better comparability of the samples, freezing curves can be reduced to $T_{50,het}$ values. This value describes the temperature at which 50 % of the droplets were frozen heterogeneously (see also subchapter 2.1.1 (Data Analysis)). This $T_{50,het}$ value is used as an expression for the INA of a sample. For the heterogeneous parameters 238 K (corresponds to -35 °C) was used as a threshold value and only the droplets that froze above this value were used for the calculation, whereby the statistical quality is determined by the number of heterogeneously frozen droplets.

3.1 $T_{50,het}$ Values and/or Freezing Curves

3.1.1 Pure and Filtered Juices

The INA of the pure and filtered juices (filtration procedure according subchapter 2.3.1 (Filtered Juices)) was examined. Results of the ice nucleation measurements of all five juices (pure and filtered), as well as of ultrapure water as a blank are depicted in Figure 29. The related $T_{50,het}$ and $f_{ice,het}$ values can be found in Table 7.

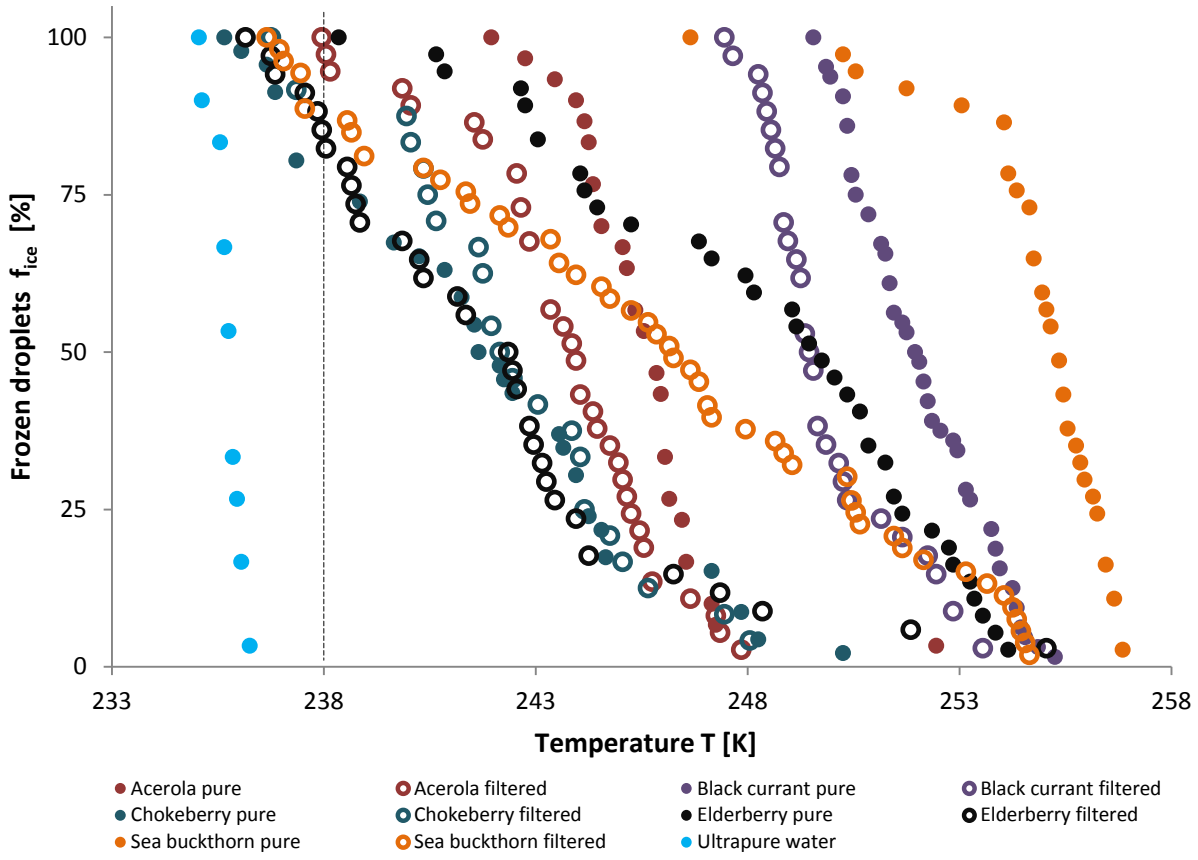

Figure 29: Freezing curves of the five selected fruit juices pure (filled circles), and filtered (empty circles), and of the ultrapure water blank.

Table 7: $T_{50,het}$ and $f_{ice,het}$ values of the five fruit juices. The temperature values have all an error interval of ±1 K, which represents the measuring inaccuracy of the VODCA setup.

Samples		$T_{50,het}$ [°C]	$T_{50,het}$ [K]	$f_{ice,het}$ [%]
Acerola	pure	-27.5	245.7	100
	filtered	-29.2	244.0	92
Black currant	pure	-21.2	252.0	100
	filtered	-23.7	249.5	100
Chokeberry	pure	-29.6	243.6	74
	filtered	-30.5	242.7	88
Elderberry	pure	-23.6	249.6	100
	filtered	-30.4	242.8	79
Sea buckthorn	pure	-17.9	255.3	100
	filtered	-26.3	246.9	87

All analysed juices are ice nucleation active and remain active even after filtration with a 0.45 µm syringe filter. The juice with the highest INA is pure sea buckthorn, followed by pure black currant juice, pure elderberry juice, and pure acerola juice. Chokeberry - pure as well as filtered - is the juice that has the lowest INA of the selected juices.

With the only exception of pure chokeberry juice, all other pure fruit juices show completely heterogeneous ice nucleation behaviour, which corresponds to higher concentrations of contained INPs. Figure 29 and Table 8 show that for the five selected fruit juices a loss of INA took place due to the filtration procedure. For the filtered juices only black currant freezes purely heterogeneous (Table 7). Nearly all other filtered samples show a reduced $f_{ice,het}$ compared to the pure juices. For black currant we see a loss of INA expressed as $T_{50,het}$ value, but the filtered juice still shows an $f_{ice,het}$ value of 100 %. The level of decrease in freezing temperatures ($\Delta T_{50,het}$) due to filtration varies to a large extent, with the least decrease for chokeberry (0.9 K) and the highest for sea buckthorn (8.5 K). The curves with the steepest slope belong to pure black currant and pure sea buckthorn juice. All other juices show a flatter slope and a more stepwise progression. This is a typical shape of a freezing curve when the INP concentration is reduced to a lower level.

We were able to show, that all five fruit juices exhibit INA even if filtered with a cut-off of 0.45 µm. We conclude from this that all selected juices exhibit INPs in the submicron size range.

Dry Mass of the Pure and Filtered Juices

The determination of the dry mass of the selected juices was carried out to investigate if there is a correlation between the dry mass and the INP quantity of the fruit juices.

In Figure 30 and Table 8 the results of the dry mass determination of the pure and filtered juices are presented.

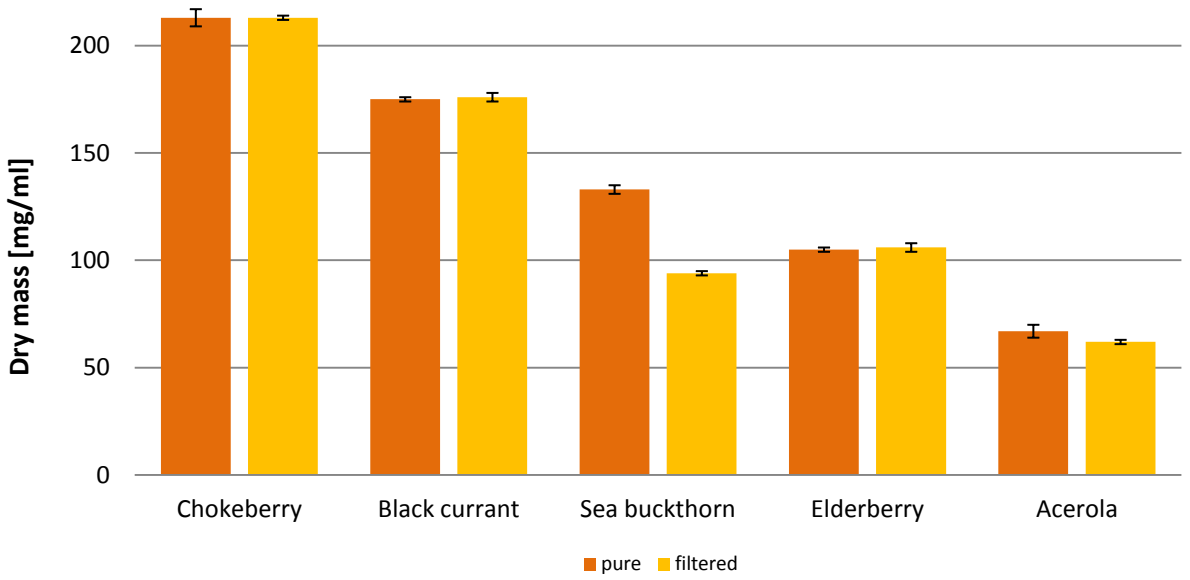

Figure 30: Dry mass of the five selected fruit juices (pure and filtered) - the whiskers mark the standard deviation of the determination.

Table 8: Numerical mean values of the dry mass of the five different fruit juices (pure and filtered), they are indicated with the standard deviation:

Samples		Dry mass [mg/ml]
Acerola	pure	67 ± 3
	filtered	62 ± 1
Black currant	pure	175 ± 1
	filtered	176 ± 2
Chokeberry	pure	213 ± 4
	filtered	213 ± 1
Elderberry	pure	105 ± 1
	filtered	106 ± 2
Sea buckthorn	pure	133 ± 2
	filtered	94 ± 1

The five examined fruit juices represent a wide variation in dry mass. Chokeberry has the highest and acerola has the lowest dry mass. Except for sea buckthorn juice, the filtration

process did not lead to a significant loss in dry mass. Chokeberry, black currant and elderberry juice did not lose dry mass due to filtration.

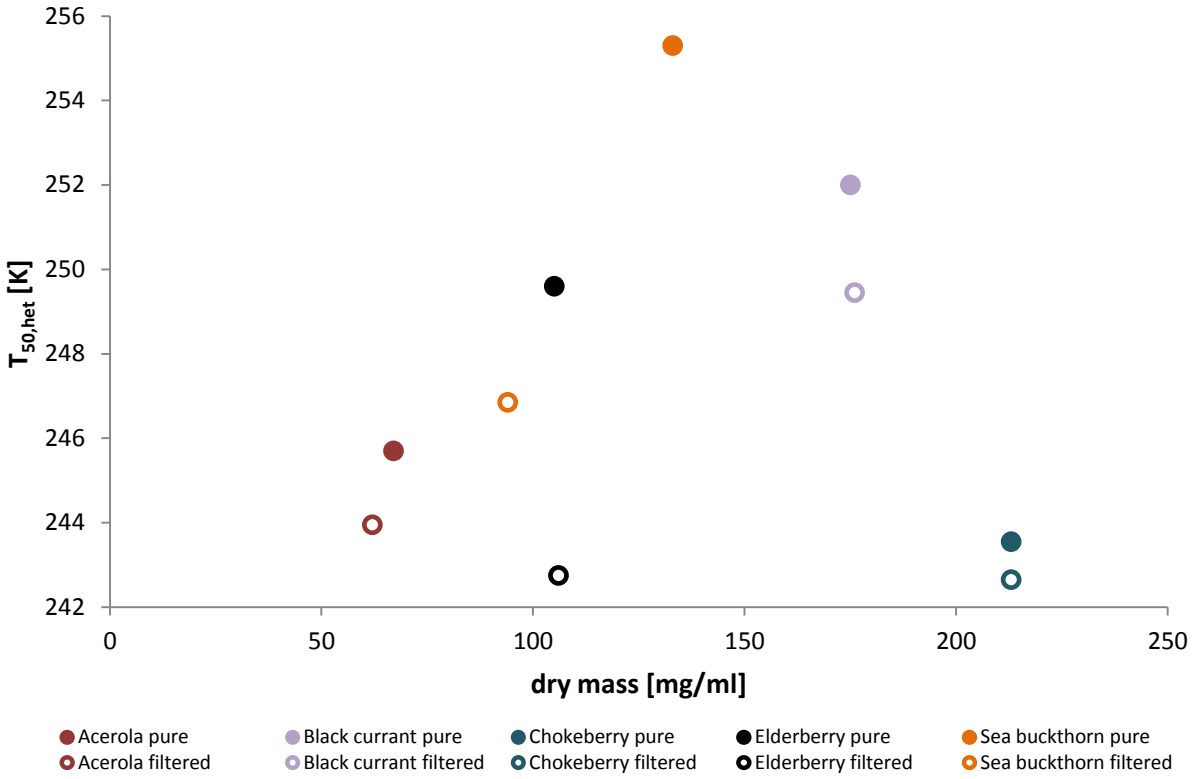

Figure 31: The INA expressed as $T_{50,het}$ values plotted against the dry mass of the pure (filled circles) and the filtered (empty circles) fruit juices.

The INA expressed as $T_{50,het}$ values are plotted against the dry mass for the pure and filtered juices in Figure 31, for a better comparability of these two fruit juice characteristics. The impact of the filtration process on the INA varies widely: for acerola, black currant and chokeberry a trend, but no significant loss of INA could be observed. Sea buckthorn juice shows a slight correlation between dry mass content and $T_{50,het}$ values: due to the filtration procedure of sea buckthorn juice a significant loss of dry mass and also a loss of INA ($\Delta T_{50,het}$ = 8.4 K) was achieved. For elderberry, no loss of dry mass could be measured, but still a huge loss in INA ($\Delta T_{50,het}$ = 6.8 K). Overall no correlation between INA and dry mass could be found; thus the INP quantity cannot be related to the dry mass content. All examined fruit juices have in common that the main quantity of solid particles, which are responsible for the total dry mass, is smaller than 0.45 µm. Thus a big part of INPs are particles in the submicron size range and these INPs can be macromolecules (INMs).

INMs could aggregate together and form larger particles or they could be absorbed on the surface of larger particles. These structures could change due to filtration process, whereby centrifugation was involved.

3.1.2 Solvent Experiments with Methanol, Methylene Chloride, and Cyclohexane

These experiments were performed to learn more about the polarity of the INPs of the five selected fruit juices. Extracts with three different solvents (methanol, methylene chloride, and cyclohexane) of the dried fruit juices were performed. These extracts were dried again separately and then each was dissolved in ultrapure water (for detailed preparation information see subchapter 2.3.2). After the solvent extracts were dissolved in ultrapure water again, they are hereinafter referred to as “aqueous solvent extracts”.

The polarity of the used solvents is declining in the order: methanol > methylene chloride > cyclohexane

Gravimetric Analysis

In most instances it was possible to dissolve the dried fruit juice residues in the lower section of the double-digit milligram range with methanol. With cyclohexane and methylene chloride just fruit juice residues in the number of single-decimal digits could be dissolved. These quantities are lower than the resolution of the analytical scale, therefore no mass balance could be prepared.

Methanol

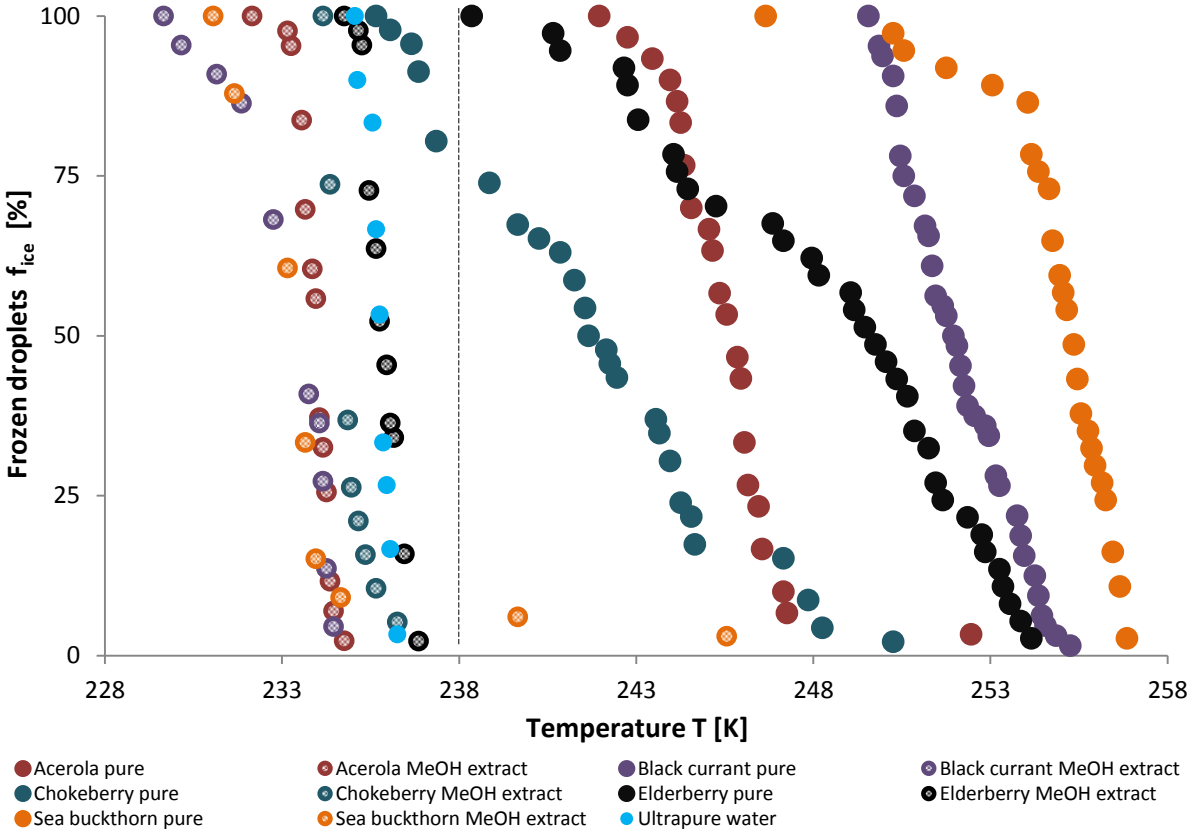

Figure 32: Freezing curves of the five pure fruit juices (filled circles), aqueous methanol extracts (checkered filled circles), and of the ultrapure water blank.

The $f_{ice,het}$ values of all aqueous solvent extracts are given in Table 9 and the freezing curves of the aqueous methanol extracts and the corresponding freezing curves of the pure juices are shown in Figure 32. Just a small frozen droplet fraction freezes heterogeneously for the aqueous methanol sea buckthorn extract ($f_{ice,het}$ = 6 %). All other aqueous methanol fruit juice extracts freeze homogeneously, therefore no INPs could be dissolved with methanol. The fact that small sugars and salts are soluble in methanol indicates their polarity. It are these osmotically active solutes, which lead to freezing point depression when redissolved from methanol into ultrapure water. This is true for acerola, black currant and sea buckthorn.

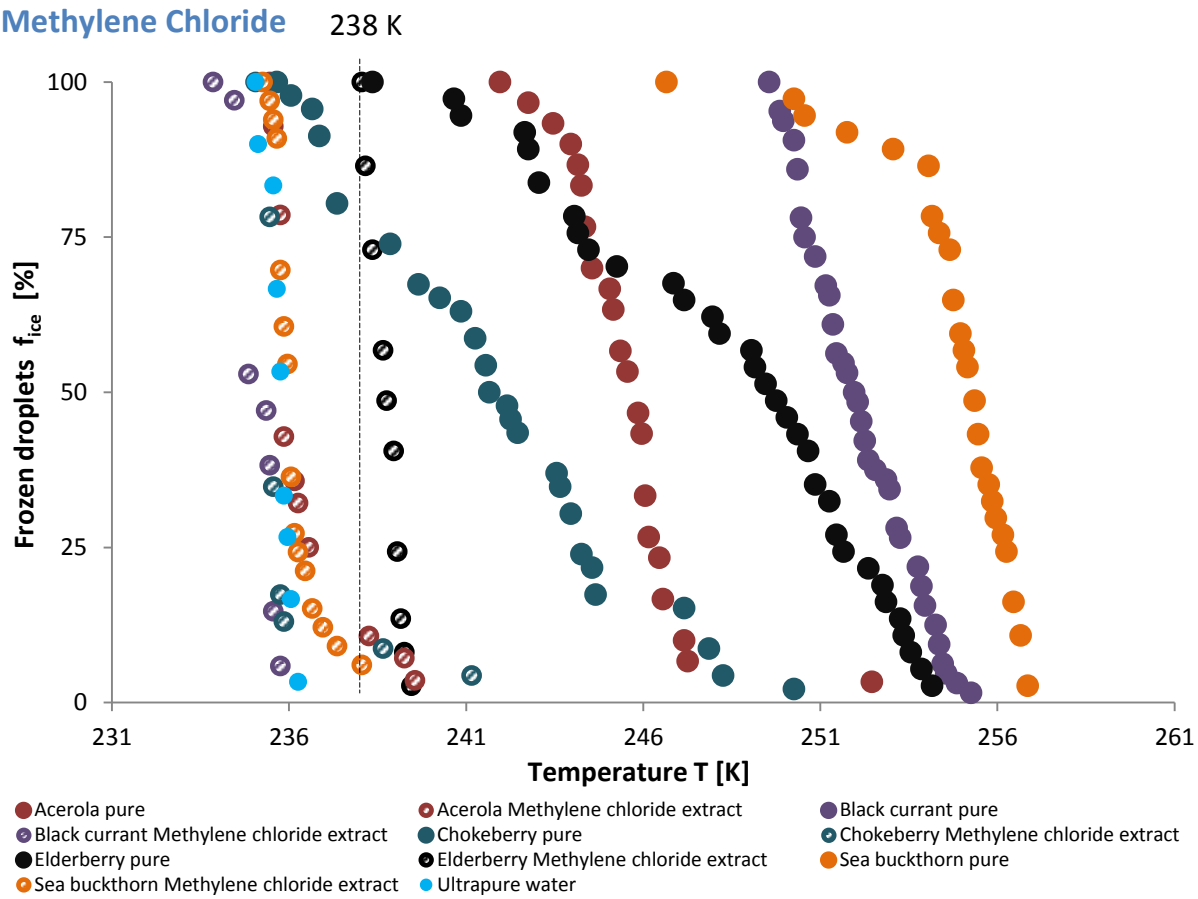

Figure 33: Freezing curves of the five pure fruit juices (filled circles), aqueous methylene chloride extracts (circles filled with diagonal lines), and of the ultrapure water blank.

In Figure 33 the freezing curves of the aqueous methylene chloride fruit juice extracts are illustrated, the corresponding $f_{ice,het}$ values are given in Table 9. The curves show a mostly steep progression (e.g. elderberry). Even though the freezing temperature is above 238 K for elderberry, homogeneous nucleation has to be assumed. We see a clear shift of the curve of about 3 K compared to the ultrapure water blank. Some curves exhibit a flattening in the beginning (e.g. chokeberry) or at the end of the freezing process (e.g. black currant) due to dependence on INP concentration and the possibility that various INPs are present in the droplets, which trigger freezing at different temperatures. All droplets of the aqueous methylene chloride black currant and sea buckthorn extracts freeze homogeneously. Heterogeneously frozen droplet fractions can be determined for the aqueous methylene chloride acerola extract 11 % and for the aqueous methylene chloride chokeberry extract 9 % (Table 9). Interestingly, for the aqueous methylene chloride elderberry extract this fraction is relatively high with 73 % (Table 9). However, the first droplets only froze very close to 238 K. A small proportion of the INPs of elderberry juice is obviously soluble in

methylene chloride (hydrophobic properties) and is subsequently also soluble again in ultrapure water (hydrophilic properties). This chemical behaviour suggests that only a few INPs of acerola, chokeberry and elderberry are compounds with an amphiphilic character. It is also an interesting fact that the dissolving process for elderberry cannot be observed via gravimetric analysis; this means that only a low quantity of INPs could be separated with this method.

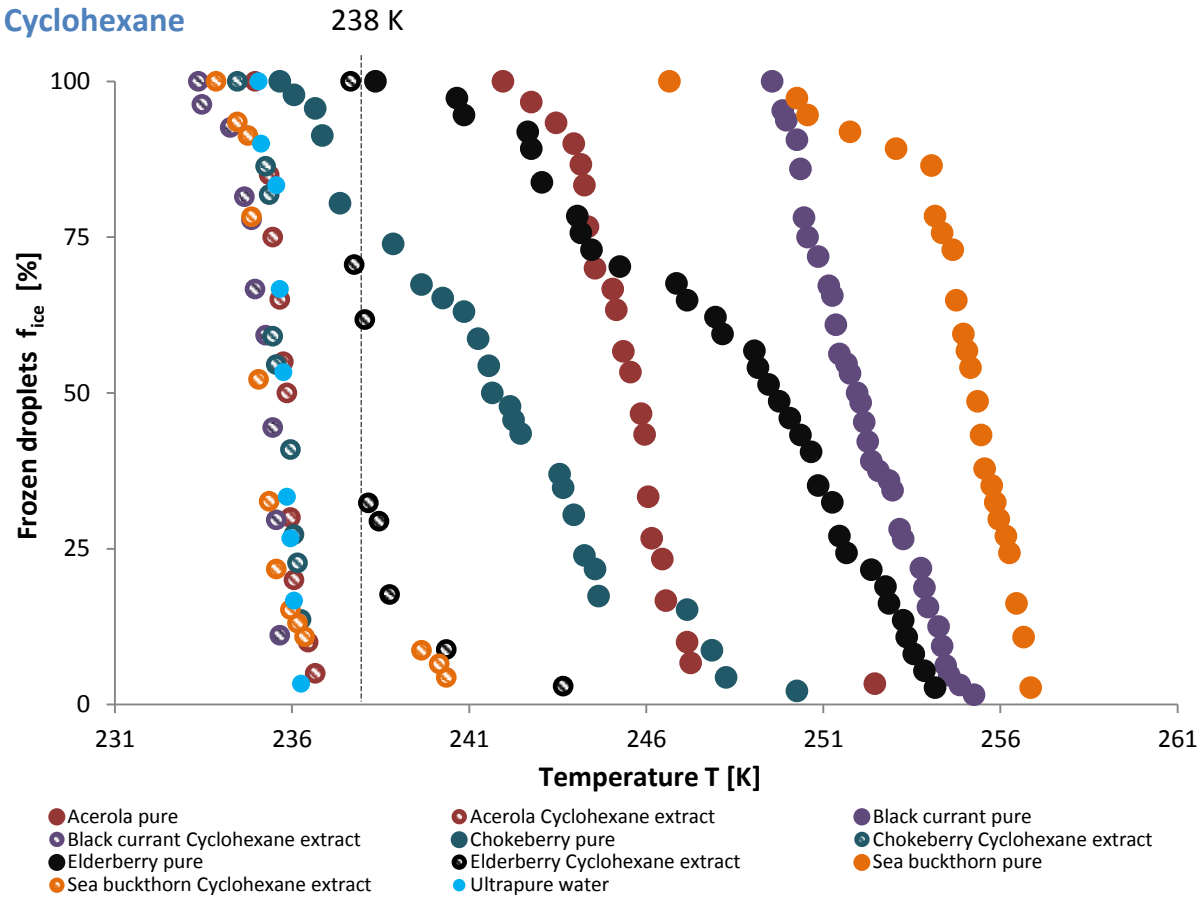

Figure 34: Freezing curves of the five pure fruit juices (filled circles), aqueous cyclohexane extracts (circles filled with diagonal lines), and of the ultrapure water blank.

The heterogeneously frozen droplet fractions can be determined for the aqueous cyclohexane elderberry extract 29 % and for the aqueous cyclohexane sea buckthorn extract 9 % (Table 9). The freezing curves of these two aqueous cyclohexane juice extracts are flatter in the beginning and steeper at the end of the freezing process (Figure 34). The aqueous cyclohexane extracts of acerola, black currant and chokeberry freeze entirely homogeneous with steep freezing curves.

Table 9: Associated $f_{ice,het}$ values of the aqueous solvent fruit juice extracts:

Fruit juices (pure)	Solvent	$f_{ice,het}$ [%]
Acerola	Methanol	-
	Methylene chloride	11
	Cyclohexane	-
Black currant	Methanol	-
	Methylene chloride	-
	Cyclohexane	-
Chokeberry	Methanol	-
	Methylene chloride	9
	Cyclohexane	-
Elderberry	Methanol	-
	Methylene chloride	73
	Cyclohexane	29
Sea buckthorn	Methanol	6
	Methylene chloride	-
	Cyclohexane	9

Our results indicate that amphiphilic components play a minor role in the INPs of acerola, chokeberry, elderberry, and sea buckthorn juice. This is not indicated for black currant juice, following the $f_{ice,het}$ values (Table 9) and the freezing curves (Figure 32, Figure 33, Figure 34). Especially for elderberry the results are very interesting, since the $f_{ice,het}$ results for the methylene chloride and the cyclohexane extract are the highest of all juices. The methanol treatment only worked out with sea buckthorn juice. For two fruit juices (acerola, chokeberry) it was possible to dissolve the INPs partially with methylene chloride and then dissolve it back in ultrapure water, but not with any other solvent. For two juices (elderberry, sea buckthorn) some of the INPs could be dissolved with the most non-polar solvent cyclohexane and then dissolved again in polar ultrapure water. In all cases no or only a minor fraction of the INPs was recovered. This can have two reasons: either they cannot be dissolved in the used solvent or they cannot be recovered with water after the solvent treatment due to structural rearrangements of the INPs. Consequently, it is thought that polar components play an important role in the ice nucleation activity of all fruit juices.

3.1.3 Experiments with Chaotropic Agents and a Protease

Experiments with GdmCl at Room Temperature

The experiments were carried out at room temperature (23±1 °C) for 24 hours to examine the effect of GdmCl on the INA of Snomax®, pure black currant and sea buckthorn juice. Immediately after a sample was drawn, it was diluted 1:10 with ultrapure water to decrease the salt concentration and stop the effects of GdmCl. Freezing point depression can occur due to GdmCl. Further information on the procedure can be found in subchapter 2.3.3. The results of these experiments are displayed in the following figures (Figure 35, Figure 36, Figure 37).

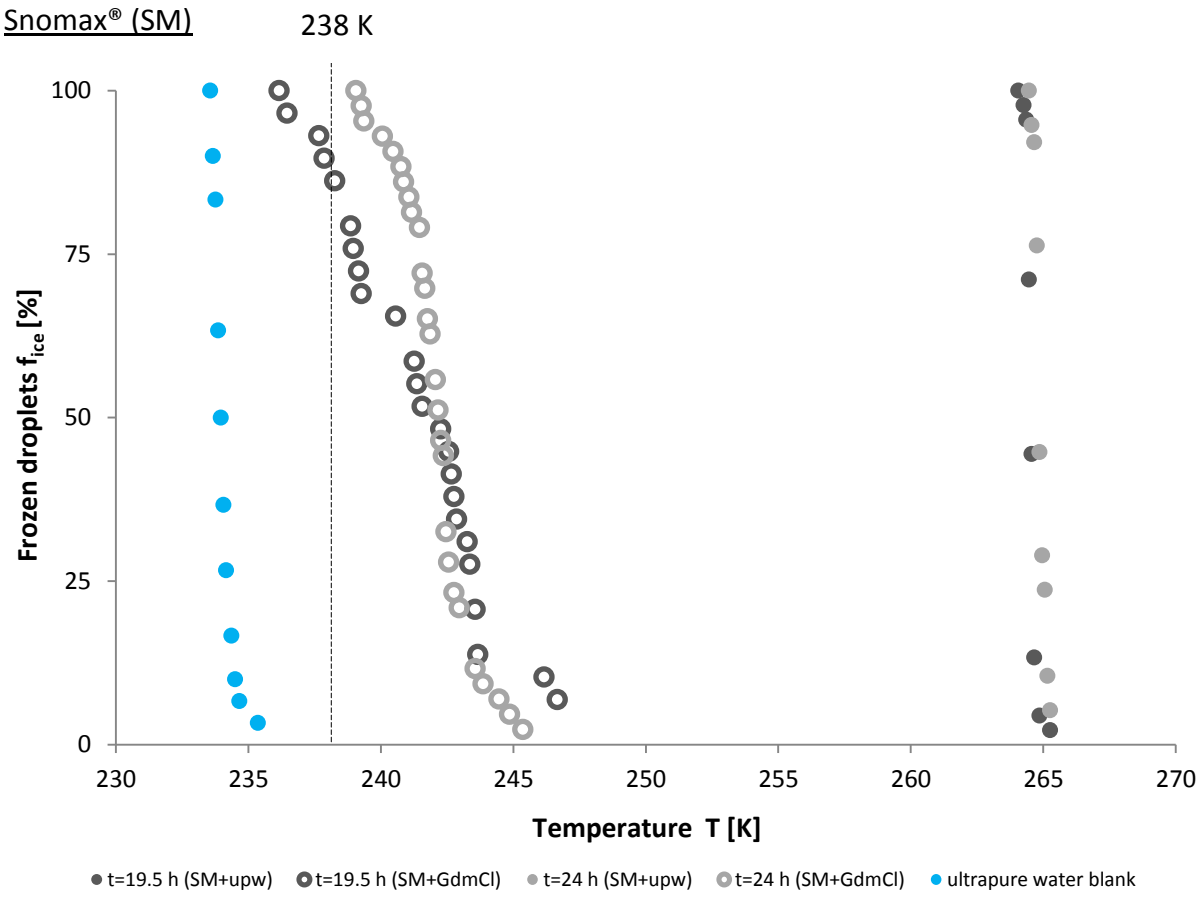

Figure 35: Freezing curves of Snomax® with GdmCl (empty circles) and solely with ultrapure water (filled circles) after 19.5 h and 24 h and of the ultrapure water blank.

In Figure 35 the extremely high INA loss of the Snomax® samples due to GdmCl compared to the untreated samples can be seen clearly due to the shift of the freezing curves to lower temperatures. The difference is for both sampling times (after 19.5 h and 24 h) more than

20 °C. However, after this harsh treatment, the diluted GdmCl samples still show INA, but it is drastically reduced.

Black currant (B)

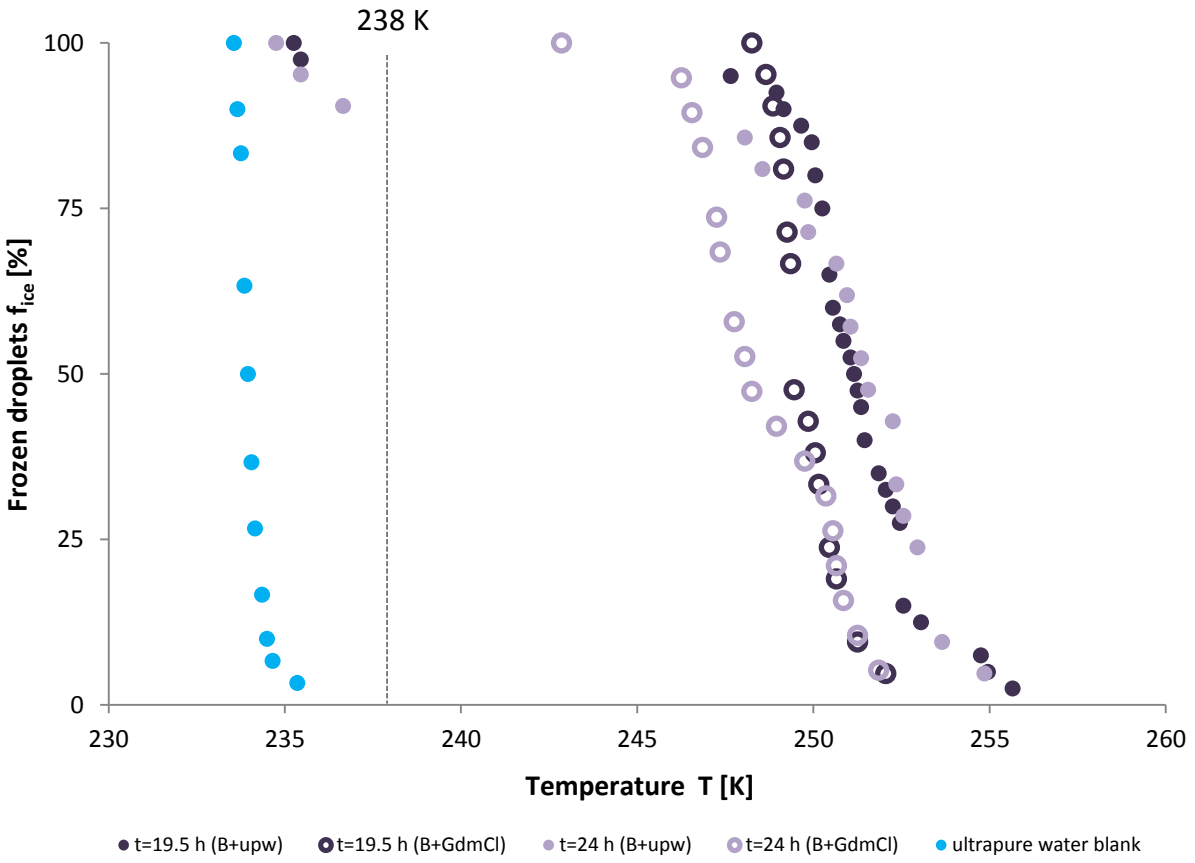

Figure 36: Freezing curves of black currant with GdmCl (empty circles) and solely with ultrapure water (filled circles) after 19.5 h and 24 h and of the ultrapure water blank.

Regarding the freezing curves of the black currant samples in Figure 36, the freezing curves of the GdmCl-containing samples are shifted to slightly lower temperatures. Nevertheless the differences between the freezing curves are not significant, when the freezing point depression due to the contained GdmCl is taken into account.

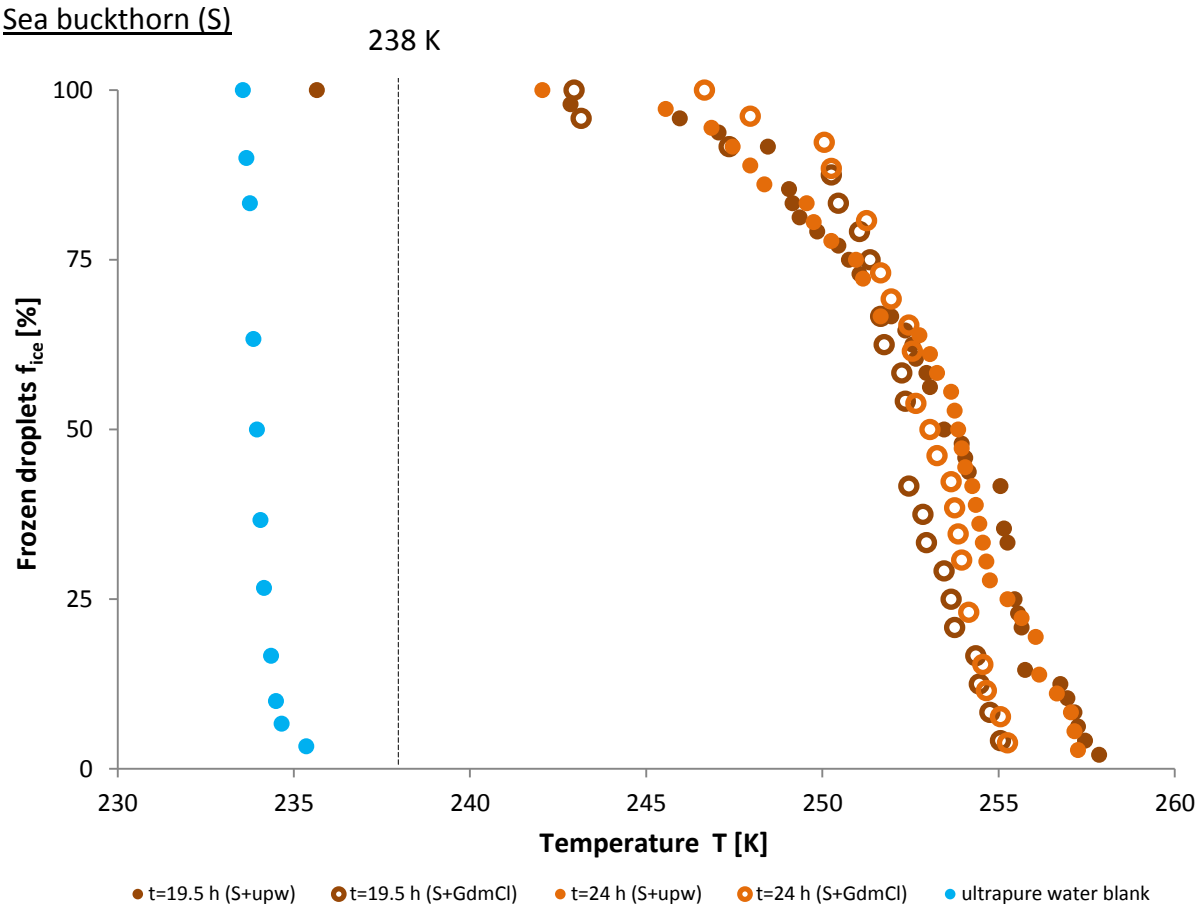

Figure 37: Freezing curves of sea buckthorn with GdmCl (empty circles) and with ultrapure water (filled circles) after 19.5 h and 24 h and of the ultrapure water blank.

The freezing curves of the sea buckthorn samples are illustrated in Figure 37, they are very close to each other, in fact they are almost coincident, when considering the freezing point depression owing to GdmCl and the error interval of the temperature values (±1 K). Surprisingly, the freezing point depression does not show a powerful effect here. Only the onset temperatures of the GdmCl treated samples are shifted to lower temperatures. The treated samples show a steeper slope, reaching higher $f_{ice,het}$ values at higher temperatures, even though their onset temperatures are shifted. This indicates a slight effect of GdmCl on sea buckthorn juice.

It is known that the INA of Snomax®, which consists of shredded Pseudmonas syringae fragments, derives from its membrane proteins (Lindow *et al.*, 1989). Therefore it was used as a positive control. In our experiments, the ice nucleating behaviour of Snomax® was drastically reduced, however, not completely destroyed by the usage of GdmCl. Concerning the investigated juices (pure black currant and sea buckthorn) GdmCl had no significant reducing effect on their INA.

It has to be mentioned that the concentration of Snomax® in solution was very high (approx. 88 mg/500 µl). This was done to match the dry mass concentration of black currant. In the following experiment with urea and Subtilisin a lower Snomax® concentration (approx. 1 mg/ml) was used for easier sample handling.

Experiments with Urea and Subtilisin at 60 °C

The experiments were carried out at 60 °C (59.5±1.5 °C) in a closable heating and shaking device for 24 hours to investigate the effects of urea, Subtilisin and heat on the INA of Snomax® (used as positive control), as well as pure black currant and sea buckthorn juice. Immediately after a sample was drawn, it was diluted 1:10 with ultrapure water to decrease the salt concentration and stop the effects of urea. Freezing point depression of the samples can occur due to urea and/or contained Tris-buffer. The results of the experiments with urea and Subtilisin at 60 °C are given in the following section. Additionally, a renaturation experiment was carried out to investigate the influences of urea on Snomax®, black currant and sea buckthorn juice.

Snomax® (SM)

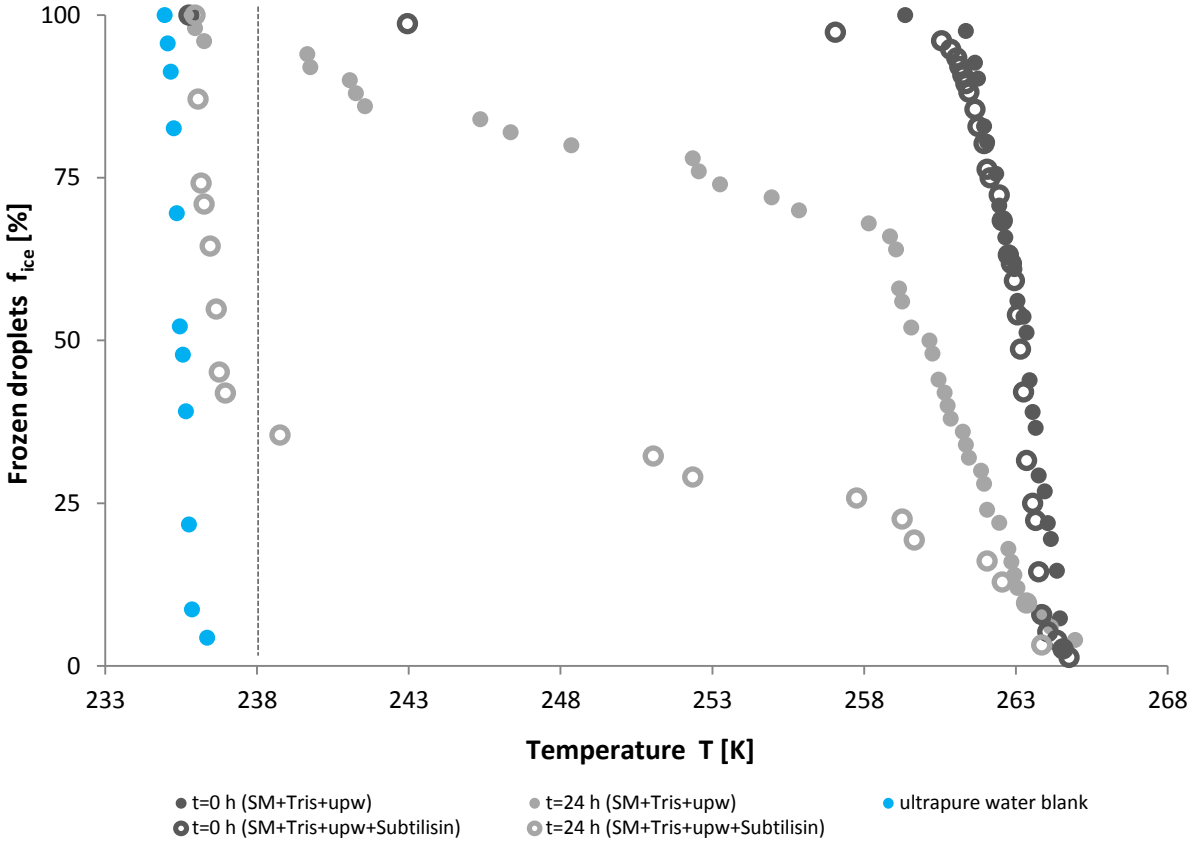

Figure 38: Freezing curves of Snomax® with aqueous Tris-buffer (filled circles) and additional with Subtilisin (empty circles) after 0 h and 24 h and of the ultrapure water blank.

Figure 38 shows the freezing curves of Snomax® treated with Subtilisin and untreated after 0 and 24 h at 60 °C. It is evident that the INA of the aqueous Snomax®-Tris-buffer sample decreases markedly after 24 hours caused by the heat treatment at 60 °C. The freezing curve of the zero sample of the aqueous Snomax®-Tris-buffer mixture with Subtilisin is nearly identical to the one of the aqueous Snomax®-Tris-buffer sample, except that the last droplets have a lower freezing temperature. The freezing curve after 24 h shows that the INA declines much faster due to the presence of Subtilisin ($f_{ice,het}$ = 35 %). This result indicates that the special membrane proteins acting as active sites are attacked by the protease Subtilisin, resulting in a lower INA of the bacterium.

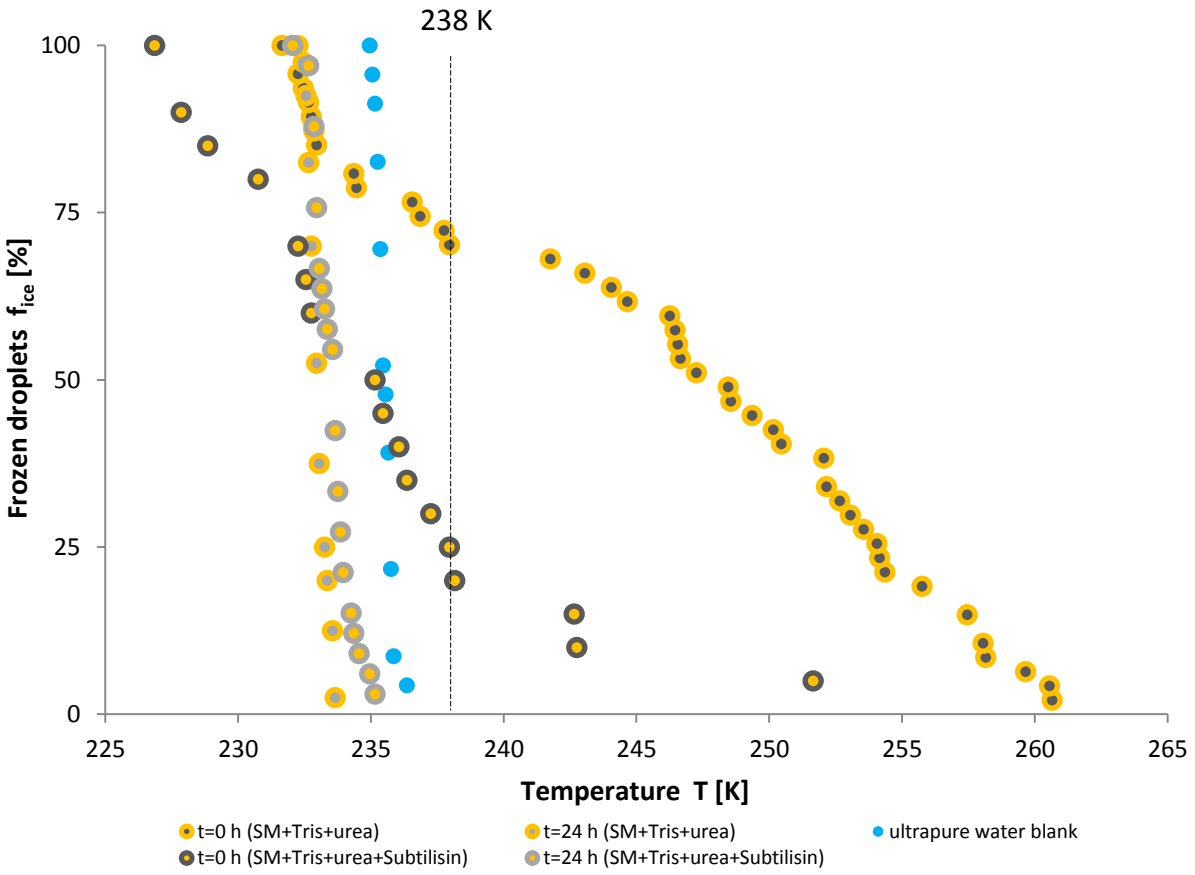

Figure 39: Freezing curves of Snomax® with urea-Tris-buffer (yellow framed circles) and additional with Subtilisin (grey framed circles) after 0 h and 24 h and of the ultrapure water blank.

According to Perlmann (1956) and Camilloni *et al.* (2008), urea is highly concentrated (as in the case here with 7.3 M prior to the 10-fold dilution) a denaturing agent, so it can disrupt reversibly the structure of a protein in its native state. In comparison, a protease (Subtilisin) is an enzyme that catalyses the hydrolysis of peptide bonds. This is an irreversible reaction since specific chemical bonds are cleaved by proteolytic enzymes. For this experiment the combination of urea and Subtilisin was selected, because even at high urea concentrations a residual hydrolysis activity of Subtilisin is retained. According to Guo and Clark (2001), even in urea concentrations as high as 8 M, 9.7 % of Subtilisins original activity remains catalytically active. The freezing curve of the Snomax®-Tris-buffer-urea mixture (t = 0 h) shows the highest INA of all samples in Figure 39. By comparison this freezing curve is considerably flatter than the both zero samples in Figure 38. The loss of INA is more drastical for the zero sample of Snomax®-Tris-buffer-urea with Subtilisin ($f_{ice,het}$ = 15 %) displayed in Figure 39 than for the Subtilisin treated sample without urea ($f_{ice,het}$ = 99 %) displayed in Figure 38. Interestingly, this sample possesses the freezing point depression to the lowest temperatures. After 24 h both samples freeze homogeneously. Based on the results of this

experiment we conclude that urea and Subtilisin have a strong effect on the ice nucleation behaviour of Snomax®. It is a suitable positive control for this investigation targeting the disruption of proteinaceous systems.

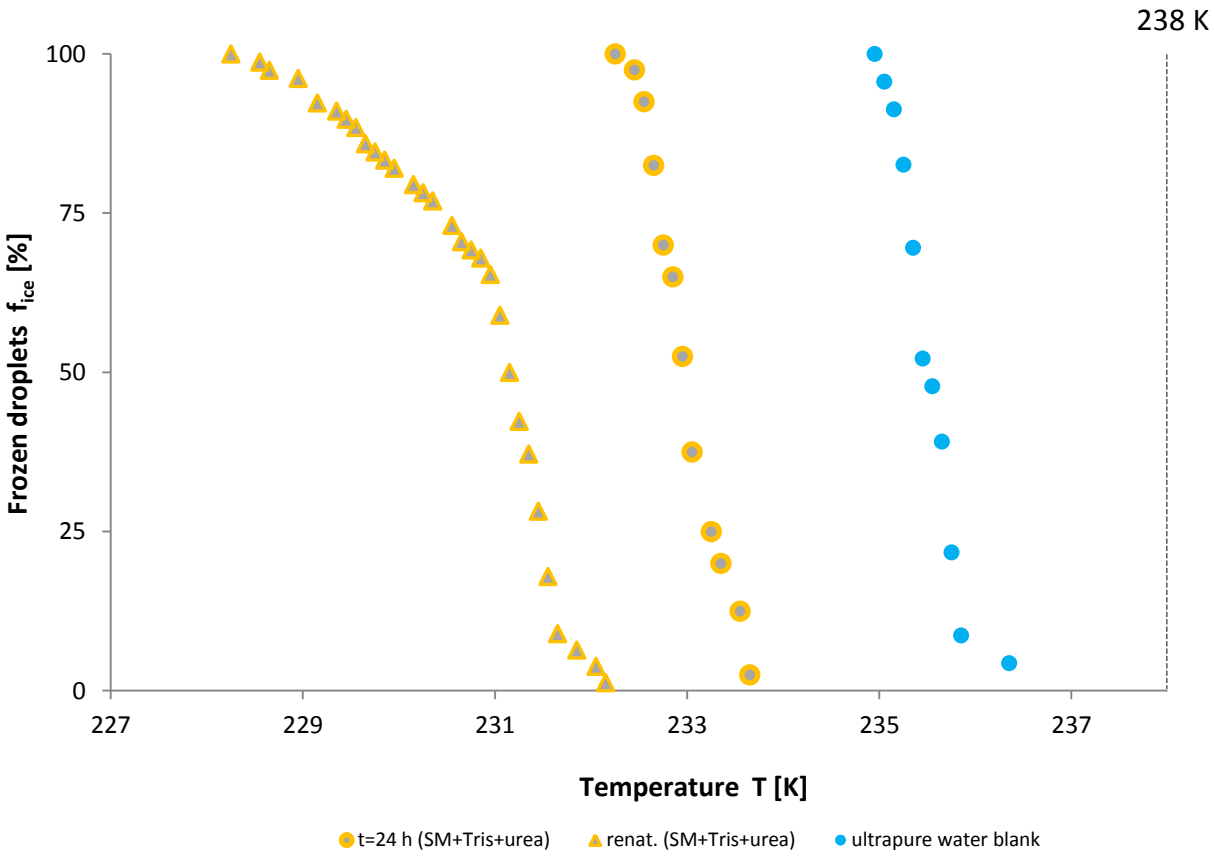

Figure 40: Freezing curves of the 24 h sample (Snomax®+Tris-buffer+urea) (circles) and of the identical sample that was additionally stored for 24 h at room temperature (triangles) and of the ultrapure water blank.

A renaturation experiment was carried out to investigate the influence of urea on the INA of the sample. The sample that was drawn after 24 h was diluted 10-fold with ultrapure water and a part of the sample was then left for 24 hours at room temperature (23±1 °C), to investigate if the renaturation proceeding has any effect on the INA. At lower concentrations, urea loses its effect of denaturation and therefore it should be possible that proteins undergo a partial recovery from this treatment. Figure 40 shows the Snomax®-Tris-buffer-urea freezing curves of the sample, which was drawn after 24 h. Prior measurement the sample was diluted (circles, already illustrated in Figure 39). The renaturated sample is represented using triangles. Due to this renaturation experiment it was not possible to enhance the INA, in fact a freezing point decrease of approximately two degrees could be

determined. This result could be based on the formation of antifreeze compounds (e.g. AFPs).

Black currant (B)

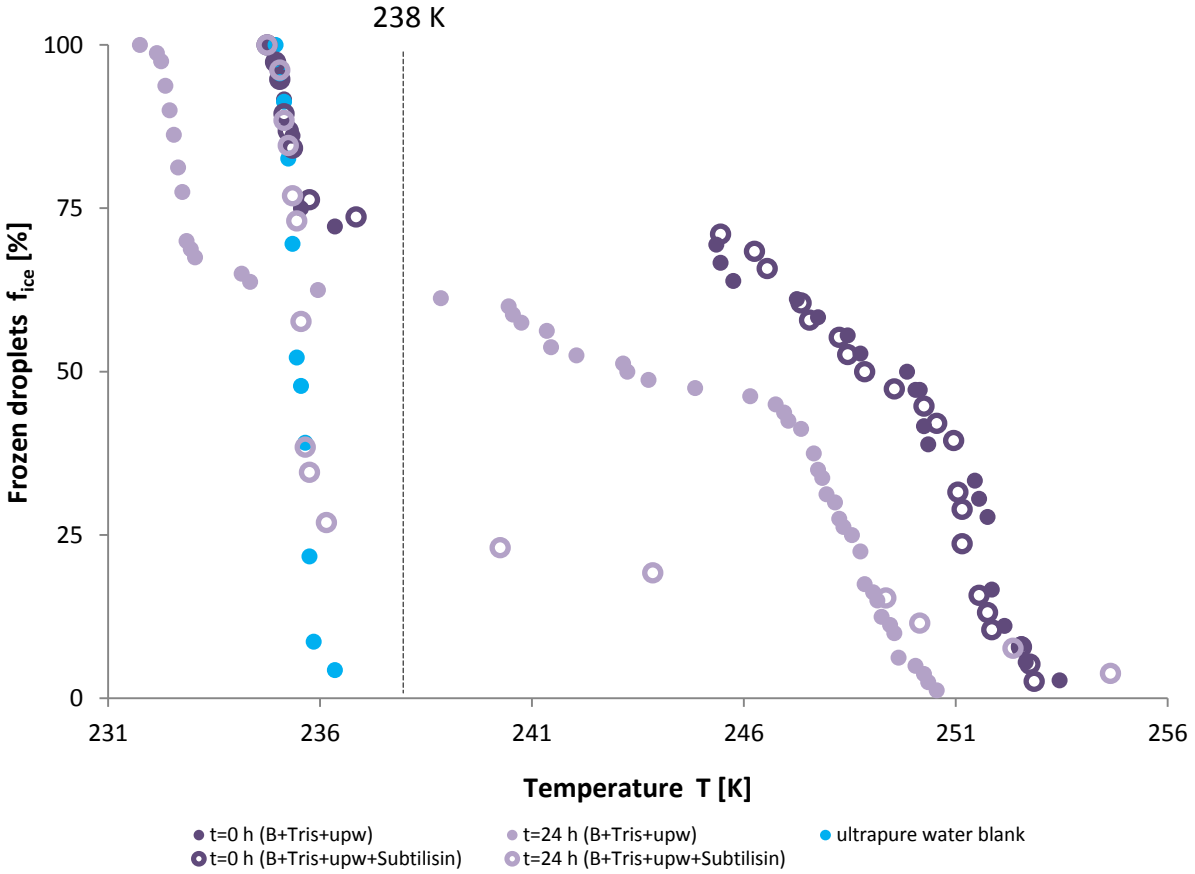

Figure 41: Freezing curves of black currant with ultrapure water-Tris-buffer (filled circles) and additional with Subtilisin (empty circles) after 0 h and 24 h and of the ultrapure water blank.

As in the case with Snomax® (Figure 38) the aqueous black currant-Tris-buffer samples in Figure 41 lose noticeably INA solely due to the heat treatment (t = 24 h). Interestingly, freezing point depression of the aqueous black currant-Tris-buffer sample (t = 24 h) occurs. The freezing curves of aqueous black currant-Tris-buffer samples (t = 0 h) with and without Subtilisin are almost identical. The INA loss of the aqueous black currant-Tris-buffer sample with Subtilisin ($f_{ice,het}$ = 23 %) is considerably more pronounced then the activity loss of the sample just undergoing heat treatment.

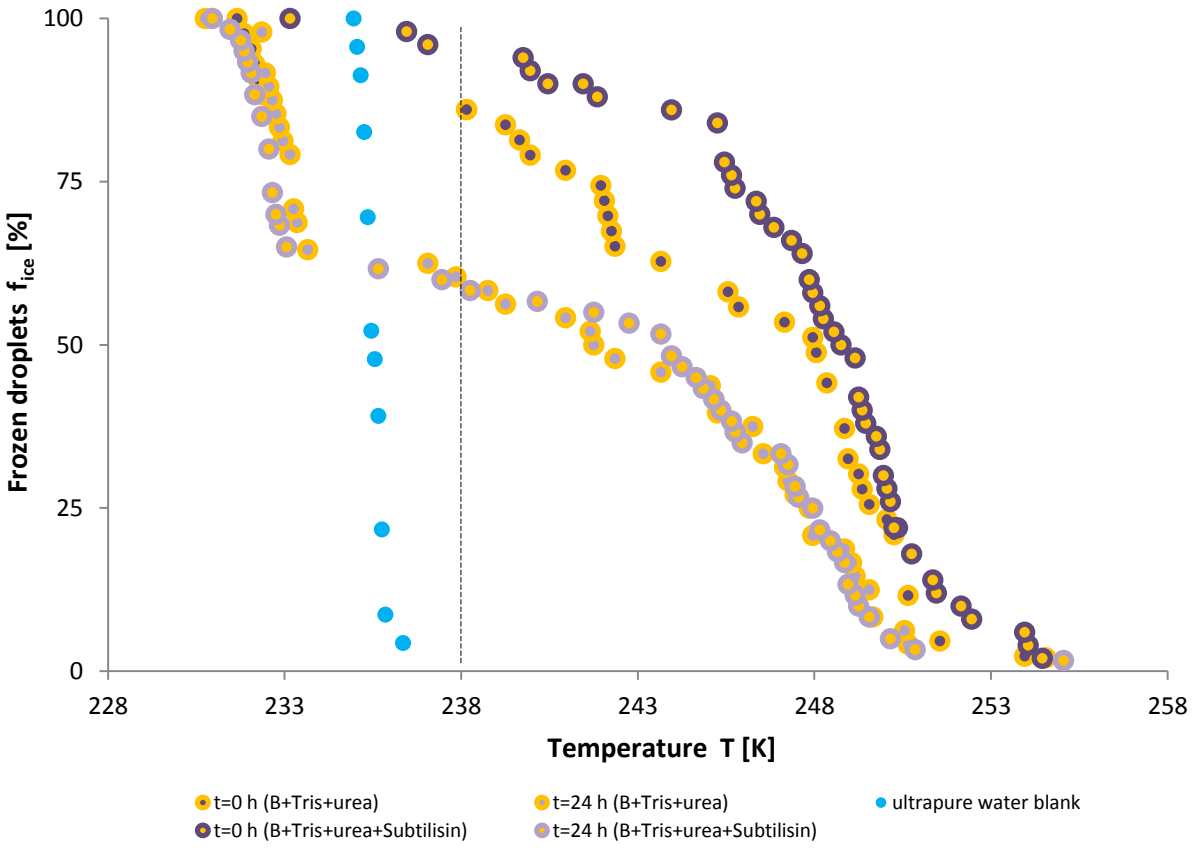

Figure 42: Freezing curves of black currant with urea-Tris-buffer (yellow framed circles) and additional with Subtilisin (violet framed circles) after 0 h and 24 h and of the ultrapure water blank.

The freezing curves of the black currant samples with urea and urea with Subtilisin lead to a decrease in INA to the same extent ($f_{ice,het}$ = 58 %) after 24 hours. Therefore no significant difference could be detected between the both samples. All samples show freezing point depression.

The renaturation experiment of the urea containing black currant sample did not show an INA-enhancing effect.

The experiments show that the strong INA loss of the Subtilisin-containing black currant sample could be an indication that proteins play a role in its INA. Urea does not have a strong effect on the INA of black currant.

Sea buckthorn (S)

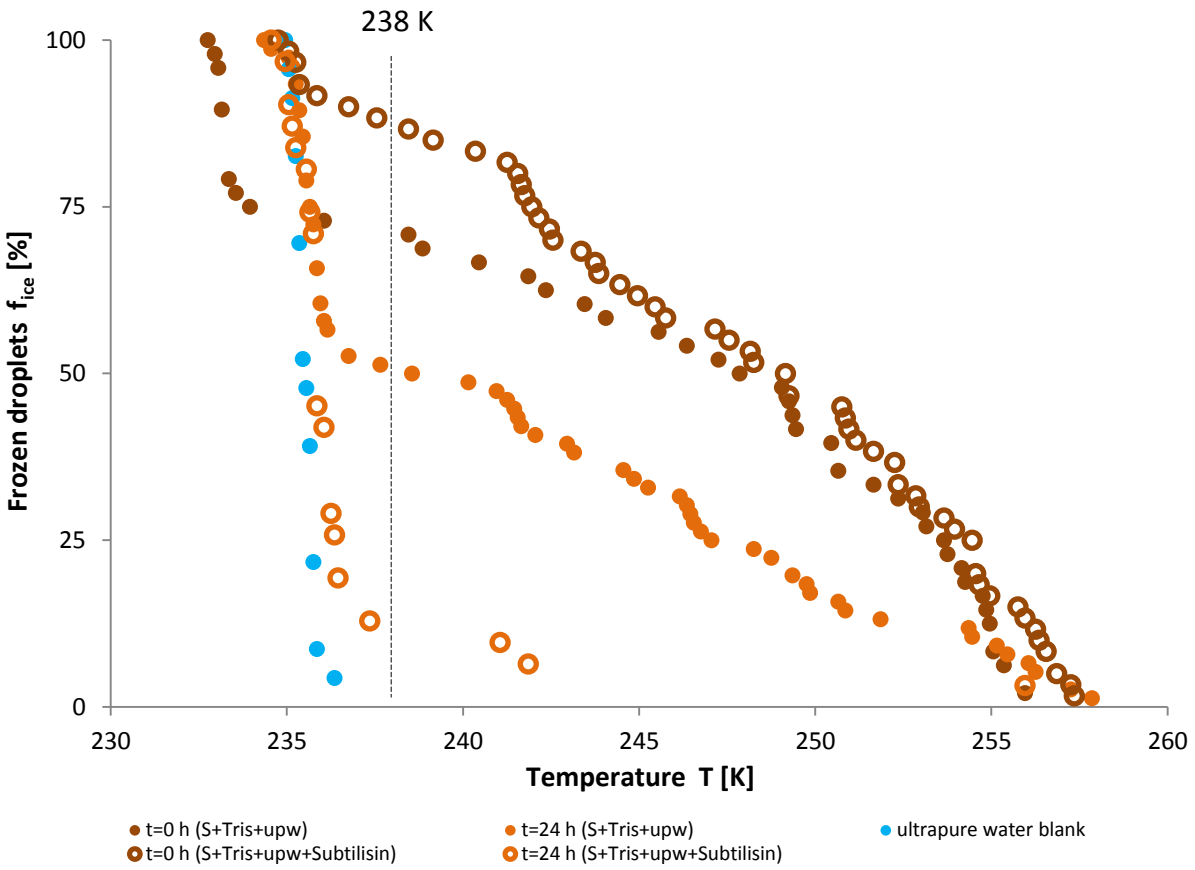

Figure 43: Freezing curves of sea buckthorn with ultrapure water-Tris-buffer (filled circles) and additional with Subtilisin (empty circles) after 0 h and 24 h and of the ultrapure water blank.

The Subtilisin treatment on sea buckthorn (Figure 43) shows the same effect, as has already been seen for the freezing curves of Snomax® (Figure 38) and black currant (Figure 41). A greater decline of INA occurs for the aqueous sea buckthorn-Tris-Subtilisin ($f_{ice,het}$ = 10 %) than for the aqueous sea buckthorn-Tris sample without the protease ($f_{ice,het}$ = 50 %). Interestingly, the aqueous sea buckthorn-Tris sample (t = 24 h) is the only one that shows freezing point depression.

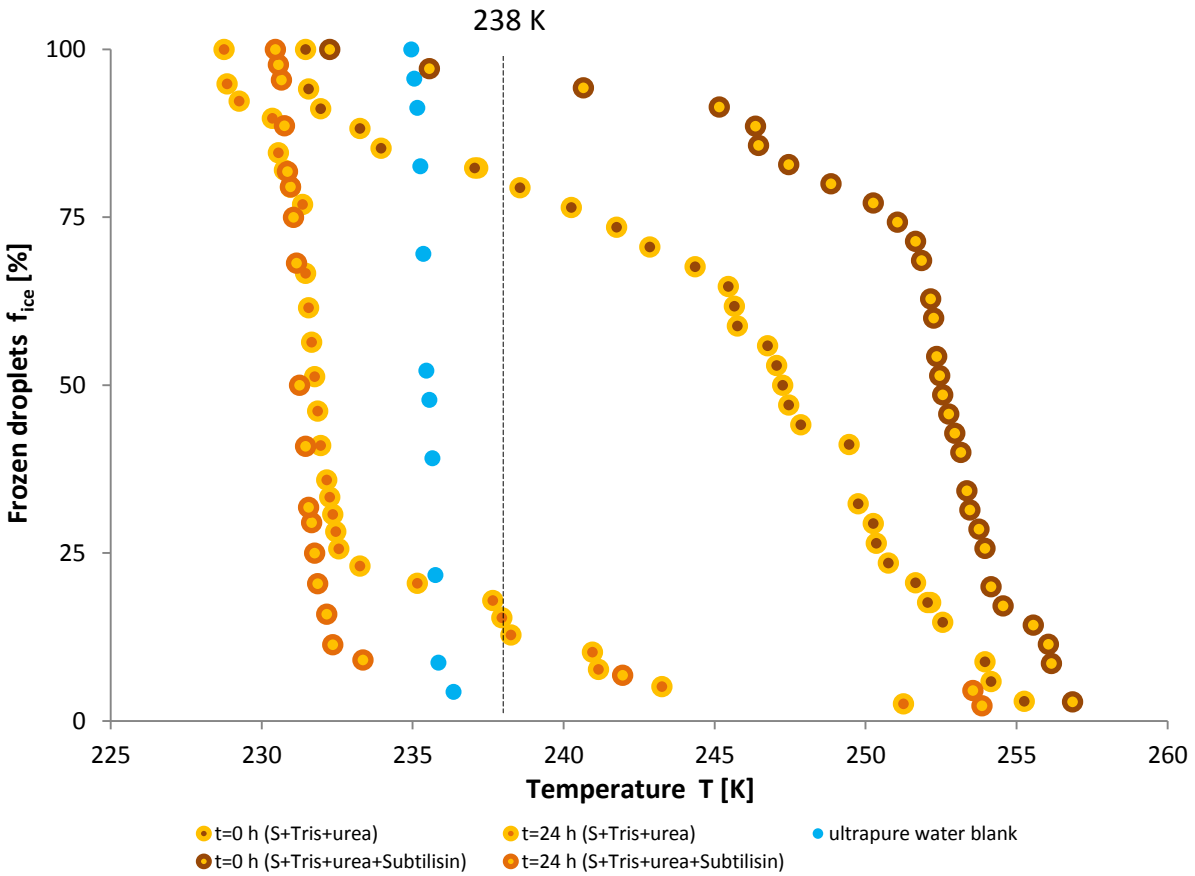

Figure 44: Freezing curves of sea buckthorn with urea-Tris-buffer (yellow framed circles) and additional with Subtilisin (orange framed circles) after 0 h and 24 h and of the ultrapure water blank.

By consideration of the freezing curves in Figure 44 it is obvious that in the course of the experiment both samples lose INA, whereat the loss of the Subtilisin and urea containing sample is stronger ($f_{ice,het}$ = 7 %) than for the sample, where Subtilisin is not present $f_{ice,het}$ = 15 %). All samples show freezing point depression.

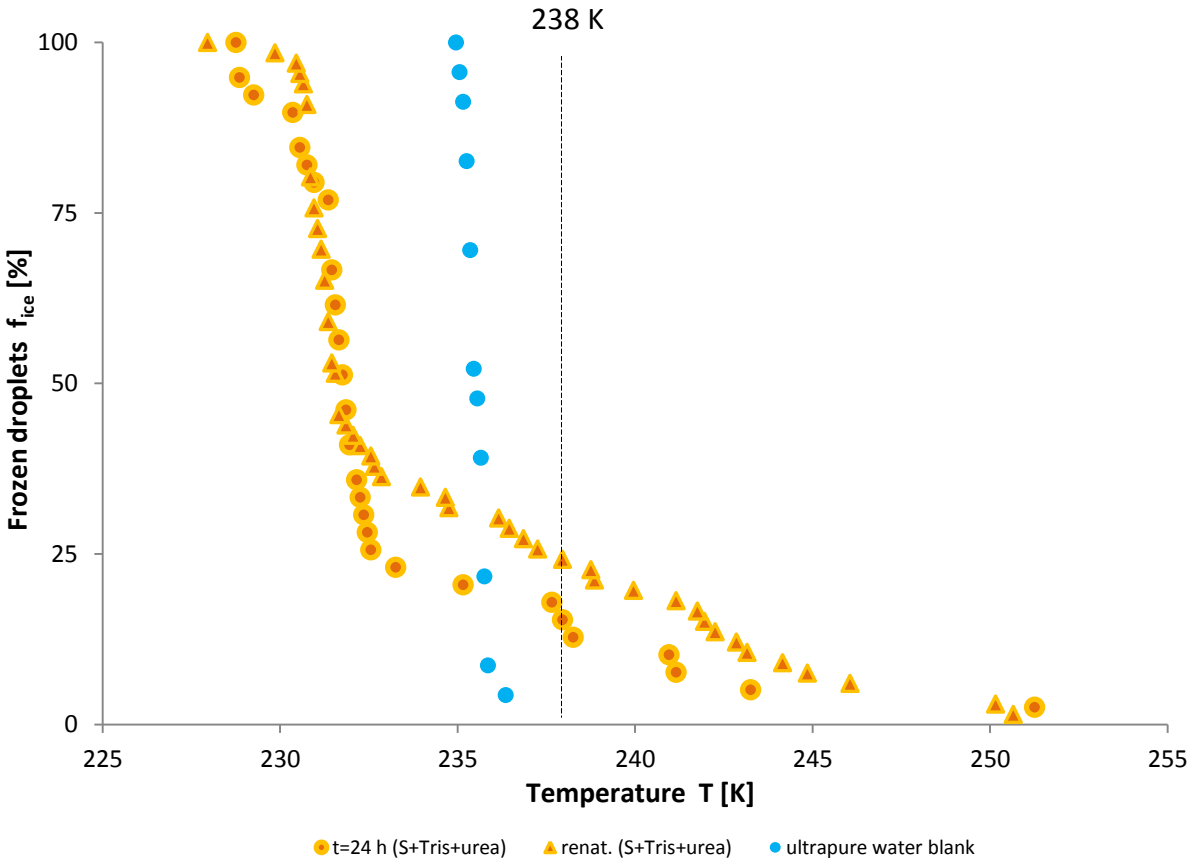

Figure 45: Freezing curves of the 24 h sample (sea buckthorn+Tris-buffer+urea) (circles) and of the same sample that was additionally stored for 24 h at room temperature (triangles) and of ultrapure water.

The renaturation experiment of sea buckthorn is the only one, where the INA of the renaturated sample was enhanced in comparison to the 24 h sample (Figure 45). This result indicates that proteins could be involved in the INA of sea buckthorn.

For all three samples (Snomax®, black currant, and sea buckthorn juice), it could be shown that a stronger INA decrease of the Subtilisin containing samples takes place than for the samples, which contain only aqueous Tris-buffer. This result indicates that the protease Subtilisin has an influence on the INA of these three samples. Consequently, it can be assumed that proteins play a role in INPs of black currant and sea buckthorn juice.

In Table 10 the results of the experiments of subchapter 3.1.3 are presented in a summarized form.

Table 10: Overview of the results of the experiments with chaotropic agents (GdmCl, urea) and a protease (Subtilisin). Given results relate to 24 hours of treatment. Abbreviations: (RT) room temperature, (-) treatment has no effect on the INA of the sample, (+) treatment has an effect on the INA of the sample, (++) treatment has a strong effect on the INA of the sample.

Samples	Sampling time [h]	Temperature [°C]	Snomax®	Black currant	Sea buckthorn
upw	24	RT	-	-	-
GdmCl	24	RT	++	-	-
Tris+upw	24	60	+	+	+
Tris+upw+Subtilisin	24	60	++	++	++
Tris+urea	24	60	++	+	++
Tris+urea+Subtilisin	24	60	++	+	++
Renaturation (Tris+urea)	-	RT	-	-	+

3.2 UV-VIS Determination of the Juices and of the Solvent Experiments

UV-VIS absorption spectra from the different fruit juices were recorded. These spectra could be used to analyse the samples in order to point out differences and similarities between the five different fruit juices regarding their composition. The UV-VIS spectra are displayed in the wavelength range of 230 to 400 nm, this is the region where significant absorbance signals appear. We find no signals in the visible range (> 380 nm).

As described in subchapter 2.3.4 the pure black currant, chokeberry and elderberry juice could be measured without any difficulties. Because of the high particle fraction of acerola and sea buckthorn juice, which would lead to a falsification due to scattering of the light on these particles, the sedimented, particle free juices were measured. The dilutions of the samples are given below the respective figure.

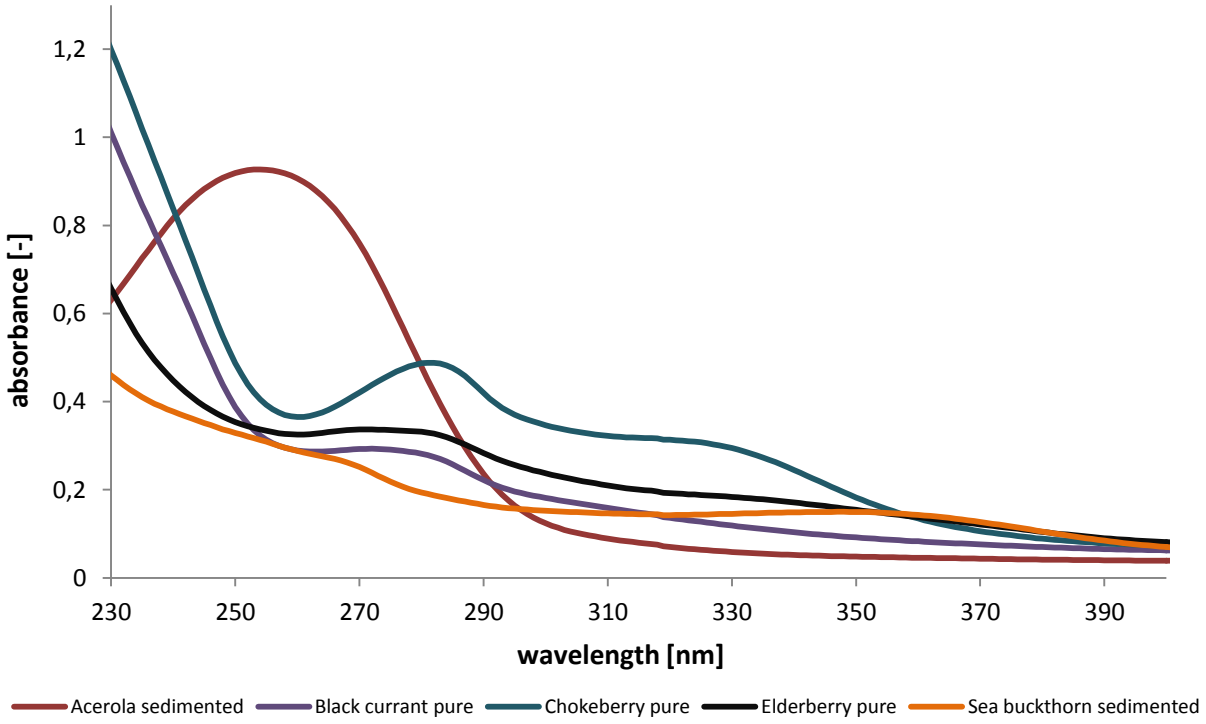

Figure 46: Absorption spectra of the five different fruit juices (pure or sedimented) diluted in ultrapure water (1:600).

In Figure 46 the absorption spectra of the pure or sedimented and diluted fruit juices are illustrated. Chokeberry juice has a relative absorption maximum at 281 nm and also a broad absorption band in the direction to higher wavelengths. The absorption spectra of black currant and elderberry juice have a similar shape from 267 nm to higher wavelengths. When comparing the absorption spectra of all five juices, sea buckthorn and acerola (absolute absorption maximum at 254 nm) juice behave unique, meaning that the two juices show no clear similarities in curve progression compared to the other three juices. As mentioned before, from a wavelength value of 380 nm the absorbance of all five fruit juices is barely visible; therefore the measured wavelength range above 400 nm is not included in Figure 46 and in the following figures.

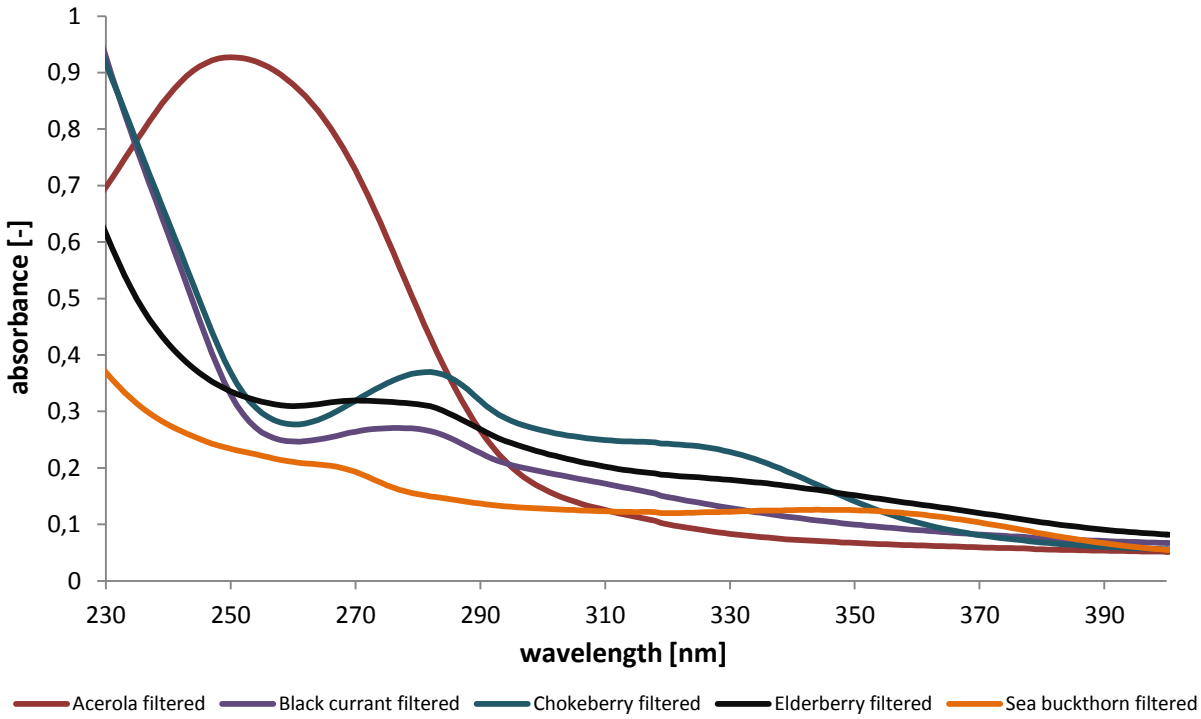

Figure 47: Absorption spectra of the five different, filtered fruit juices diluted in ultrapure water (1:600).

The comparison between the pure or sedimented juices (Figure 46) and the filtered ones (Figure 47) illustrates that the filtration process causes few alterations in the absorbance of the fruit juices. In general, the curve progression of the different filtered juices is the same as for the pure or sedimented juices.

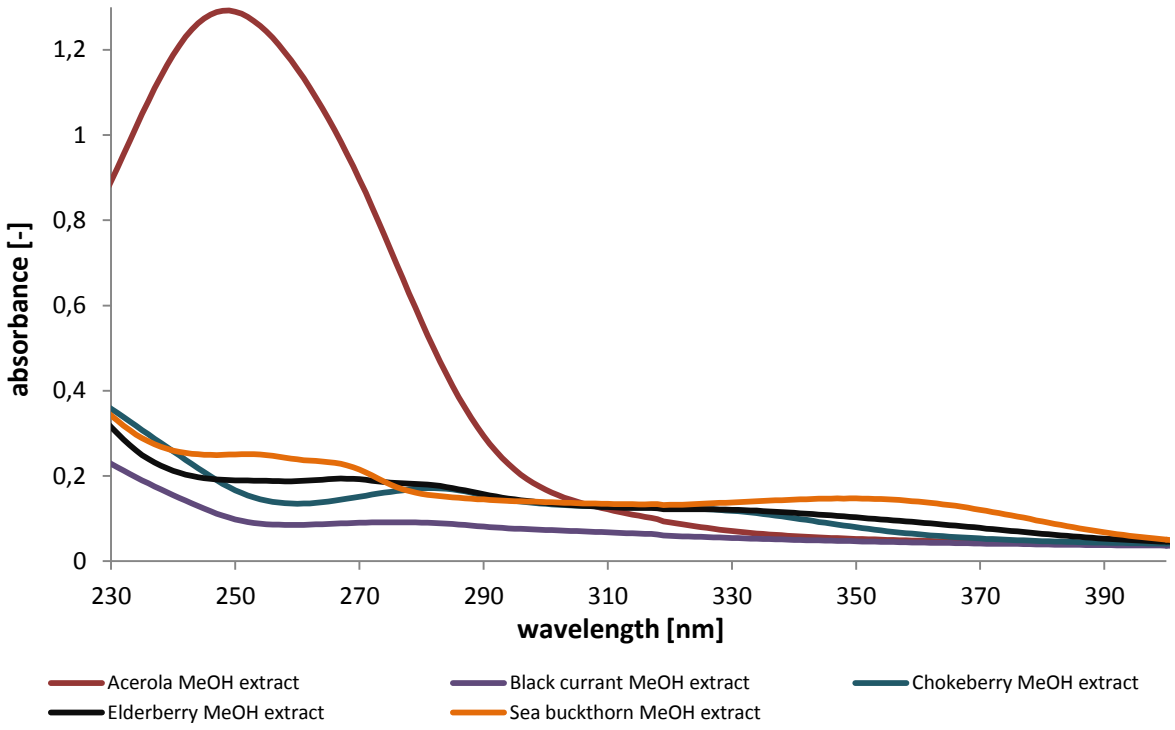

Figure 48: Absorption spectra of the five aqueous methanol fruit juice extracts, diluted in ultrapure water (1:150).

Methanol is a rather polar solvent and can therefore dissolve well polar compounds out of the dried fruit juice residues. According to Figure 48 the absorbance of the aqueous acerola methanol extract is distinctively higher at lower wavelengths than of the other four aqueous fruit juice extracts.

The UV-VIS absorption spectra of the aqueous fruit juice extracts of methylene chloride (dilution 2:15) and cyclohexane (dilution 1:15) are very similar and do not point out any characteristic signals or clearly visible bands and therefore the spectra are not shown.

In Table 11 the results of the experiments of subchapter 3.2 are presented in a summarized form.

Table 11: Overview of the absorption maxima of the UV-VIS spectra of the juices (pure or sedimented, filtered, aqueous methanol extract).

Samples		Maxima [nm]
Acerola	sedimented	254
	filtered	251
	aqueous methanol extract	249
Black currant	pure	271
	filtered	277
	aqueous methanol extract	-
Chokeberry	pure	281
	filtered	281
	aqueous methanol extract	-
Elderberry	pure	271
	filtered	271
	aqueous methanol extract	-
Sea buckthorn	sedimented	-
	filtered	-
	aqueous methanol extract	-

3.3 ATR-FTIR Characterization of the Pure Juices

FTIR spectroscopy was applied to investigate similarities and differences in chemical composition of the pure fruit juices. For the reduction of fluctuations in the IR spectrum, the method of five point FFT (abbreviation for “Fast Fourier Transform”) smoothing was applied on every sample spectrum. Therefore we used the software OriginPro 2016G.

The characteristic bands in the IR spectrum are in general broader, thus overlapping of the bands (Pummer, 2013) and vibrational interaction of all the atoms can occur. For that reason and since biological fruit juices consist of a large number and various content of different primary (proteins, lipids, carbohydrates) and secondary (terpenes, phenolic and nitrogenous compounds (Brechner *et al.*, 2001)) plant metabolites, no detailed elucidation of the IR fruit juice spectra can be given. Nonetheless the following part will try to work out similarities and differences between the juices and to assign characteristic bands to molecular groups.

The spectra were baseline corrected (five point FFT-smoothed). The pure fruit juices are shown in Figure 49 (3600 - 750 cm^{-1}) and in Figure 50 (1800 - 750 cm^{-1}). The possible assignments of the band positions are listed in Table 12.

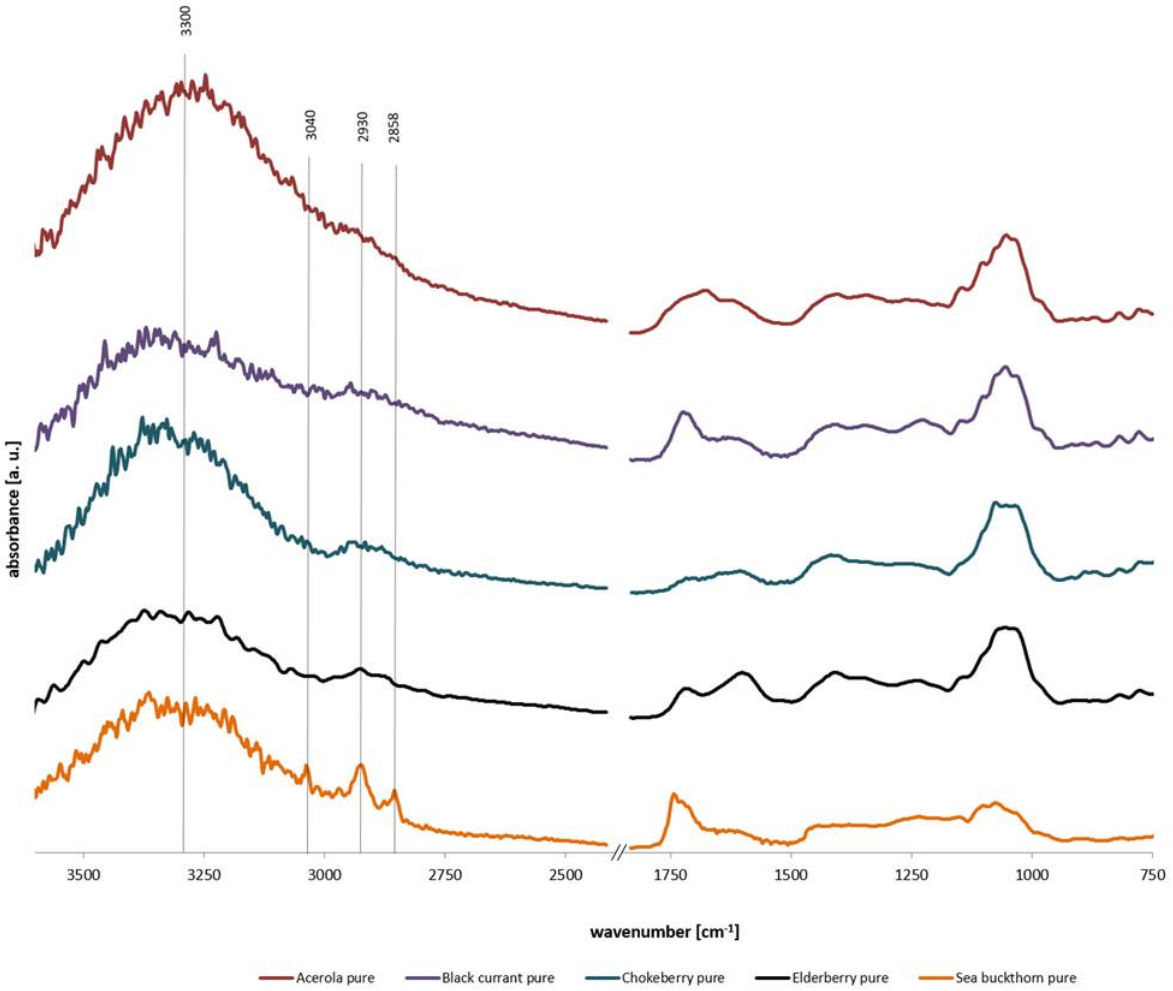

Figure 49: FTIR spectra of the pure fruit juices (sea buckthorn in orange, elderberry in black, chokeberry in petrol, black currant in violet and acerola in red) between 3600 cm^{-1} and 750 cm^{-1}. Possible assignments of the bands are listed in Table 12.

The spectral range at higher wavenumbers is an extremely broad intensity region with its maxima at about 3300 cm^{-1} that is related to the characteristic O-H and N-H stretching vibration (Figure 49). The range of 3100 to 2850 cm^{-1} is associated to the C-H stretching vibration, only for pure sea buckthorn juice three relatively sharp signals could be detected at 3040 cm^{-1}, 2930 cm^{-1} and 2858 cm^{-1}. For the other juices in Figure 49, we can observe that absorption occurs, but also other bands are located here, so all in all we just see a broader shoulder.

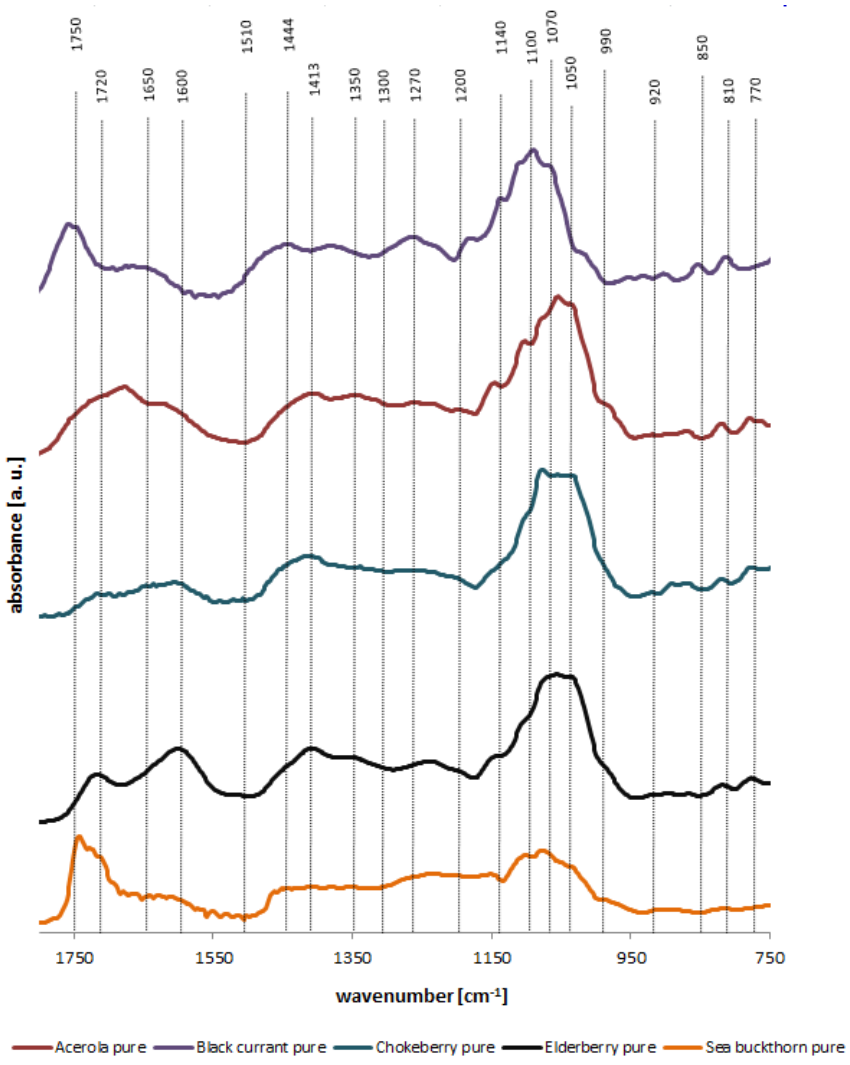

Figure 50: Enlarged part of the lower wavenumber region of the FTIR spectra of the pure fruit juices from Figure 49 between 1800 cm^{-1} and 750 cm^{-1}.

In Figure 50 the right, low-frequency parts of the spectra are illustrated, for a better presentation of the band positions. In this spectral region an array of bands occurs. In the different fruit juices we found a large number of strong bands, which are characteristic for saccharides (1200 to 800 cm^{-1}) (Kačuráková *et al.*, 2000). The absorption pattern in this spectral range of black currant and acerola juice is similar, as well as those of chokeberry and elderberry. The intensity of sea buckthorn is lower than for the other juices in this region. Some of the bands are resulting from phenolic compounds (1200 cm^{-1}, 920 cm^{-1}, 850 cm^{-1}, 810 cm^{-1}) and also the occurrence of lipid bands (1750 cm^{-1}, 1444 cm^{-1}) can be observed. In particular, black currant and sea buckthorn juice show strong bands at approx. 1750 cm^{-1} (C=O stretch). For all five juices we found broader bands in the different amid regions (Amid I – III) (see Table 12). Except for acerola, where no intensity could be detected at 1510 cm^{-1}.

In these regions also bands of other compounds can occur, hence the presence of proteins cannot be assured with certainty.

Table 12: Assignments for the FTIR-bands of the five pure fruit juices (Miyazawa *et al.*, 1956; Kačuráková *et al.*, 2000; Pretsch *et al.*, 2001; Günzler and Gremlich, 2003; Schulz and Baranska, 2007; Chen *et al.*, 2010; Smith, 2011; Pummer *et al.*, 2013).

ATR-IR band wavenumber [cm^{-1}]	Assignment
3300	O-H stretch, N-H stretch
3040	C-H stretch
2930	C-H stretch
2858	C-H stretch
1750	C=O stretch (lipids, polysaccharides)
1720	C=O stretch
1650	C=O stretch, C=C stretch, Amid I
1600	C=O stretch, C=C stretch, Amid I
1510	C=O stretch, Amid II
1444	CH deformation (pectin), CH_2 deformation (lipids)
1413	C-O stretch
1350	C-H deformation
1300	C-N deformation, Amid III
1270	C=O stretch, Amid III
1200	Phosphate, C-C-O of phenolic compounds
1140	C-O-C stretch (pyronase rings), C=O stretch (aliphatic groups), Tyrosine, Tryptophane, Guanine
1100	Sugar skeletal vibration
1070	C-H stretch, C-C stretch
1050	C-H stretch, C-C stretch
990	OCH_3 (polysaccharides)
920	C=C (polysaccharides – ß-linkage, phenolic compounds)
850	C-O-C skeletal mode (polysaccharides – α - linkage, phenolic compounds)
810	C=O deformation (phenolic compounds)
770	Phosphate stretch

The wavenumber regions of the FTIR-spectra, which contain no significant information (in particular: > 3600 cm^{-1}, < 750 cm^{-1}, and between 2415 and 1833 cm^{-1}) are not shown in Figure 49 and Figure 50.

4 Discussion

Our results reveal that all five examined fruit juices (pure) exhibit INA expressed as $T_{50,het}$ values in the temperature range from -17.9 to -29,6 °C. In all filtered fruit juices (< 0.45 µm), INPs are still present, which counts for macromolecular INPs. No further information is known about the particle size distribution of the INPs in the submicron size range. It is possible that the submicron INPs we found are similar in size to the INMs as described by Pummer *et al.* (2012, 2015)[21]. An INA loss of all fruit juices in varying extents took place due to the filtration procedure and therefore either coarse INPs are contained in the five pure fruit juices or some INPs are attached to the coarse particle fraction e.g. by absorption.
If submicron INPs become airborne, they can have a longer residence time in the atmosphere due to their small size. These tiny INPs, probably including nanoparticles, can further be absorbed by other aerosol particles (e.g. kaolinite (O'Sullivan *et al.*, 2016)), whereby biological active sites are added to abundant mineral dust particles.

Jann *et al.* (1997) also found INA of sea buckthorn berries after filtration on a membrane with a mesh size of 0.45 µm and concluded therefore that the INPs originate from sea buckthorn berries and not from bacteria (epiphytic organisms). Lundheim and Wahlberg (1998) examined filtered (through 0.2 µm mesh size) sea buckthorn juice from different varieties, which showed INA in the range of -6.1 to -15.1 °C. In this thesis we found for filtered (through 0.45 µm mesh size) sea buckthorn juice the median freezing temperature ($T_{50,het}$) of -26.3 °C, with an onset freezing temperature at -18.5 °C. These differences can be explained by the differences in methodology. The temperature of heterogeneous ice nucleation is in general independent from its volume (Vali, 1971), but since larger sample volumes comprise more INPs, the freezing probability is higher and freezing can occur at higher temperatures (see subchapter 1.4.2). Lundheim and Wahlberg (1998) used sample volumes of 20 µl, which is five orders of magnitude greater than the droplet volumes (4 - 113 pl) we used. Further we cannot rule out that the sample preparation impacts the INA of the plant materials, as the preparation of Lundheim and Wahlberg (1998) differed from ours. They used fresh fruit juice (the upper lipid layer not included) without application of any

[21] INP size comparisons with other publications are often difficult, since they use kDa as unit (Pummer *et al.*, 2012).

heat treatment. Mild pasteurization of the sea buckthorn juice, used in this thesis, was a processing step by which some INPs could be inactivated.

The experiments with different solvents (methanol, methylene chloride, and cyclohexane) revealed that a small amount of the aqueous solvent extracts still shows INA, except for black currant juice. The methylene chloride and cyclohexane extracts of elderberry exhibit the highest INA of the solvent extracts. The low level of INA can have two reasons: either the INPs of the fruit juices cannot be dissolved in the used solvent, or they cannot be recovered with water after the solvent treatment due to structural rearrangements. Since the experiments have worked out only to a low extent, we assume that amphiphilic components seem to play a minor role in the INA of acerola, chokeberry, elderberry and sea buckthorn juice. Conversely, it is thought that polar components play a major role in the INA of all analysed fruit juices. Similar observations were made with birch pollen washing water. Pummer *et al.* (2012) identified that INMs can be washed off from birch pollen grains easily with ultrapure water. However, Seifried (2017) carried out extractions of birch pollen washing water with methanol and n-hexane. After she evaporated the solvent of the collected fractions, the residues were dissolved with ultrapure water again and then assayed for INA. In contrary to our results, she found that the aqueous fractions still show heterogeneous ice nucleation to a large extent and concluded that it is therefore likely that INMs of birch pollen have amphiphilic properties. (Seifried, 2017)

Solely due to the heat treatment (60 °C), aqueous black currant and sea buckthorn samples lose a distinct portion of INA. For both fruit juices the activity loss of the Subtilisin-containing samples is significantly more pronounced. These results could be an indication that proteins or protein complexes play a role in the INA of pure black currant and sea buckthorn juice.
Proteinaceous compounds were also found to be important in the INA of biological material before. Jann *et al.* (1997) suggest that the ice nucleator of sea buckthorn berry juice is likely a high molecular weight complex, which consists of a protein (subunits with 25 to 27 kDa) and a lipid part. In addition, aromatic amino acids seem to play a role in the active sites of INPs (Jann *et al.*, 1997). Our results support this suggestion. Proteins are known to be important in several other cases of biological INA, as e.g. for the bacterium *Pseudomonas*

syringae (Maki *et al.*, 1974; Govindarajan and Lindow, 1988; Lindow *et al.*, 1989) or for the intrinsic INPs in winter rye leaves (Brush *et al.,* 1994)

Nature could have developed the INPs of all five fruit juices in an evolutionary way as a cryopreservation mechanism as all of the used materials stem from plants native to areas, where they are exposed to cold stress. Even in Brazil (cultivation area of acerola berries, our only non-boreal plants), around and south of the Tropic of Capricorn, episodic frost events down to -10 °C can occur. Black currant, chokeberry and sea buckthorn were all grown in winter cold areas (for details see 2.2.2) with average annual minima between -10 and -40 °C. (Kadereit *et al.*, 2014, p. 851)

No information is known about the geographic origin, the varieties and the growth conditions. The influence of these factors on the INA of fruits should be analysed in additional studies in order to make assessments of the INPs of the investigated fruit juices regarding their climatic dependence.

5 Conclusion

The pure fruit juices reveal INA (expressed as $T_{50,het}$ values) in the temperature range between -17.9 and -29,6 °C. The $T_{50,het}$ values of the filtered fruit juices are ranging from -23.7 to -30,5 °C. Hence an INA loss of all the fruit juices took place due to the filtration with a mesh size of 0.45 µm. The loss of INA (expressed as $\Delta T_{50,het}$ values) varies widely, with the maximum decline of 8.5 °C for sea buckthorn and the minimum decline of 0.9 °C for chokeberry. In the filtered juices only the submicron particles smaller than 0.45 µm remained and they still have the ability to serve as INPs. Therefore all analysed samples contain INPs in both fractions: in the coarse (> 0.45 µm) as well as in the submicron size range (< 0.45 µm), whereby the latter INPs can be termed INMs. The main quantity of solid particles that are responsible for the total dry mass, is smaller than 0.45 µm for all examined fruit juices. Overall, no direct correlation between the dry mass and INA of all examined juices was found. Consequently, no conclusions can be drawn from the dry mass of a juice regarding the quantity of INPs. Remarkably, for elderberry juice a massive loss in INA ($\Delta T_{50,het}$ = 6.8 K), but yet no loss in dry mass could be detected. The results of the experiments with different solvents suggest that amphiphilic components play no important role in the INA of acerola, chokeberry, elderberry and sea buckthorn. Due to this fact, it can be argued that polar components play a major role in the INA of all analysed fruit juices.

Aqueous black currant and sea buckthorn samples lose noticeably INA solely due to the heat treatment (60 °C). This fact and the significant INA loss due to treatment with Subtilisin indicate that proteins cause the INA of pure black currant and sea buckthorn juice. For all five juices also broader bands in the different amid regions could be detected via FTIR spectroscopy. Further numerous strong bands were assigned to saccharides, lipids and phenolic compounds.

It can be concluded that while we found some similarities between the different fruit juices (e.g. strong FTIR bands, which are resulting from saccharides), their INPs still differ (e.g. INA loss due to filtration, urea and Subtilisin treatment of black currant and sea buckthorn juice).

6 References

Ahrens, D. C. (2007) *Meteorology Today: An Introduction to Weather, Climate, and the Environment*. 8th edn. Thomson Books/Cole. ISBN: 0495011622.

Asahina É. (1956) 'The Freezing Process of Plant Cell', *Contributions from the Institute of Low Temperature Science*, 10, pp. 83–126.

Bichler, M. (2015) *Investigations on biological ice nucleation concerning plant materials and structural polysaccharides*. Technische Universität Wien.

Bigg, E. K. (1953) 'The Supercooling of Water', *Proceedings of the Physical Society, Section B, IOP Publishing*, 66(8), pp. 688–694. doi: 10.1088/0370-1301/66/8/309.

Brechner, E., Dreesmann, D. and Dinkelaker, B. (2001) *Kompaktlexikon der Biologie. A bis Fotom. (Bd. 1)*. Spektrum. ISBN: 382741041X, http://www.spektrum.de/lexikon/biologie-kompakt/sekundaere-pflanzenstoffe/10686.

Brush, R. A., Griffith, M. and Mlynarz, A. (1994) 'Characterization and Quantification of Intrinsic Ice Nucleators in Winter Rye (Secale-Cereale) Leaves', *Plant Physiology*, 104(2), pp. 725–735. doi: 10.1104/pp.104.2.725.

Burke, M. J., Gusta, L. V., Quamme, H. A., Weiser, C. J., and Li, P. H.(1976) 'Freezing and Injury in Plants', *Annual Review of Plant Physiology*, 27(1), pp. 507–528. doi: 10.1146/annurev.pp.27.060176.002451.

Caballero, R. (2014) *Physics of the atmosphere*. Bristol: IOP Publishing. ISBN: 9780750310529.

Camilloni, C., Guerini Rocco, A., Eberini, I., Gianazza, E., Broglia, R. A., and Tiana, G. (2008) 'Urea and Guanidinium Chloride Denature Protein L in Different Ways in Molecular Dynamics Simulations', *Biophysical Journal*, 94(12), pp. 4654–4661. doi: 10.1529/biophysj.107.125799.

Chen, H., Ferrari, C., Angiuli, M., Yao, J., Raspi, C., Bramanti, E., (2010) 'Qualitative and quantitative analysis of wood samples by Fourier transform infrared spectroscopy and multivariate analysis', *Carbohydrate Polymers*. Elsevier Ltd., 82(3), pp. 772–778. doi: 10.1016/j.carbpol.2010.05.052.

Constantinidou, H. A. and Menkissoglu, O. (1992) 'Characteristics and importance of heterogeneous ice nuclei associated with citrus fruits', *Journal of Experimental Botany*, 43(249), pp. 585–591. doi: 10.1093/jxb/43.4.585.

Cziczo, D. J., Ladino, L., Boose, Y., Kanji, Z. A., Kupiszewski, P., Lance, S., Mertes, S., and Wex, H. (2017) 'Measurements of Ice Nucleating Particles and Ice Residuals', *Meteorological Monographs*, 58(April), p. 8.1-8.13. doi: 10.1175/AMSMONOGRAPHS-D-16-0008.1.

DeMott, P. J. (1990) 'An Exploratory Study of Ice Nucleation by Soot Aerosols', *Journal of Applied Meteorology*, 29, pp. 1072–1079. doi: 10.1175/1520-0450(1990)029<1072:AESOIN>2.0.CO;2.

DeMott, P. J., Prenni, A. J., Liu, X., Kreidenweis, S. M., Petters, M. D., Twohy, C. H., Richardson, M. S., Eidhammer, T., and Rogers, D. C. (2010) 'Predicting global atmospheric ice nuclei distributions and their impacts on climate', *Proceedings of the National Academy of Sciences*, 107(25), pp. 11217–11222. doi: 10.1073/pnas.0910818107.

Diehl, K., Quick, C., Matthias-Maser, S., Mitra, S. K., and Jaenicke, R. (2001) 'The ice nucleation ability of pollen: Part I. Laboratory studies in immersion and contact freezing modes.', *Atmospheric Research*, 58(2), pp. 75–87. doi: 10.1016/S0169-8095(01)00091-6.

Dorsch, R. G. and Hacker, P. T. (1950) 'Technical Note 2142: Photomicrographic Investigation of Spontaneous Freezing Temperatures of Supercooled Water Droplets', *National Advisory Committee for Aeronautics*.

Fabian, P. (1989) *Atmosphäre und Umwelt : chemische Prozesse, menschliche Eingriffe ; Ozon-Schicht, Luftverschmutzung, Smog, saurer Regen*. 3., aktual. Berlin [u.a.]: Springer. ISBN: 0387517383, http://katalog.ub.tuwien.ac.at/AC00056453 %0A.

Friedrich W. Stöcker; Gerhard Dietrich (1986) *Fachlexikon ABC Biologie : ein alphabetisches Nachschlagewerk für Wissenschaftler und Naturfreunde ; etwa 7000 Stichwörter*. 6. edition. Leipzig: Thun [u.a.]. ISBN: 3871448834, http://katalog.ub.tuwien.ac.at/AC00253386.

Govindarajan, A. G. and Lindow, S. E. (1988) 'Size of bacterial ice-nucleation sites measured in situ by radiation inactivation analysis.', *Proceedings of the National Academy of Sciences of the United States of America*, 85(5), pp. 1334–1338. doi: 10.1073/pnas.85.5.1334.

Griffith, M. and Yaish, M. W. F. (2004) 'Antifreeze proteins in overwintering plants: A tale of two activities', *Trends in Plant Science*, 9(8), pp. 399–405. doi: 10.1016/j.tplants.2004.06.007.

Gross, D. C., Proebsting, E. L. and Maccrindle-Zimmerman, H. (1988) 'Development , Distribution , and Characteristics of Intrinsic, Nonbacterial Ice Nuclei in Prunus Wood', *Plant Physiology*, 88, pp. 915–922. doi: 10.1104/pp.88.3.915.

Günzler H.; Gremlich H.-U. (2003) *IR-Spektroskopie : eine Einführung*. 4. edition. Weinheim: Wiley-VCH. ISBN: 3527308016, http://katalog.ub.tuwien.ac.at/AC03756734.

Guo, Y. and Clark, D. S. (2001) 'Activation of enzymes for nonaqueous biocatalysis by denaturing concentrations of urea', *Biochimica et Biophysica Acta - Protein Structure and Molecular Enzymology*, 1546(2), pp. 406–411. doi: 10.1016/S0167-4838(01)00163-7.

Guy, C., Kaplan, F., Kopka, J., Selbig, J., and Hincha, D. K. (2008) 'Metabolomics of temperature stress', *Physiologia Plantarum*, 132(2), pp. 220–235. doi: 10.1111/j.1399-3054.2007.00999.x.

Hartmann, S., Wex, H., Clauss, T., Augustin-Bauditz, S., Niedermeier, D., Rösch, M., and Stratmann, F. (2016) 'Immersion Freezing of Kaolinite: Scaling with Particle Surface Area', *Journal of the Atmospheric Sciences*, 73(1), pp. 263–278. doi: 10.1175/JAS-D-15-0057.1.

Hauptmann, A., Handle, K. F., Baloh, P., Grothe, H., and Loerting, T. (2016) 'Does the emulsification procedure influence freezing and thawing of aqueous droplets?', *Journal of Chemical Physics*, 145(211923). doi: 10.1063/1.4965434.

Huffman, J. A., Prenni, A. J., Demott, P. J., Pöhlker, C., Mason, R. H., Robinson, N. H., Fröhlich-Nowoisky, J., Tobo, Y., Després, V. R., Garcia, E., Gochis, D. J., Harris, E., Müller-Germann, I., … Pöschl, U. (2013) 'High concentrations of biological aerosol particles and ice nuclei during and after rain', *Atmospheric Chemistry and Physics*, 13, pp. 6151–6164. doi: 10.5194/acp-13-6151-2013.

IPCC, 2007: Climate Change 2007: Synthesis Report. Contribution of Working Groups I, II and III to the Fourth Assessment Report of the Intergovernmental Panel on Climate Change [Core Writing Team, Pachauri, R.K and Reisinger, A. (eds.)]. IPCC, Geneva, Switzerland, 104 pp.

IPCC, 2013: Summary for Policymakers. In: Climate Change 2013: The Physical Science Basis. Contribution of Working Group I to the Fifth Assessment Report of the Intergovernmental Panel on Climate Change [Stocker, T.F., D. Qin, G.-K. Plattner, M. Tignor, S.K. Allen, J. Boschung, A. Nauels, Y. Xia, V. Bex and P.M. Midgley (eds.)]. Cambridge University Press, Cambridge, United Kingdom and New York, NY, USA.

IPCC, 2014: Climate Change 2014: Synthesis Report. Contribution of Working Groups I, II and III to the Fifth Assessment Report of the Intergovernmental Panel on Climate Change [Core Writing Team, R.K. Pachauri and L.A. Meyer (eds.)]. IPCC, Geneva, Switzerland, 151 pp.

Jann, A., Lundheim, R., Niederberger, P., and Richard, M. (1997) 'Increasing freezing point of food with sea buckthorn ice nucleating agent'. United States Patent.

Kačuráková, M., Capek, P., Sasinkova, V., Wellner, N., Ebringerova, A., and Kac, M. (2000) 'FT-IR study of plant cell wall model compounds : pectic polysaccharides and hemicelluloses', 43(2), pp. 195–203. doi: 10.1016/S0144-8617(00)00151-X.

Kadereit, J. W., Körner, C., Kost, B., Sonnewald, U. (2014) *Strasburger - Lehrbuch der Pflanzenwissenschaften*. 37. edition. Berlin [u.a.] : Springer. ISBN: 9783642544347, http://katalog.ub.tuwien.ac.at/AC11685588 %0A.

Kajava, A. V. and Lindow, S. E. (1993) 'A Model of the Three-dimensional Structure of Ice Nucleation Proteins', *Journal of Molecular Biology*, pp. 709–717. doi: 10.1006/jmbi.1993.1424.

Kieft, T. L. (1988) 'Ice nucleation activity in lichens.', *Applied and environmental microbiology*, 54(7), pp. 1678–1681.

Kiehl, J. T. and Trenberth, K. E. (1997) 'Earth's Annual Global Mean Energy Budget', *Bulletin of the American Meteorological Society*, 78(2), pp. 197–208. doi: 10.1175/1520-0477(1997)078<0197:EAGMEB>2.0.CO;2.

Kishimoto, T., Yamazaki, H., Saruwatari, A., Murakawa, H., Sekozawa, Y., Kuchitsu, K., Price, W. S., and Ishikawa, M. (2014) 'High ice nucleation activity located in blueberry stem bark is linked to primary freeze initiation and adaptive freezing behaviour of the bark', *AoB PLANTS*, 6(plu044), pp. 1–17. doi: 10.1093/aobpla/plu044.

Knopf, D. A., Wang, B., Laskin, A., Moffet, R. C., and Gilles M. K. (2010) 'Heterogeneous nucleation of ice on anthropogenic organic particles collected in Mexico City', *Geophysical Research Letters*, 37(11), pp. 1–5. doi: 10.1029/2010GL043362.

Kremer, B. P. (2010) *Essbare & giftige Wildpflanzen : über 200 Kräuter, Beeren und Nüsse ; [Gaumenfreude oder Giftbeere]*. Stuttgart : Ulmer. ISBN: 9783800153442, http://katalog.ub.tuwien.ac.at/AC08168432 %0A.

Kulikov, M. Y., Feigin, A. M. and Sonnemann, G. R. (2009) 'Retrieval of water vapor profile in the mesosphere from satellite ozone and hydroxyl measurements by the basic dynamic model of mesospheric photochemical system', *Atmospheric Chemistry and Physics*, 9(21), pp. 8199–8210. doi: 10.5194/acp-9-8199-2009.

Langham, E. J. and Mason, B. J. (1958) 'The heterogeneous and homogeneous nucleation of supercooled water', *Proceedings of the Royal Society of London. Series A, Mathematical and Physical Sciences*, 247(1251). doi: 10.1098/rspa.1958.0207.

Lehmann, T. (2009) 'UV/VIS Spektroskopie', *Freie Universität Berlin*, pp. 1–15.

Levine, J. (1950) 'Technical Note 2234: Statistical Explanation of Spontaneous Freezing of Water Droplets', *National Advisory Committee for Aeronautics*.

Lindow, S. E., Arny, D. C. and Upper, C. D. (1978) 'Distribution of ice-nucleation active bacteria on plants in nature', *Applied and Environmental Microbiology*, 36(6), pp. 831–838.

Lindow, S. E., Lahue, E., Govindarajan, A. G., Panopoulos, N. J., and Gies, D. (1989) 'Localization of Ice Nucleation Activity and the iceC Gene Product in Pseudomonas syringae and Escherichia coli', *Molecular Plant-Microbe Interactions*, pp. 262–272. doi: 10.1094/MPMI-2-262.

Lohmann, U., Lüönd, F. and Mahrt, F. (2016) *An introduction to clouds: from the microscale to climate*. Cambridge : Cambridge University Press. ISBN: 1139087517.

Lu, R. (1992) *Seabuckthorn: A Multipurpose Plant Species for Fragile Mountains*, *ICIMOD Occasional Paper No. 20*. Kathmandu, Nepal. ISBN: 9291150300.

Lundheim, R. and Wahlberg, K. (1998) 'Ice nucleation in fruit juice from different varieties of sea buckthorn Hippophaë rhamnoides L.', *Euphytica*, 102(1), pp. 117–124. doi: 10.1023/A:1018336413479.

Maki, L. R., Galyan, E. L., Chang-Chien, M. M., and Caldwell, D. R. (1974) 'Ice nucleation induced by pseudomonas syringae', *Applied microbiology*, 28(3), pp. 456–459. doi: 10.1111/1462-2920.12668.

Miyazawa, T., Shimanouchi, T. and Mizushima, S. (1956) 'Characteristic Infrared Bands of Monosubstituted Amides', *The Journal of Chemical Physics*, 24, pp. 408–418. doi: 10.1063/1.1742489.

Murray, B. J., Wilson, T. W., Dobbie, S., Cui, Z., Al-Jumur, S. M. R. K., Möhler, Ö., Schnaiter, M., Wagner, R., Benz, S., Niemand, M., Saathoff, H., Ebert, V., … Kärcher, B. (2010a) 'Heterogeneous nucleation of ice particles on glassy aerosols under cirrus conditions', *Nature Geoscience*. Nature Publishing Group, 3(4), pp. 233–237. doi: 10.1038/ngeo817.

Murray, B. J., Broadley, S. L., Wilson, T. W., Bull, S. J., Wills, R. H., Christenson, H. K., and Murray, E. J. (2010b) 'Kinetics of the homogeneous freezing of water', *Physical Chemistry Chemical Physics*, 12(35), pp. 10380–10387. doi: 10.1039/c003297b.

Murray, B. J., Broadley, S. L., Wilson, T. W., Atkinson, J. D., and Wills, R. H. (2011) 'Heterogeneous freezing of water droplets containing kaolinite particles', *Atmospheric Chemistry and Physics*, 11(9), pp. 4191–4207. doi: 10.5194/acp-11-4191-2011.

Murray, B. J., O'Sullivan, D., Atkinson, J. D., and Webb, M. E. (2012) 'Ice nucleation by particles immersed in supercooled cloud droplets', *Chemical Society Reviews*, 41(19), pp. 6519–6554. doi: 10.1039/c2cs35200a.

Niedermeier, D., Shaw, R. A., Hartmann, S., Wex, H., Clauss, T., Voigtländer, J., and Stratmann, F. (2011) 'Heterogeneous ice nucleation: Exploring the transition from stochastic to singular freezing behavior', *Atmospheric Chemistry and Physics*, 11(16), pp. 8767–8775. doi: 10.5194/acp-11-8767-2011.

O'Sullivan, D., Murray, B. J., Ross, J. F., and Webb, M. E. (2016) 'The adsorption of fungal ice-nucleating proteins on mineral dusts: A terrestrial reservoir of atmospheric ice-nucleating particles', *Atmospheric Chemistry and Physics*, 16, pp. 7879–7887. doi: 10.5194/acp-16-7879-2016.

Pearce, R. S. (2001) 'Plant freezing and damage', *Annals of Botany*, 87(4), pp. 417–424. doi: 10.1006/anbo.2000.1352.

Perkampus, H.-H. (1992) *UV-VIS spectroscopy and its applications: with 21 tables*. Berlin [u.a.] : Springer. ISBN: 0387554211, http://katalog.ub.tuwien.ac.at/AC00545910.

Perlmann, G. E. (1956) 'Observations on the Effect of Urea on Crystalline Pepsin', *Archives of Biochemistry and Biophysics*, 65, pp. 210–217.

Petty, G. W. (2008) *A First Course in Atmospheric Thermodynamics*. Madison, Wisconsin: Sundog Publishing. ISBN: 9780972903325.

Phillips, R. L. (2005) 'Barbados Cherry', *UF University of Florida IFAS Extension*, p. FC28_1-3.

Phillips, V. T. J., Donner, L. J. and Garner, S. T. (2007) 'Nucleation Processes in Deep Convection Simulated by a Cloud-System-Resolving Model with Double-Moment Bulk Microphysics', *Journal of the Atmospheric Sciences*, 64(3), pp. 738–761. doi: 10.1175/JAS3869.1.

Pouleur, S., Richard, C., Martin, J., and Antoun, H. (1992) 'Ice Nucleation Activity in Fusarium-Acuminatum and Fusarium-Avenaceum', *Applied and Environmental Microbiology*, 58(9), pp. 2960–2964.

Pratt, K. A., DeMott, P. J., French, J. R., Wang, Z., Westphal, D. L., Heymsfield, A. J., Twohy, C. H., Prenni, A. J., and Prather, K. A. (2009) 'In situ detection of biological particles in cloud ice-crystals', *Nature Geoscience*. Nature Publishing Group, 2(6), pp. 398–401. doi: 10.1038/ngeo521.

Pretsch, E.; Bühlmann, P.; Affolter, C.; Badertscher, M. (2001) *Spektroskopische Daten zur Strukturaufklärung organischer Verbindungen*. 4. edition. Berlin [u.a.]: Springer. ISBN: 3540418776, http://katalog.ub.tuwien.ac.at/AC03281405 %0A.

Pruppacher, H. R. and Klett, J. D. (2010) *Microphysics of Clouds and Precipitation*. 2. edition. Springer. ISBN: 9780306481000.

Pummer, B. (2013) *Ice nucleation activity of pollen and fungal spores*. Technische Universität Wien.

Pummer, B. G., Bauer, H., Bernardi, J., Bleicher, S., and Grothe, H. (2012) 'Suspendable macromolecules are responsible for ice nucleation activity of birch and conifer pollen', *Atmospheric Chemistry and Physics*, 12, pp. 2541–2550. doi: 10.5194/acp-12-2541-2012.

Pummer, B. G., Bauer, H., Bernardi, J., Chazallon, B., Facq, S., Lendl, B., Whitmore, K., and Grothe, H. (2013) 'Chemistry and morphology of dried-up pollen suspension residues', *Journal of Raman Spectroscopy*, 44(12), pp. 1654–1658. doi: 10.1002/jrs.4395.

Pummer, B. G., Budke, C., Augustin-Bauditz, S., Niedermeier, D., Felgitsch, L., Kampf, C. J., Huber, R. G., Liedl, K. R., Loerting, T., Moschen, T., Schauperl, M., Tollinger, M., Morris, C. E., … Fröhlich-Nowoisky, J. (2015) 'Ice nucleation by water-soluble macromolecules', *Atmospheric Chemistry and Physics*, 15(8), pp. 4077–4091. doi: 10.5194/acp-15-4077-2015.

Schnell, R. C. and Vali, G. (1973) 'World-wide Source of Leaf-derived Freezing Nuclei', *Nature*, 246, pp. 212–213. doi: 10.1038/246212a0.

Schulz, H. and Baranska, M. (2007) 'Identification and quantification of valuable plant substances by IR and Raman spectroscopy', *Vibrational Spectroscopy*, 43(1), pp. 13–25. doi: 10.1016/j.vibspec.2006.06.001.

Seifried, T. M. (2017) *Analytical Characterization of Macromolecular Ice Nuclei from Birch Pollen Grains*. Technische Universität Wien.

Seinfeld, J. H. and Pandis, S. N. (1998) *Atmospheric chemistry and physics of air pollution*. New York, NY [u.a.]: John Wiley & Sons, Inc. ISBN: 0471178160.

Seinfeld, J. H. and Pandis, S. N. (2016) *Atmospheric Chemistry and Physics: From Air Pollution to Climate Change*. 3 edition. John Wiley & Sons, Inc. ISBN: 9781119221173.

Smith, B. C. (2011) *Fundamentals of fourier transform infrared spectroscopy*. 2 edition. Boca Raton, Fla. [u.a.]: CRC Press. ISBN: 9781420069297, http://katalog.ub.tuwien.ac.at/AC08784157 %0A.

Storey, J. M. and Storey, K. B. (2004) 'Cold Hardiness and Freeze Tolerance', in *Functional Metabolism: Regulation and Adaptation*. Hoboken: John Wiley & Sons, Inc, pp. 470–503. doi: 10.1002/047167558X.ch17.

Stuart, B. H. (2004) *Infrared Spectroscopy: Fundamentals and Applications*, *Methods*. John Wiley & Sons, Inc. ISBN: 0470854278, http://doi.wiley.com/10.1002/0470011149.

Le Treut, H., R. Somerville, U. Cubasch, Y. Ding, C. Mauritzen, A. Mokssit, T. Peterson and M. Prather, 2007: Historical Overview of Climate Change. In: Climate Change 2007: The Physical Science Basis. Contribution of Working Group I to the Fourth Assessment Report of the Intergovernmental Panel on Climate Change [Solomon, S., D. Qin, M. Manning, Z. Chen, M. Marquis, K.B. Averyt, M. Tignor and H.L. Miller (eds.)]. Cambridge University Press, Cambridge, United Kingdom and New York, NY, USA. pp. 93–127. doi: 10.1016/j.soilbio.2010.04.001.

Urrutia, M. E., Duman, J. G. and Knight, C. A. (1992) 'Plant thermal hysteresis proteins', *Biochimica et Biophysica Acta (BBA)/Protein Structure and Molecular*, 1121(1–2), pp. 199–206. doi: 10.1016/0167-4838(92)90355-H.

Vali, G. (1971) 'Quantitative Evaluation of Experimental Results an the Heterogeneous Freezing Nucleation of Supercooled Liquids', *Journal of the Atmospheric Sciences*, 28(3), pp. 402–409. doi: 10.1175/1520-0469(1971)028<0402:QEOERA>2.0.CO;2.

Vali, G. (1994) 'Freezing Rate Due to Heterogeneous Nucleation', *Journal of the Atmospheric Sciences*, 51(13), pp. 1843–1856. doi: 10.1175/1520-0469(1994)051<1843:FRDTHN>2.0.CO;2.

Vali, G., DeMott, P. J., Möhler, Ö., and Whale, T. F. (2015) 'Technical Note: A proposal for ice nucleation terminology', *Atmospheric Chemistry and Physics*, 15(18), pp. 10263–10270. doi: 10.5194/acp-15-10263-2015.

Vali, G. and Stansbury, E. J. (1966) 'Time-Dependent Characteristics of the Heterogeneous Nucleation of Ice', *Canadian Journal of Physics*, 44(3), pp. 477–502. doi: 10.1139/p66-044.

Wang, P. K. (2013) *Physics and dynamics of clouds and precipitation*. Cambridge : Cambridge University Press. ISBN: 9781107005563.

WMO (1975) *International Cloud Atlas. Volume I: Manual on the observation of clouds and other meteors*, *WMO Publication*. Geneva, Switzerland. ISBN: 9263104077.

Zachariassen, K. E. and Kristiansen, E. (2000) 'Ice Nucleation and Antinucleation in Nature', *Cryobiology*, 41(4), pp. 257–279. doi: 10.1006/cryo.2000.2289.

Zaragotas, D., Liolios, N. T. and Anastassopoulos, E. (2016) 'Supercooling, ice nucleation and crystal growth: A systematic study in plant samples', *Cryobiology*. Elsevier Ltd, 72(3), pp. 239–243. doi: 10.1016/j.cryobiol.2016.03.012.

Zimmermann, R. (2015) 'Aerosols and health: A challenge for chemical and biological analysis', *Analytical and Bioanalytical Chemistry*, 407(20), pp. 5863–5867. doi: 10.1007/s00216-015-8832-x.

Zolles, T., Burkart, J., Häusler, T., Pummer, B., Hitzenberger, R., and Grothe, H. (2015) 'Identification of ice nucleation active sites on feldspar dust particles', *Journal of Physical Chemistry A*, 119(11), pp. 2692–2700. doi: 10.1021/jp509839x.

Zuberi, B., Bertram, A. K., Koop, T., Molina L. T., and Molina M. J. (2001) 'Heterogeneous freezing of aqueous particles induced by crystallized (NH4)2SO4, ice, and letovicite', *Journal of Physical Chemistry A*, 105(26), pp. 6458–6464. doi: 10.1021/jp010094e.

7 Appendix

7.1. UV-VIS Measurements

The used solid reference substances and their used mass concentrations are presented in Table 13. These substances were dissolved in ultrapure water corresponding to their solubility product. We performed the dissolution process in water in an ultrasonic bath (EMAG Emmi-40HC) for 20 minutes at room temperature. The various solutions were stored over night at a temperature of 8 °C. Before we started the measurements with the UV-VIS spectrometer the next day, the reference solutions were placed in the ultrasonic bath again under exactly the same conditions described previously. The ultrapure water blank was treated the same way as the other aqueous solutions. The absorption spectra of the reference substances are illustrated in Figure 51 and Figure 52.

Table 13: Reference substances for the qualitative UV-VIS measurements.

Chemical	Weight [mg] in 5 ml	Annotation
(+)Arabinogalactan	15.0	
Cinnamic acid ($C_9H_8O_2$)	22.2	*
Citric acid-1-hydrate ($C_6H_8O_7{*}H_2O$)	21.7	
Dextrin $(C_6H_{10}O_5)_n$ {yellow}	112.4	
L(+)Tartaric acid ($C_4H_6O_6$)	53.9	
Malt extract	54.4	*
Oxalic acid anhydrous ($C_2H_2O_4$)	22.1	*
Pectin esterified (lemon)	17.3	
Sucrose ($C_{12}H_{22}O_{11}$)	105.3	
Salicylic acid ($C_7H_6O_3$)	1.5	
Starch soluble $(C_6H_{10}O_5)_n$	12.5	*
Syringic acid ($C_9H_{10}O_5$)	2.4	
Vanillic acid ($C_8H_8O_4$)	2.0	
Vanillin ($C_8H_8O_3$)	17.6	
Xanthone ($C_{13}H_8O_2$)	2.8	*
α -Tyrosine ($C_9H_{11}NO_3$)	1.4	

* These compounds were not fully dissolved after the ultrasonic treatment. Attention was paid for the UV-VIS measurements to determine just the supernatant and not the deposited solids.

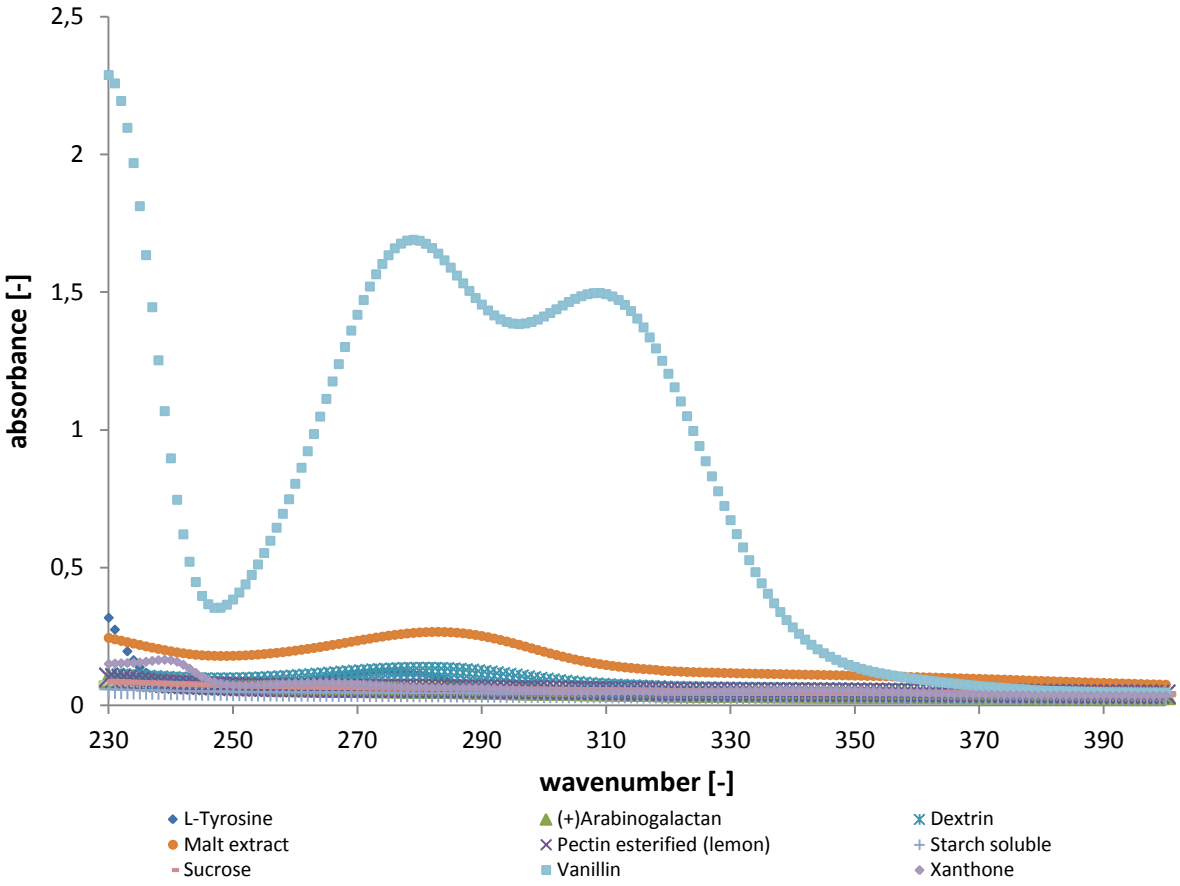

Figure 51: Absorption spectra of chemical compounds (reference substances), which can occur naturally in fruits and/or plants - diluted in ultrapure water, the concentration is given in Table 13.

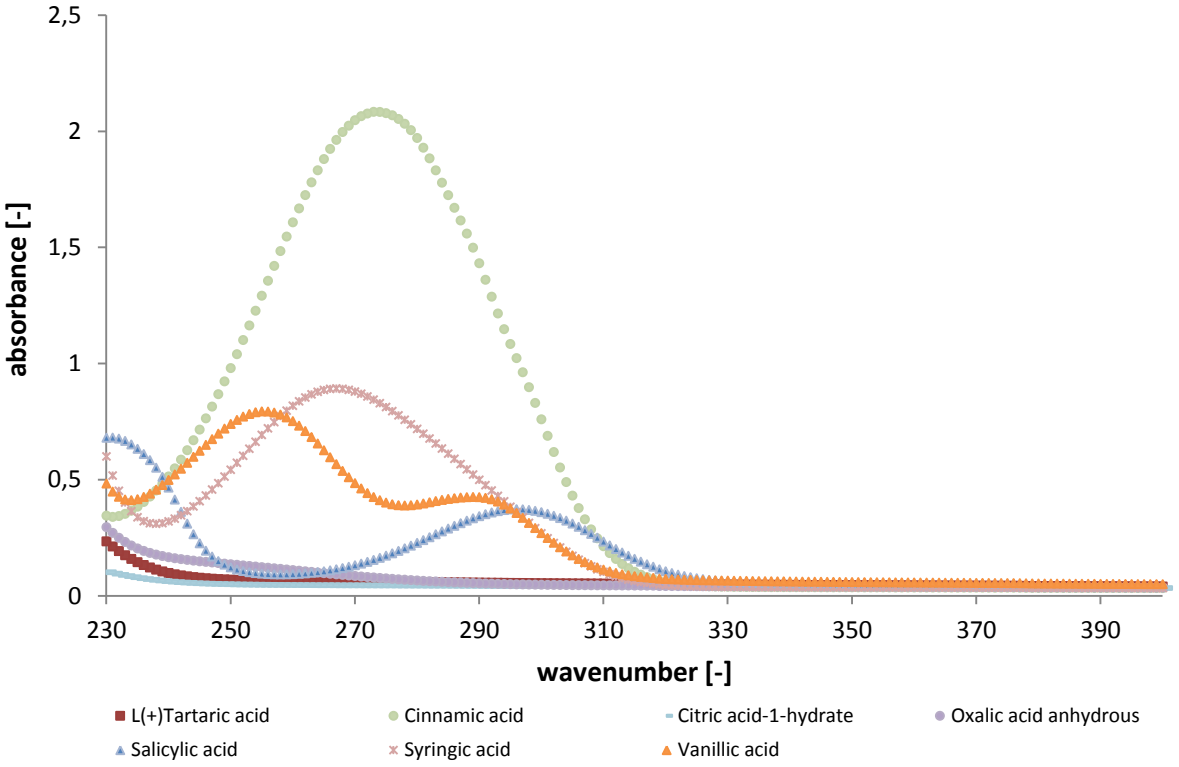

Figure 52: Absorption spectra of chemical acids or acid derivatives (reference substances), which can occur naturally in fruits and/or plants - diluted in ultrapure water, the concentration is given in Table 13.

7.2. Chemicals

All of the chemicals that were used for the measurements in this thesis are listed in Table 14.

Table 14: A list of all used chemicals in this thesis. Given is the company name, level of purity, package size and reference number.

Chemical	Company name	Level of purity	Package size	Reference number
(+)Arabinogalactan (larch)	Sigma	n. a.	25 g	10830-25G
Cinnamic acid ($C_9H_8O_2$)	Merck	> 99 %	250 g	9267417
Citric acid-1-hydrate ($C_6H_8O_{7*}H_2O$)	Riedel-de Haën	≥ 99.8 %	1 kg	03400
Cyclohexane (C_6H_{12})	Sigma-Aldrich	≥ 99.9 %	1 l	650455-1L
Dextrin $(C_6H_{10}O_5)_n$	Roth	n. a.	1 kg	333202908
Guanidinium chloride (CH_6ClN_3)	Merck	≥ 99.0 %	100 g	TD962220 101
L(+)Tartaric acid ($C_4H_6O_6$)	Merck	≥ 99.5 % p. a.	250 g	8543453
Lanolin anhydrous	Bio-Shop 6850 Dornbirn	anhydrous, pesticide-free	1 kg	n. a.
L-Tyrosine ($C_9H_{11}NO_3$)	Fluka	≥ 99%	100 g	360476/1
Malt extract	Roth	n. a.	500 g	243201080
Methanol (CH_3OH)	Sigma-Aldrich	≥ 99.9 %	1 l	34860-1L-R
Methylene chloride (CH_2Cl_2)	Roth	≥ 99.5 %	2.5 l	n. a.
	Riedel-de Haën	≥ 99.8 %	1 l	53120-1L
Oxalic acid anhydrous ($C_2H_2O_4$)	Fluka	≥ 99 %	50 g	408986/1
Paraffin oil light	AppliChem	pure	2.5 l	A4692.2500
Pectin esterified (lemon)	Sigma	n. a.	5 g	P9561-5G
Salicylic acid ($C_7H_6O_3$)	n. a.	n. a.	n. a.	n. a.
Snomax®	SMI Snow Makers AG	n. a.	n. a.	n. a.
Starch soluble $(C_6H_{10}O_5)_n$	Merck	p. a.	250 g	E577552
Subtilisin (Protease from Bacillus licheniformis)	Sigma	Type VIII, lyophilized powder; 11 units/mg solid	25 mg	P5380-25mg
Sucrose ($C_{12}H_{22}O_{11}$)	Wiener Zucker	n. a.	1 kg	L12161104 1
Syringic acid ($C_9H_{10}O_5$)	Fluka	≥ 97%	50 g	358321/1
Tris(hydroxymethyl)amino-methane ($C_4H_{11}NO_3$)	Sigma-Aldrich	≥ 99.8%	100 g	252859-100g
Vanillic acid ($C_8H_8O_4$)	Aldrich	97 %	25 g	26222-129
Vanillin ($C_8H_8O_3$)	Fluka	≥ 98%	500 g	405529/1
Xanthone ($C_{13}H_8O_2$)	Merck	98 %	n. a.	4203815